Spring 1996

Rocket observations of the HF heated ionosphere

William James Peria
University of New Hampshire, Durham

INFORMATION TO USERS

This manuscript has been reproduced from the microfilm master. UMI films the text directly from the original or copy submitted. Thus, some thesis and dissertation copies are in typewriter face, while others may be from any type of computer printer.

The quality of this reproduction is dependent upon the quality of the copy submitted. Broken or indistinct print, colored or poor quality illustrations and photographs, print bleedthrough, substandard margins, and improper alignment can adversely affect reproduction.

In the unlikely event that the author did not send UMI a complete manuscript and there are missing pages, these will be noted. Also, if unauthorized copyright material had to be removed, a note will indicate the deletion.

Oversize materials (e.g., maps, drawings, charts) are reproduced by sectioning the original, beginning at the upper left-hand corner and continuing from left to right in equal sections with small overlaps. Each original is also photographed in one exposure and is included in reduced form at the back of the book.

Photographs included in the original manuscript have been reproduced xerographically in this copy. Higher quality 6" x 9" black and white photographic prints are available for any photographs or illustrations appearing in this copy for an additional charge. Contact UMI directly to order.

UMI

A Bell & Howell Information Company
300 North Zeeb Road, Ann Arbor MI 48106-1346 USA
313/761-4700 800/521-0600

Rocket Observations of the HF Heated Ionosphere

BY

William J. Peria

B.S., University of Minnesota (1988)

DISSERTATION

Submitted to the University of New Hampshire
in partial fulfillment of
the requirements for the degree of

Doctor of Philosophy

in

Physics

May 1996

This dissertation has been examined and approved.

Dissertation director, R. B. Torbert
Professor of Physics

R. L. Arnoldy
Professor of Physics

R. L. Kaufmann
Professor of Physics

T. G. Onsager
Research Assistant Professor of Physics

H. K. Shepard
Professor of Physics

May 3, 1996
Date

Acknowledgments

A large number of exceptional people contributed to this thesis. My advisor, Professor Roy Torbert, gave me with the opportunity, support, independence and guidance necessary to pursue this unique project. Professor Roger Arnoldy enabled me to come to the physics department at UNH, and was an excellent role model and a pleasure to work with. I am very grateful to Professor Harvey Shepard for his no-nonsense manner at a time when I was struggling to pass classes: at his insistence I examined my priorities, and then made the decision to stay in graduate school. Professor Dick Kaufmann gave me, in his course and in discussions, a sensible and solid way of approaching problems in plasma physics. Professor Terry Onsager was tireless in our daily discussions of my work; many of the ideas and methods of this thesis took shape in his office. Professor Mike Kelley deserves many thanks both for writing his excellent book and for repeatedly reading my thesis and providing many valuable suggestions each time. Professor Laurence Cahill gave me my introduction to space physics by hiring me as a relatively useless and arrogant undergraduate, I owe him a great debt. I would like to specially acknowledge Professor Phyllis Freier, and the love of physics she so relentlessly shared with all her students; may these pages be worthy of her memory.

I would like to thank Dave Rau for his time, energy, and good humor throughout this project: at UNH, at Wallops, and in Puerto Rico. Craig Kletzing took a keen interest in this project and helped me through the initial science meetings and some of the actual physics. Eric Dors, as my office mate of over five years, shared with me all the highs and lows of this project, as well as his indispensable computer expertise. Dr. Kristina Lynch

gave scientific and moral support to every phase of this project; she deserves many thanks.

This project was greatly aided by countless educational and enjoyable discussions (and vacuum chamber time!) with the staff of the Arnoldy lab: Hank Dolben, Marc Lessard, Mark Widholm, and David Young deserve special thanks. As a student in the Arnoldy group, Brett Austin worked with me extensively on technical problems related to electric field data analysis, for which I am very grateful.

This thesis relies heavily on the technical skills and expertise of many excellent people, including the precision machining of Arthur Anderson and John Levasseur, the NASA-certified electronics construction of Jon Googins and Paul Vachon, the microprocessor wizardry of Vincent Ye, and finally the integration and launch support of personnel at the NASA Wallops Flight Facility. Thanks are due to Chris de Heer for his assistance on several figures. This work was supported by a fellowship from NASA's Graduate Student Research Program.

Colleen E. McVeigh patiently climbed the walls during my final phase of thesis writing. She absorbed all my nervousness and kept things moving along; one wonders if this project could ever have reached completion without her! Certainly not as soon, nor so happily!

Finally I acknowledge the love and dedication of my parents, Joan and Bill Peria. There is no way to fully acknowledge their contribution to this project!

Table of Contents

List of Figures

ABSTRACT

Rocket Observations of the HF Heated Ionosphere

by

William J. Peria
University of New Hampshire, February, 1996

Measurements of the ion distribution function, electron density, wave activity, and convection electric field have been made *in situ* by a sounding rocket flown through the artificially heated F layer ionosphere over Arecibo, Puerto Rico. The ion distributions show the effect of the HF heater through elevated effective temperatures, superthermal fluctuation levels, and a plume-like population of energetic ions drifting out of the HF reflection region. The electron density, from a Langmuir probe, shows meter-scale depletions of $\sim$ 10 % in the immediate vicinity of the reflection height, both above and below [Kelley et al., 1995]. A shear in the convection electric field observed at the reflection layer can be interpreted as the return current at the westward edge of a heater driven current system.

The payload also passed within 2.2 km of the Arecibo 430 MHz incoherent scatter radar (ISR) beam, where a burst of energetic ions was observed, preceded by coherent wave activity in both the Langmuir and electric field double-probe. A cross spectral analysis indicates that the waves originate from the ISR beam.

Chapter 1

Ionospheric Heating

Powerful electromagnetic waves can heat the ionosphere. At frequencies of a few MHz, radio waves become resonant with the ionospheric plasma, and at sufficiently high powers, such resonant waves will dissipate substantial amounts of energy into the plasma. It is not easy to understand such dissipation in a collisionless plasma, and the study of ionospheric heating draws on several active areas of plasma physics research. One of the first successful heating experiments was performed in the spring of 1970 in Platteville, Colorado[Utlaut, 1970], and many basic questions remain unanswered.

Ionospheric heating occurs when a powerful electromagnetic wave is reflected off the conductivity gradient in the ionosphere. As a wave propagates upward into the ionosphere, it encounters plasma of steadily increasing density. The plasma frequency, being proportional to the square root of the plasma density, is increasing as well. When the plasma frequency ω_{pe} becomes equal to the wave frequency ω , the wave is said to have a "cutoff", and it can propagate no further [Jackson, 1975]. Cutoffs correspond to zeroes in the refractive index, in this case given by $1 - (\frac{\omega_p}{\omega})^2$. Physically, the cutoff can be pictured by imagining the wave finally encountering a layer where the electrons become fully able to screen out the wave electric field, preventing its further communication. The impulse delivered to (and therefore the deflection of) each and every electron during a half-cycle of the heater wave

field is fixed, and therefore the degree to which the plasma can be polarized by an incident wave is measured by the *number* of deflected electrons, in other words, the density. This is the reason for the relation between plasma frequency and density, and in this way we can understand that, for a wave of a given frequency, a *critical* density might exist, above which no propagation is possible.

Strictly speaking, such a cutoff does not include any dissipative effects. And yet dissipation does occur in ionospheric heating experiments. The electron temperature has been observed to increase by factors of 2 or 3[Showen and Behnke, 1978], while the ion temperature has been observed to increase by 30% or more [Djuth et al., 1987b]. Artificial spread F is created in this type of experiment[Utlaut et al., 1970], and strongly enhanced Langmuir fluctuations are indicated by both incoherent scatter radar [Carlson et al., 1972] and stimulated electromagnetic emission (SEE) measurements[Leyser and B. Thidé, 1988]. These phenomena cover spatial scales from kilometers (spread F and thermal "patches") to centimeters (Langmuir waves and cavitons), corresponding to time scales of minutes to microseconds.

Heating the F layer ionosphere near the plasma frequency produces a rich variety of plasma phenomena, including the Rayleigh-Taylor instability (spread F), the parametric decay instability (Langmuir waves and ion acoustic waves), strong Langmuir turbulence and cavitons, kilometer-scale density depletions and 10-m scale filamentary field-aligned vortices, seeded by the nonlinear ponderomotive force.

An interesting feature of heating is that it appears to occur only, or at least much more strongly, when the heater wave has O-mode polarization, with the wave electric field parallel to the geomagnetic field $\vec{\mathbf{B}}_0$, as opposed to X-mode, with the wave electric field perpendicular to $\vec{\mathbf{B}}$. This is believed to be related to the fact that the X-mode is cutoff

at ω_R, the right-hand cutoff frequency. Since $\omega_R > \omega_p$, the X-mode encounters this cutoff *before* it reaches an altitude where it is resonant with the local plasma frequency.

Most measurements of the artificially-heated ionosphere are made, not surprisingly, from the ground. The heated region can be probed with incoherent scatter radar (ISR), observed passively using stimulated electromagnetic emissions (SEE) near the heater, or pump, frequency, or even diagnosed through optical observations of enhanced airglow emissions. In this thesis, we will describe *in situ* measurements, made near the heated region from a rocket.

1.1 Ionospheric Heating Experiments

1.1.1 Incoherent Scatter Radar

Incoherent scatter radar (ISR) is the diagnostic most often employed in the study of the heated ionosphere. Note that the words "incoherent scatter" are intended to imply that the power returned to the radar consists of radiation from the acceleration of individual ionospheric electrons by the radar beam. This was the original idea, but the first measurements made with an ISR [Bowles, 1958] showed that in fact most of the scattering occurs off the Debye clouds of individual *ions*. Thus, the main feature of an ISR spectrum is the central peak, broadened by the thermal *ion* velocity. This feature is called the ion line. In the ambient ionosphere, true incoherent scatter, manifested by a small spectral peak shifted from the ISR frequency by the electron plasma frequency, is quite difficult to observe [Isham, 1991]. During HF modification, however, the plasma line is greatly enhanced and observable, and is referred to as the HFPL, meaning HF-enhanced plasma line.

For the non-specialist, it is sufficient to remember that

- *The ISR technique deals in extremely weak signals.* The standard analogy is that the effective cross section of the F region is the same as that of a *small ball bearing* at the same range. Many clever schemes are used to increase the signal-noise ratio. The simplest of these is the use of fairly long pulse lengths, at the expense of altitude resolution.

- *An ISR probes the fluctuation power at only its own half-wavelength* A 430 MHz radar, for example, detects fluctuation power at $\frac{1}{2}\frac{c}{430}$ MHz $= 0.35$ meters, where c is the speed of light. Imagine that the backscattered spectrum has a peak at 430.001 MHz. This peak corresponds to a peak in the thermal fluctuation spectrum of the plasma at a frequency of 1.0 kHz, a wavelength of .35 meters, and a phase velocity of 350 m/s.

1.1.2 Stimulated Electromagnetic Emission

"Stimulated electromagnetic emission", in the context of ionospheric heating, refers to a class of passive experiments, where radio receivers tuned near the HF-heater frequency are used to detect the spectrum of HF radiation scattered from the ionosphere. The SEE spectrum is quite complex [Leyser and B. Thidé, 1988], but one clear and robust result is a peak down-shifted from the heater frequency by a few khZ. This peak supports the idea of a horizontally stratified density structure (several %, 100 meter altitude scale) corresponding to the standing wave pattern of the reflecting heater wave. The evidence for this is a spectral peak down-shifted from the heater frequency by a few kHz, corresponding to trapped Langmuir waves which have undergone linear mode conversion to EM waves. Langmuir waves, formed by the parametric decay instability (PDI), are trapped in the minima of the horizontally stratified standing wave or "Airy" pattern which occurs at the reflection height. They undergo linear mode conversion [Stix, 1992] on the density gradients as they

propagate out of the density wells, becoming electromagnetic and radiating out of the system. Since these waves are produced (by PDI) at the local Langmuir frequency, they are a diagnostic for the density in the wells. The observed downward frequency shift of a few kHz corresponds well with the expected Airy pattern density depletions of ~ 1 %.

The interpretation of an observed SEE spectrum requires a model for the zeroth-order T_e/T_i and density profiles, as well as for the standing wave pattern of the reflected wave. The dependence on T_e/T_i is weak, however, meaning that the SEE is not a good diagnostic of the ion temperature.

1.1.3 Airglow

Natural airglow occurs when ionospheric electrons with energies of a few eV excite neutral atoms. This is similar to the visible light generation of diffuse aurora, but at a much lower intensity, measured in Rayleighs, not the kiloRayleighs of the visible aurora. Enhancement of the natural airglow is often observed during ionospheric heating.

Biondi et. al. [Biondi et al., 1970] were the first to observe airglow during heating. Airglow consists of several optical emission lines of O_2^+, NO^+, N_2^+, and may be an indicator of a superthermal (a few to several eV) e^- from the heater. For typical levels of airglow enhancement from 20-250 Rayleighs [Haslett and Megill, 1974], Nicholson estimated the superthermal electron flux from the heater to be between 2×10^8 and 2×10^9 electrons/cm^2-s[Nicholson, 1977]. Others argue that the airglow is a heat conduction effect, requiring no superthermal electrons [Mantas and Carlson, 1996]. Bernhardt observes a drift of the airglow pattern, followed by a snapback to its original spot, at SURA[Bernhardt et al., 1988] and at Arecibo[Bernhardt et al., 1989], and uses such motions as a diagnostic of natural ionospheric drifts.

1.2 Contributions of This Thesis

This thesis contributes to the study of ionospheric heating because very few *in situ* measurements have been made to date. Our experiment package, with particle detectors made here at UNH and wave experiments from Cornell University and the Los Alamos National Laboratory, allowed us to directly observe ion fluxes, local electron density depletions with accompanying electric fields, superthermal electrons accelerated by the heater, the possible signature of a heater driven convection/current system, and, indeed, the reflection of the heater wave and its absence above the reflection height. In addition, we were able to detect coherent low frequency electrostatic waves in the vicinity of the Arecibo ISR beam, and observed the acceleration of ions by these waves.

There are few measurements of the ion temperature during HF heating [Isham et al., 1990]. It is straightforward, using an ISR, to measure T_i from the width of the ion line (Doppler shift by thermal ions) but the altitude resolution on such a measurement exceeds the thickness of the heated layer by an order of magnitude [Evans, 1969][Carlson et al., 1972]. It is also possible to infer the ratio T_e/T_i, and to plausibly separate this into T_e and T_i using a separate high resolution density measurement, since the backscattered power depends on both the density and the temperature ratio. This method is subject to contamination by the HF-enhanced ion line, and therefore this method has been applied only when there are no significant heater-induced enhancements of the ion line due to ion acoustic fluctuations[Djuth et al., 1987b]. In other words, under conditions when ion acoustic fluctuations (a likely ion heating mechanism) are strong, the ion temperature becomes difficult to measure.

Using a computer model of our ion detector, we are able to estimate the ion temperature in and above the heated region. We find temperatures in excess 3000 K while in the heater

beam, diminishing to 1500 K as we go above and to the west. Our results, however, are subject to serious ambiguities caused by unmodeled spacecraft wake effects. Other methods of which we are aware, which give ion temperatures of 800-1300 K, can either only infer the ion temperature indirectly, and only at times when it is likely to be low, or they are incapable of altitude-resolving the heated layer. The software detector also helps determine the level of spacecraft charging, which can then be used to infer the superthermal electron flux. We note that this flux is largest when the payload is most nearly magnetically connected to the center of the HF beam, followed closely by the time of magnetic connection to the ISR beam.

The d.c. electric field data is used in this experiment to investigate convection in the vicinity of the heated volume, and to put a lower limit on the temperature inside the heater-induced filaments [Kelley et al., 1995]. We find also a shear in the electric field as we exit the heater beam to the west. This shear is interpreted as the signature of the parallel return current for a current system driven by the heater beam. Furthermore, the direction of the $\vec{\mathbf{E}} \times \vec{\mathbf{B}}$ drift measured at the payload above the heater beam is shown to be not inconsistent with the picture of a plume of heater-energized ions drifting from the heater to the payload.

There is unfortunately no electron spectrum available from this payload, due primarily to the high level of spacecraft charging. Furthermore, the rocket which carried our experiment flew nearly 20° off azimuth, carrying us away from the center of the heater beam, slipping just inside the -3 dB contour at the reflection height. There is nevertheless a good deal to be learned from this unique experiment; this thesis is an attempt to do exactly that.

Chapter 2

The Zakharov Model

The microphysics of ionospheric heating near the plasma frequency is often understood in terms of the Zakharov model, which is a multiple time scale simplification of the standard two-fluid plasma equations [Chen, 1984]. The Zakharov model includes *some* of the inherent nonlinearity of the two-fluid plasma equations; enough to allow a coupling across widely separated time scales. We will consider a system in which quantities vary on two time scales: a fast or high-frequency scale, labeled by a subscript h, and a slow or low-frequency scale, labeled by a subscript l. For the experiment described in this thesis, the fast time scale can be associated with the heater wave frequency and directly driven responses, while the slow time scale contains the nonlinearly coupled low-frequency response of the plasma to the heater wave. We will see how a wave near the plasma frequency can drive low-frequency ion acoustic waves, through the nonlinear "ponderomotive force"[Chen, 1984].

I will first specify some of the notation to be used in this chapter. E, n, v, and m, with various subscripts, will be used to indicate electric fields, number densities, fluid velocities, and particle masses. $\tilde{E}_1$ is the envelope of the high frequency electric field response, V_e is the electron thermal velocity, ω_e is the electron plasma frequency, n is the plasma density, subscripted with e for electron, i for ion, and 0, h, or l for a background, high, or low-frequency quantity. $\tilde{E}_0$ is the driver wave amplitude, and $\Delta\omega$ is the difference between the

driver frequency ω_0 and the electron plasma frequency ω_e. The symbol c_s is the ion acoustic speed, e is the electronic charge, which is a positive number. A subscripted ∂ denotes partial differentiation with respect to the subscripted variable, $\langle - \rangle_x$ denotes a spatial average, a '*' means complex conjugation, and i is the imaginary number. The notation '$\tilde{x}$' indicates the magnitude of the oscillating quantity x. Gaussian units will be used throughout this chapter.

2.1 Assumptions and Physical Picture

The Zakharov model is based on five assumptions [Payne et al., 1984], which can be shown to hold reasonably well during the first several milliseconds following turn-on of an HF heater in the ambient F layer ionosphere [Cheung et al., 1989].

Assumption 1 *High and low frequencies are well-separated.*

Assumption 2 *Low-frequency motions are quasi-neutral.*

$$n_{el} \approx n_{il} \text{ and } v_{el} \approx v_{il}$$

Assumption 3 *High-frequency electrostatic wave energy density is much less than electron kinetic energy density.*

$$\frac{1}{8\pi}\left|\tilde{E}_1\right|^2 \ll \frac{1}{2}T_e n_e,$$

where the symbol $\tilde{E}_1$ is used for the envelope of the high-frequency electric response field.

This is equivalent to the statement that the high-frequency electron fluid quiver velocity ($\frac{qE_h}{m_e\omega}$) is much less than the thermal velocity for each species.

Assumption 4 *Low-frequency fluid speed is much less than high-frequency fluid speed times* $\left(\frac{m_e}{m_i}\right)^{\frac{1}{2}}$.

Assumption 5 *High-frequency length scales are smaller than, but on the same order as, low-frequency length scales.*

2.2 Derivation of the Zakharov Equations

The two equations of the one dimensional Zakharov model [Zakharov, 1972] can be written :

$$i\partial_t \tilde{E}_1 + \frac{3}{2}\frac{V_e^2}{\omega_e}\partial_x^2 \tilde{E}_1 = \frac{\omega_e}{2n_0}[n_{el}\tilde{E}_1 + \tilde{E}_0 \exp(-i\Delta\omega t) - \langle n_{el}\tilde{E}_1\rangle_x], \tag{2.1}$$

$$\partial_t^2 n_{il} - c_s^2 \partial_x^2 n_{il} = \frac{1}{4\pi m_i}\partial_x^2 \left[\left|\tilde{E}_1\right|^2 + \tilde{E}_0\tilde{E}_1^* \exp\left(-i\Delta\omega t\right) + \tilde{E}_0^*\tilde{E}_1 \exp\left(i\Delta\omega t\right)\right], \tag{2.2}$$

I would like to derive these two equations, starting with the usual fluid equations and the assumptions listed above. The derivation is given elsewhere[Nicholson, 1983][Payne et al., 1984], but with less explicit physical insight. The goal of the Zakharov model is to understand the coupling of a high-frequency wave field to low-frequency fluid plasma dynamics. There is no such coupling available in linear plasma theory, and, as we shall see, it arises here through the action of the ponderomotive force.

The one-dimensional fluid plasma equations, with quasi-neutrality already inserted, are:

- The electron and ion continuity equations.

$$\partial_t n_e + \partial_x(n_e v_e) = 0 \tag{2.3}$$

$$\partial_t n_i + \partial_x (n_i v_i) = 0 \tag{2.4}$$

- The electron force equation.

$$\partial_t v_e + v_e \partial_x v_e = -\frac{eE}{m_e} - \frac{\gamma_e T_e}{n_e m_e} \partial_x n_e \tag{2.5}$$

- The ion force equation.

$$\partial_t v_i + v_e \partial_x v_e = \frac{eE}{m_i} - \frac{\gamma_i T_i}{n_i m_i} \partial_x n_i \tag{2.6}$$

- Poisson's equation.

$$\partial_x E = 4\pi e (n_i - n_e) \tag{2.7}$$

In these equations and those that follow, E means the total electric field, and v is a fluid velocity. The symbol γ is the ratio of specific heats, a constant relating fractional pressure changes to fractional density changes. T_e and T_i refer to the electron and ion thermal energies, with Boltzmann's constant absorbed. The subscripts e and i refer to the electron and ion components of the plasma, and the subscripts l and h indicate whether the subscripted quantity varies on the low or high-frequency time scale.

First I will separate each variable into its equilibrium value plus the low and high-frequency components of its fluctuations. The fluid velocities, density gradients, and forces all vanish in equilibrium, so we have $v_0 = 0$, $\partial_x n_0$, and $E_0 = 0$. I will ignore high-frequency fluctuations of the sluggish ion fluid in comparison to those of the electron fluid.

$$n_e = n_0 + n_{eh} + n_{el} \tag{2.8}$$

$$n_i = n_0 + n_{il} \tag{2.9}$$

$$v_e = v_{eh} + v_{el} \tag{2.10}$$

$$v_i = v_{il} \tag{2.11}$$

$$E = E_l + E_h \tag{2.12}$$

I will begin deriving 2.1 by taking the time derivative of the high-frequency part of 2.3. Substituting 2.8 into 2.3 gives:

$$\partial_t[n_0 + n_{el} + n_{eh}] + \partial_x[(n_0 + n_{el} + n_{eh})(v_{el} + v_{eh})] = 0.$$

By assumption 4, we can immediately drop v_{el} in comparison with v_{eh}. Then, taking only the high-frequency terms:

$$\partial_t n_{eh} + \partial_x[n_0 v_{eh} + n_{el} v_{eh}] = 0. \tag{2.13}$$

It might at first seem that there should be a term $n_{eh}v_{eh}$ in the preceding equation. It is worthwhile to show why this term is dropped in deriving the Zakharov model. First of

all, the product of two factors, both of which are oscillating near the plasma frequency, has two harmonic components: one near zero frequency and the other near twice the plasma frequency. The preceding equation must balance with terms oscillating near the plasma frequency in this multiple scale analysis.

However, perhaps the term $n_{eh}v_{eh}$ should be included in the low frequency continuity and momentum equations, since it will have a low frequency component. We can give an order of magnitude argument for why this is not necessary [Newman, 1996].

Consider the linearized, high-frequency electron continuity equation

$$\omega\tilde{n}_{eh} = kn_0\tilde{v}_{eh}$$

for a Langmuir wave with frequency ω near ω_e and wavenumber k. From the dispersion relation

$$\omega^2 = \omega_e^2 + 3k^2{V_e}^2,$$

we can see that the wavelength for such a wave is much larger than the Debye length λ_D . Therefore, since $V_e = \omega_e\lambda_D$, we can write:

$$\frac{\tilde{n}_{eh}}{n_0} = k\lambda_D\frac{\tilde{v}_{eh}}{V_e}.$$

Since $k\lambda_D \ll 1$, this is equivalent to the usual statement that the high-frequency density perturbation is much smaller than the high-frequency velocity perturbation in the natural dimensionless units [Goldman, 1984]. Note that this can be written approximately as

$$\frac{\tilde{n}_{eh}}{n_0} \sim \frac{\tilde{v}_{eh}}{\omega_e L},$$

where $L(\approx 1/k)$ is the length scale associated with either high or low-frequency quantities (see assumption 5)

Now consider the low-frequency electron momentum equation,

$$\partial_t v_{el} = \frac{-eE_l}{m_e} - \frac{\partial_x p_e}{m_e n_0} - v_{eh}\partial_x v_{eh}.$$

For a linear ion-acoustic wave, the first two terms on the right-hand side cancel each other. This leaves, for a weakly nonlinear wave, the magnitude equation

$$\Omega \tilde{v}_{el} \sim -\frac{\tilde{v}_{eh}^2}{L},$$

where L is the approximate length scale for processes on both time scales (see assumption 5), and Ω is the "low" frequency.

Finally, examine the low-frequency continuity equation:

$$\frac{\Omega \tilde{n}_{el}}{n_0} \sim -\frac{\tilde{v}_{el}}{L} - \frac{\tilde{n}_{eh}}{n_0}\frac{\tilde{v}_{eh}}{L}.$$

From the previous paragraphs, we can substitute in for $\tilde{v}_{el}$, obtaining:

$$\frac{\Omega \tilde{n}_{el}}{n_0} \sim -\frac{\tilde{v}_{eh}^2}{L^2}\left(\frac{1}{\Omega} - \frac{1}{\omega}\right),$$

from which it is clear (see assumption 1) that the first term on the right hand side dominates the term which came from $n_{eh}v_{eh}$, so we drop $n_{eh}v_{eh}$. Note that for a model appropriate to lower-hybrid turbulence and solitary structures [Lynch et al., 1994], the separation of time scales is considerably smaller, and it turns out that the $n_{eh}v_{eh}$ nonlinearity is important and must be retained[Newman, 1996].

So we have, taking the time derivative of the high-frequency electron continuity equation:

$$\partial_t^2[n_{eh}] + \partial_{xt}^2[n_0 v_{eh} + n_{el} v_{eh}] = 0.$$

Now I take the high-frequency part of equation 2.5.

$$\partial_t v_{eh} + (v_{el}\partial_x v_{eh} + v_{eh}\partial_x v_{el} + v_{eh}\partial_x v_{eh}) = \frac{-eE_h}{m_e} - \frac{\gamma_e T_e}{(n_0 + n_{el} + n_{eh})}\frac{\partial_x n_e}{m_e}$$

In the denominators n_{el} and n_{eh} are ignored in comparison with n_0. The relative size of the terms on the left hand side can be estimated as follows. The high-frequency terms can be taken to be oscillations near the plasma frequency, so $\partial_t v_{eh} \sim \omega_e v_{eh}$, while each convective term contributes approximately $v_{eh}v_{el}/L$, where L is the gradient scale length for high and low-frequency fluctuations (see assumption 5). So, the left-hand side (LHS), goes as:

$$LHS \sim v_{eh}(\omega_e + \frac{2v_{el}}{L}),$$

or

$$\sim v_{eh}(\frac{V_e}{\lambda_D} + \frac{2v_{el}}{L}).$$

Assumption 3 implies that $v_{eh} \ll V_e$, while assumption 4 states that $v_{el} \ll v_{eh}$, therefore we have $v_{el} \ll V_e$. Furthermore, the assumption of widely separated time scales (assumption 1) implies a relatively monochromatic high-frequency wave, i.e., one with a slowing-varying spatial envelope. In other words, we have $L \gg \lambda_D$. For these reasons, Zakharov drops the convective terms in comparison with the partial time derivative in the electron and ion force equations. This leaves:

$$\partial_t v_{eh} = \frac{-eE_h}{m_e} - \frac{\gamma_e T_e}{n_0}\frac{\partial_x n_e}{m_e}. \tag{2.14}$$

Now consider the convective term from the electron continuity equation. By assumption 4, we can ignore v_{el} in comparison with v_{eh}. In taking the time derivative of the convective term in the electron continuity equation, we can neglect the time dependence of the low-frequency quantities, and move the ∂_t through to act on v_{eh} only:

$$\partial_{xt}^2[(n_0 + n_{el})v_{eh}] = \partial_x[(n_0 + n_{el})\partial_t v_{eh}].$$

This can be substituted back into 2.13, along with $\partial_t v_{eh}$ from equation 2.14, to give:

$$\partial_t^2 n_{eh} - \partial_x[(n_0 + n_{el})\left(\frac{eE_h}{m_e} + \frac{\gamma_e T_e}{m_e n_0}\partial_x n_{eh}\right)] = 0.$$

Looking back at Poisson's equation, using quasi-neutrality, and ignoring high-frequency ion motions, we get:

$$\partial_x E_h = -4\pi e n_{eh}.$$

This can be inserted into the previous equation to eliminate n_{eh} in favor of E_h, yielding:

$$\partial_x\left[\partial_t^2 E_h + (n_0 + n_{el})\left(\frac{\omega_e^2}{n_0}E_h - \frac{\gamma_e T_e}{m_e n_0}\partial_x^2 E_h\right)\right] = 0.$$

Note that the only high-frequency quantity in this equation is E_h.

Now the high-frequency electric field can be expressed as the sum of an applied field E_{ext} and a response field E_1. We will assume the external field to be spatially uniform, and the response to average to zero over the volume of interest. So, we insert $E_h = E_{ext} + E_1$,

into the previous equation, yielding

$$\partial_x \left[\partial_t^2 E_1 + \omega_e^2 E_1 + \frac{n_{el}}{n_0}\omega_e^2 E_1 - \frac{\gamma_e T_e}{m_e}\partial_x^2 E_1 - \frac{\omega_e^2}{n_0} n_{el}(E_1 + E_{ext}) \right] = 0,$$

where I have already made use of $\partial_x E_{ext} = 0$. This equation can be integrated over x, resulting in:

$$\partial_t^2 E_1 + \omega_e^2 E_1 + \frac{n_{el}}{n_0}\omega_e^2 E_1 - \frac{\gamma_e T_e}{m_e}\partial_x^2 E_1 - \frac{\omega_e^2}{n_0} n_{el}(E_1 + E_{ext}) = f(t),$$

where $f(t)$ is an as yet undetermined function of time, an "integration constant" for the x-integration. We can now evaluate $f(t)$ by performing a spatial average. One term alone survives, yielding:

$$f(t) = \frac{\omega_e^2}{n_0}\langle n_{el} E_1 \rangle_x.$$

The response and driver fields can each be written as the product of a modulation envelope and an oscillation at a dominant "high" frequency, i.e.

$$E_1 = \tilde{E}_1 e^{i\omega t} + c.c.$$

and

$$E_{ext} = \tilde{E}_0 e^{i\omega_0 t} + c.c.,$$

where "+c.c." indicates that the complex conjugate is being added on to give a real result. Note that the modulation envelopes $\tilde{E}_1$ and $\tilde{E}_0$ are slowly-varying quantities. Therefore, in taking the second time derivative of E_1, we ignore $\partial_t^2 \tilde{E}_1$ in comparison with $2i\omega_e \partial_t \tilde{E}_1$, while the term $-\omega_e^2 \tilde{E}_1$ cancels with the second term in the previous equation. The result

can be written

$$e^{-i\omega_e t}\{i\partial_t \tilde{E}_1 - \frac{n_{el}}{2n_0}\omega_e \tilde{E}_0 e^{-i\Delta\omega t} - \frac{n_{el}}{2n_0}\omega_e \tilde{E}_1 + \frac{3}{2}V_e{}^2\partial_x^2 \tilde{E}_1 + \frac{\omega_e}{2n_0}\langle n_{el}\tilde{E}_1\rangle_x\} + c.c.,$$

where $\Delta\omega \equiv \omega_0 - \omega$, and γ_e has been taken to be 3, in this one-dimensional model.

In the Zakharov model, we use the somewhat more restrictive, but still informative:

$$i\partial_t \tilde{E}_1 - \frac{n_{el}}{2n_0}\omega_e \tilde{E}_0 e^{-i\Delta\omega t} - \frac{n_{el}}{2n_0}\omega_e \tilde{E}_1 + \frac{3}{2}V_e{}^2\partial_x^2 \tilde{E}_1 + \frac{\omega_e}{2n_0}\langle n_{el}\tilde{E}_1\rangle_x = 0.$$

Any (E_h, n_{el}) which solves this complex equation will also solve the preceding real equation.

It is in the second Zakharov equation where the ponderomotive force appears. The force equations can be written as

$$m_{e,i}\partial_t v_{e,i} = q_{e,i}E - \gamma_{e,i}T_{e,i}\frac{\partial_x n_{e,i}}{n_{e,i}},$$

where, as discussed above, the convective terms on the left-hand side have been dropped in comparison with the partial time derivative. We will now perform a time average on this equation, over the fast timescale, over an interval such that v_{eh} averages to zero. This procedure preserves low-frequency terms as though they were constants, and allows for a non-zero time-average of the high-frequency fluid element position, and therefore a non-zero average of E_h, which is a function of position. The result is

$$m_e n_0 \partial_t v_{el} = \gamma_e T_e\, \partial_x n_{el} - e n_0(E_l + \langle E_h\rangle_t),$$

for electrons, and

$$m_i n_0 \partial_t v_{il} = \gamma_i T_i \, \partial_x n_{il} + e n_0 (E_l + \langle E_h \rangle_t),$$

for ions.

Consider the term $\langle E_h \rangle_t$. E_h can be written as the product of a spatial dependence and an oscillation (as above), with a simplified notation and choice of phase:

$$E_h = E(x) \cos \omega t \approx (E(x_0) + \delta x \cdot \frac{dE}{dx}|_{x_0}) \cos \omega t,$$

(where x_0 is the position of the fluid element at $t = 0$), so the time average yields:

$$\langle E_h \rangle_t \approx 0 + \partial_x E|_{x_0} \langle \delta x \cos \omega t \rangle_t.$$

The quantity δx can be approximated, to first order, as the "quiver motion" of a charge in an oscillating electric field, i.e.

$$\delta x \approx \frac{-qE(x_0)}{m\omega^2} \cos \omega t.$$

Inserting this into the equation for E_h, we find

$$\langle E_h \rangle_t = -\frac{q_{e,i}}{4 m_{e,i} \omega^2} \partial_x |E|^2|_{x_0},$$

which is the ponderomotive force. Inserting this into the force equations, adding the two equations together, and using quasi-neutrality ($n_{il} \approx n_{el}$ and $v_{il} \approx v_{el}$), we obtain:

$$(m_e + m_i) n_0 \partial_t v_{el} = -(\gamma_e T_e + \gamma_i T_i) \partial_x n_{el} - \frac{e^2}{4\omega^2} \partial_x |\tilde{E}_1|^2 \left(\frac{1}{m_e} + \frac{1}{m_i} \right).$$

Using $m_e \ll m_i$, $c_s^2 \equiv (\gamma_e T_e + \gamma_i T_i)/m_i$, $\omega \approx \omega_e$, $\omega_e^2 \equiv 4\pi n_0 e^2/m_e$, and $\partial_t n_0 = 0$ we get:

$$\partial_t(n_0 v_{el}) = -c_s^2 \partial_x n_{el} - \frac{1}{16\pi m_i}\partial_x |E_h|^2.$$

Now we take the derivative of this equation with respect to x, and use $\partial_x(n_0 v_{el}) = -\partial_t n_{el}$ from the low frequency continuity equation, which yields:

$$\partial_t^2 n_{el} - c_s^2 \partial_x^2 n_{el} = \frac{1}{16\pi m_i}\partial_x |E_h|^2,$$

which, after expanding E_h, becomes the second equation of the Zakharov model.

Having thus shown how the ponderomotive force enters the two-fluid plasma equations, it is interesting to compare the ponderomotive force to the ordinary gas pressure force. Both forces are the time-averaged result of a large number of tiny impulses, the sum total of which may yield a net push in a particular direction. The gas pressure force, however, is made of stochastic and spatially localized impulses, which occur on time scales which are *much* shorter than the timescale for any bulk motions of the gas. The ponderomotive force, on the other hand, is clearly made of periodic (differentiable!) impulses, which are spatially extended, and often occurs at time scales corresponding to collective plasma motions such as Langmuir or lower hybrid waves.

So, we have now shown in detail how one arrives at the Zakharov equations:

$$i\partial_t \tilde{E}_1 + \frac{3}{2}\frac{V_e^2}{\omega_e}\partial_x^2 \tilde{E}_1 = \frac{\omega_e}{2n_0}[n_{el}\tilde{E}_1 + \tilde{E}_0 \exp(-i\Delta\omega t) - \langle n_{el}\tilde{E}_1\rangle_x],$$

$$\partial_t^2 n_{el} - c_s^2 \partial_x^2 n_{el} = \frac{1}{4\pi m_i}\partial_x^2 \left[\left|\tilde{E}_1\right|^2 + \tilde{E}_0\tilde{E}_1^* \exp(-i\Delta\omega t) + \tilde{E}_0^*\tilde{E}_1 \exp(i\Delta\omega t)\right].$$

The real part of the first equation describes the time evolution of the envelope of the high-

frequency electric field, with a term indicating the influence of the driver field $\tilde{E}_0$, and two terms describing the impact of the low-frequency density perturbation. The left-hand side of the second equation describes the free propagation of linear ion acoustic waves; the right-hand side then acts as a source term for such waves. The equation indicates that ion acoustic waves are launched from wherever there is a divergence in the ponderomotive force.

Such a divergence might occur, for example, at the reflection height of a MHz radio wave propagating upwards into the ionosphere, or indeed at the edge of any intense beam of electromagnetic radiation in a plasma. Note that in this derivation, we assumed that the wave frequency ω was equal to the electron plasma frequency ω_e. This simplified the appearance of the resulting model, and is appropriate near the reflection height of a heater wave, the so-called "critical layer." The model can also be applied at higher frequencies, by including a factor $(\omega_e/\omega)^2$ in front of the ponderomotive source term. This will be done in this thesis in order to speculate about possible ponderomotive effects at the edge of the Arecibo ISR beam, which operates at 430 MHz.

The Zakharov model continues from here by noting a singularity in the two equations derived above. After a finite time t_c, with density cavities being dug by the ponderomotive force, and waves being trapped in these cavities, the Zakharov equations predict an explosive (infinite) growth of the electric field envelope $\tilde{E}_1$. At t_c, then, these equations are clearly not valid, and the ensuing kinetic plasma physics can only be described by difficult and computationally intensive computer simulations [Zakharov et al., 1989]. The main prediction of such simulations is that the energy of the incident waves is dissipated abruptly at times near t_c in the acceleration of electrons to several times their thermal energy. This process is then thought to begin again, in the now somewhat depleted cavity regions.

Within the Arecibo HF heater beam, it is thought that something like this process

probably occurs throughout the center of the HF interaction region. The cavities mentioned above, under conditions typical over Arecibo, would be some tens of centimeters in size, and would survive (cycle) for a t_c of about 100 μs. When the experiment described in this thesis was in the funding proposal stage, we hoped that it would be possible to observe these sort of kinetic effects with our particle detectors, and to observe spiky electric fields and density depletions with various antennas and probes.

Once the data had been gathered, however, it became clear that these microphysical processes were still somewhat beyond our measurement capabilities, even if we had passed directly through the HF interaction region. And so the data analyzed in this experiment make contact with the Zakharov model only in the sense that they will be interpreted in terms of the ponderomotive force, and that we can, perhaps, remotely sense collapse-accelerated superthermal electrons.

Chapter 3

A Rocket Through the Heater Beam

While there exists a fairly large body of radar observations of the heated F layer ionosphere, the number of *in situ* measurements remains small. *Rose et al.* made measurements of heater-induced Langmuir waves, density fluctuations and electron temperatures with a rocket-borne probe [Rose et al., 1985] , and more recently *Bernhardt et. al.* flew a payload similar to ours through the Arecibo heater beam, performing a chemical release [Bernhardt et al., 1995] . Using information gathered by [Rose et al., 1985], we attempted to design a particle diagnostic package capable of seeing meter-scale density fluctuations, microsecond bursts of energetic electrons, and wave-particle correlations. These tasks were to be accomplished by three particle detectors on board the spacecraft: two high geometric factor detectors looking along the magnetic field, one for ions, one for electrons, and one pitch angle imaging electron detector. Our efforts were primarily focused on detecting the signatures of caviton collapse [Zakharov et al., 1989][DuBois, 1991].

Overall, the experiment consisted of three main parts: an HF heater, a diagnostic radar, and an instrumented rocket payload. The role of the HF heater was to boil the ionosphere at its reflection altitude somewhere in the F region. The diagnostic radar was the 430 MHz incoherent scatter radar of the famous Arecibo observatory, used here to find the HF-heated region, so that our rocket could be flown directly into it.

3.1 Special Note: There are Two Transmitters!

It is crucial for the understanding of this experiment to realize the distinction between the HF heater and the diagnostic radar. The HF heater operates at 5.1 MHz, illuminates a 100 km diameter region below the F peak, and is some 30 km west of the launch site, near the town of Islote. On the other hand, the radar operates at 430 MHz, probing a spot less than 1 km in diameter in the F layer, and is 36 km southwest of the launch site. Their intended purposes are quite different as well. The HF heater is meant to resonate with F layer plasma and violently heat it, while the radar is simply intended to *look* at the HF heating. The diagnostic radar is variously called "Arecibo", "the ISR", or just "the radar", but never anything with "HF" or "heater" in it. Similarly, the HF heater is sometimes called "the HF beam", or "the heater beam" but the word "radar" is never applied to it. The heater is, in fact, *not* a radar; it has no receiving capability. Confusion often arises in discussions of this experiment, primarily because one of its more exciting results is in fact the unexpected perturbation of the plasma environment by the ISR beam! The radar is not supposed to interact measurably with the ionospheric plasma, but in fact it appears to do exactly that. Furthermore, early heating experiments at Arecibo, before the building of the present heating facility, used a heating transmitter suspended above the radar dish!

3.2 Flight Geometry

Soliton was launched on June 9, 1992 at 7:31:13 UT, from pad 2 at NASA's Tortuguero launch facility, on a Black Brant IX. It flew approximately 20 degrees SW of its intended azimuth, passing through the reflection altitude of 268 km about 18 km west of the heater beam center. The reflection altitude was passed at the extreme westward edge of the heater

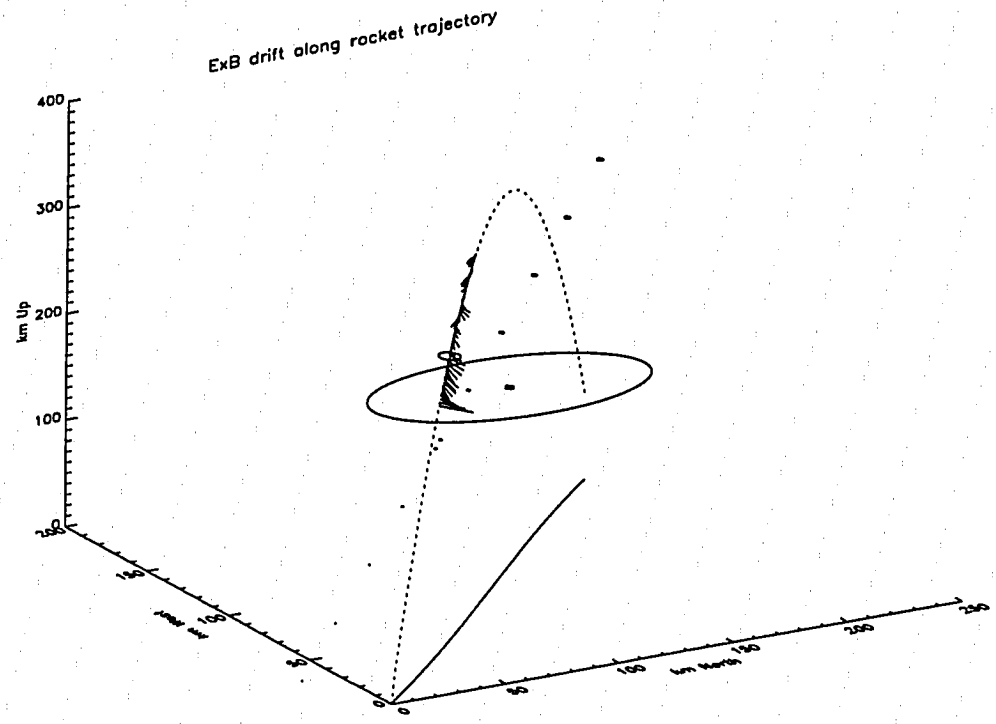

Figure 3-1: *The geometry of the Soliton flight.* The trajectory begins at the origin, and has convective drift vectors attached during part of the upleg. The half-power contour of the HF heater at its reflection height is the large ellipse with a diamond in its center. A small circle indicates where the rocket passed through the reflection height (268 km) of the HF beam, just outside the half-power contour. The tiny circles, beginning just left of the origin and proceeding up and to the right, are the half-power contours of the ISR beam. The trajectory comes nearest the ISR beam at 200 km altitude.

beam. The reflection of the heater and the edges of its radiation pattern have similar gradient scale lengths, and it may not always be clear whether a given feature in the data is due to vertical or horizontal gradients in the heater wave power. Soliton flew to an apogee of 359 km. On the upleg, at 207 km altitude, the payload passed serendipitously close to the Arecibo incoherent scatter radar (ISR) beam. Figure 3-1 shows the trajectory and its location with respect to the HF heated region and the ISR beam.

3.3 The Heater

The Arecibo heater is located at 18.476 N, 66.667 W. It consists of a rectangular array of horizontal elements, upheld by towers, covering a swampy 54 acres. In this experiment the array was phased such as to produce the maximum radiation at an angle of twelve degrees from local vertical, due north of the heater facility. The radiation was an electromagnetic O-mode with a frequency of 5.1 MHz. Heater wave intensity is often expressed in terms of *effective radiated power* (ERP), which simply means the power input which would be required *if* the heater achieved its peak Poynting flux in every direction (4π steradians). Use of the ERP allows a quick calculation of the peak Poynting flux, or the peak electric field magnitude, as a function of distance from the heater. The ERP from Arecibo during this experiment was 60 MW, corresponding to a peak electric field magnitude of ~ 1 V/m at the reflection height of 268 km.

3.4 Arecibo 430 MHz Incoherent Scatter Radar

The Arecibo ISR is located at 18.344 N, 66.753 W. It has a 300 meter diameter fixed spherical dish, and pointing is achieved by moving the line feed to the appropriate azimuth and elevation. During our experiment, the peak output power was somewhat less than 2 MW, at a frequency of 430.0 MHz, a pulse width of 52 μs, and a time between pulses (IPP) of 11 ms. Note that the ERP of the radar is on the order of 8 TW, over 100 times that of the heater. Although Arecibo is capable of measuring a bewildering array of ionospheric parameters, on the night of our flight it measured only the total backscattered power in the ion line as a function of time or virtual range, which is, in the absence of temperature gradients, proportional to the electron density [Evans, 1969].

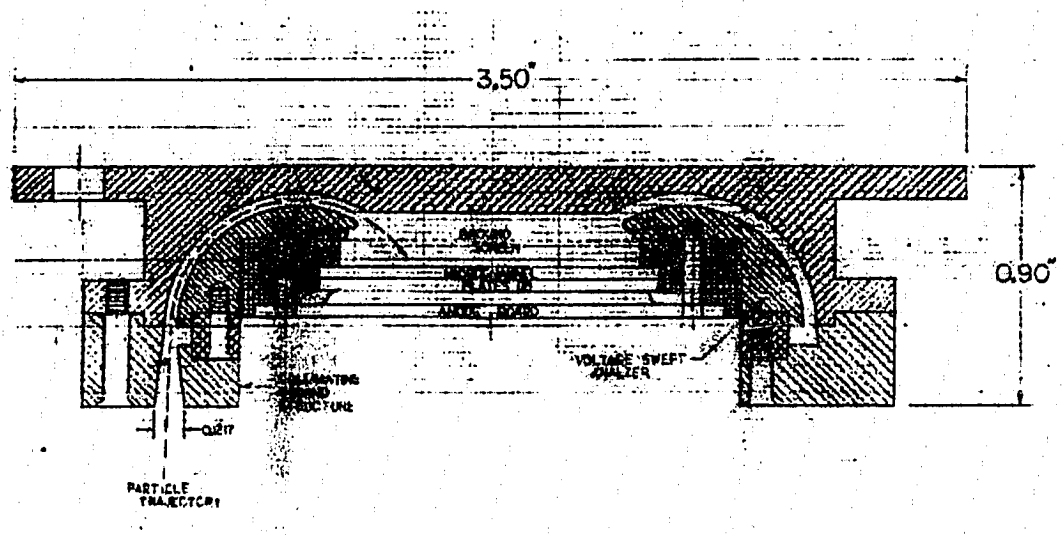

Figure 3-2: *Mechanical drawing of the ion Bagel.* The real Bagel can be visualized by rotating this picture around an axis running up the page through the center of the drawing in the plane of the paper.

3.5 Particle Detectors

3.5.1 The Ion Bagel

The particle detector whose data are presented in this thesis is called the Ion Bagel, named for the shape of its energy selection, or analyzer, plates. A schematic drawing of the detector is seen in figure 3-2. The Ion Bagel's field of view is an approximately 10^o half-angle cone which was aligned along the spacecraft symmetry or spin axis. It was intended that this detector look at particles approximately anti-parallel to the geomagnetic field. However, a substantial spacecraft wobble ($\sim$ 60 degrees) caused its field-of-view to swing from nearly anti-parallel to forty-five degrees away from anti-parallel with a period of $\sim$ 30 seconds. The ion Bagel's maximum count rate was limited by its counting electronics to around 600 kHz.

The Bagel's intended function was to look at fast timescale processes over a narrow

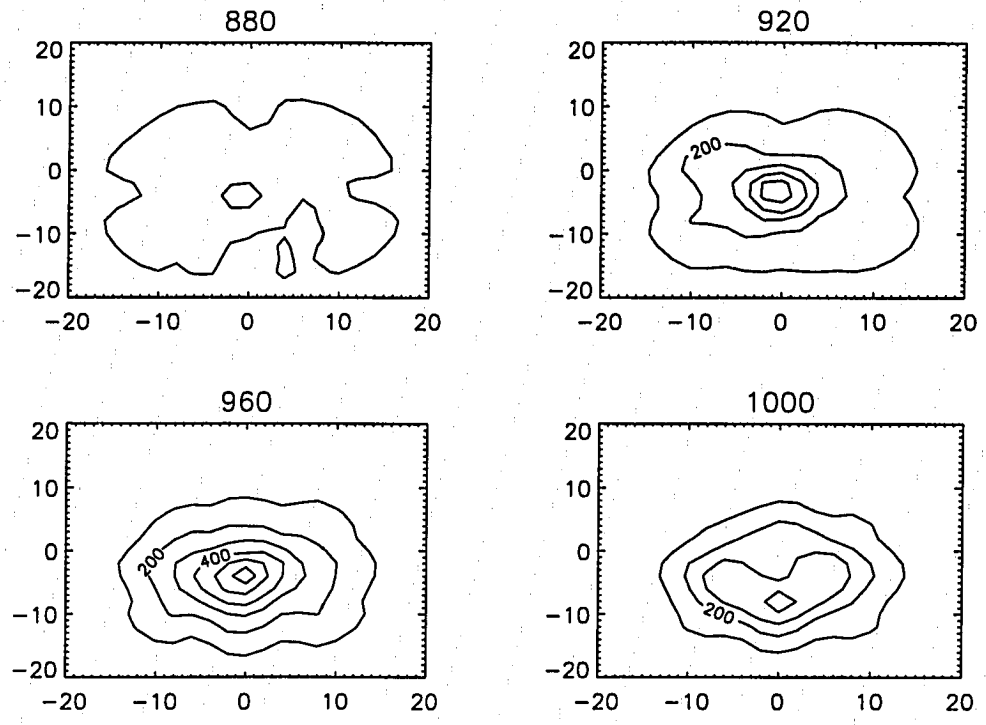

Figure 3-3: *Response of the Bagel to 4 keV electrons.* Each plot shows the angular dependence of the response function at a particular analyzer voltage, in volts, which is displayed in the title. The axes are in degrees, the contour levels are total counts. The displacement of the response away from normal incidence corresponds to the deflection of the calibration beam in the Earth's magnetic field.

(and unresolved) angular field-of-view. In this case, we were hoping to see superthermal electrons (and perhaps ions) expelled in caviton collapse events. Another application might be resolving the fine structure of auroral parallel electron precipitation. The Bagel trades away fine angular resolution and wide view in favor of high sensitivity, fast time resolution and fine energy resolution [Decreau et al., 1975]. Figure 3-3 shows some views of the Soliton electron Bagel's measured response function. The "volume" of this response function, or "geometric factor", is 0.0015 cm^2-ster-eV/eV.

The Soliton ion Bagel was operated in two distinct sweep, or energy sampling, modes. The same energy steps were sampled in each mode, but at different rates. During the teleme-

try (TM) burst mode, the ion Bagel sampled each energy step four times before switching to the next step. This feature can be exploited to examine the statistical fluctuation level as a function of energy as described in section 5.9. Each sample was an accumulation of counts for 0.81 ms. On the other hand, during TM engineering, post-burst and data dump modes, the Bagel sampled each energy step only once before switching to the next. The accumulation time in this sweep mode was 1.02 ms.

The ion Bagel was in burst mode while the spacecraft was in the heater beam, switched to post-burst mode at 170 seconds, just after leaving the heater, and entered data dump mode at 230 seconds. At 240 seconds, there was a destructive failure of the Bagel's high voltage power supply, so no data is available after that time.

It is important to realize that aspiring to detect individual cavitons with this type of detector is somewhat naïve. Cavitons are thought to have scale sizes of less than 0.5 meter and lifetimes of $\sim 100\mu s$. So, a caviton lifetime is short compared to the time required to accumulate counts. Furthermore, the Bagel draws the particles for each of its samples from a finite region of space at least as large as the thermal ion velocity (slowest relevant) times the accumulation time; in this case a few meters.

3.5.2 The Electron Detectors

Soliton carried two electron detectors: an electron Bagel and a Shrunken Electrostatic Analyzer (SESA). The electron Bagel is identical to the ion Bagel; it measures electrons because its analyzer plates are biased appropriately, with polarity opposite that of the ion Bagel. The SESA is rather different, however. It has several discrete bins which respond to particles arriving from various directions near the same plane. Our intent was to orient the spacecraft such that $\vec{B}_0$ would lie in this plane. In that case the discrete bins become pitch-

angle bins. The SESA was mounted on a telescoping tube, and during the flight extended outwards perpendicular to the spacecraft spin axis, as shown in figure 4-14.

3.6 Electric Field and Density Experiments

Electric fields were measured by double-probes of various lengths and orientations. Figure 5-10 shows the relative size and location of these. Many diagnostics were fed from these booms. Some channels were mixed down to give a bandwidth bracketing the heater frequency, while others were just linear samplings of the potential between pairs of spheres, in a few bands covering 0-20 kHz. In this thesis, our main concern will be with the d.c. electric field experiment, called V1-2 in figure 5-10.

A single fixed-biased Langmuir probe (#5) was used to measure the electron density. Probe (#6) unfortunately had a mechanical failure and never deployed. It was held at 3.0 volts with respect to the payload deck structure, and sampled in two different ways, both with a linear gain, but one at 90 ksamples/s, 8 bit resolution (CAV5), the other at 2 ksamples/s with 12 bit resolution (CAV5'). CAV5 has been used to investigate density depletions at the 10-m scale near the HF reflection height [Kelley et al., 1995], and in this thesis CAV5' will be used to lend credibility to low-frequency ISR generated waves. The higher dynamic resolution of CAV5' is needed to detect the small coherent fluctuations near the ISR beam. From this point on, CAV5' will be called simply "the probe", or perhaps, unfortunately, CAV5. The probe also gives an independent indication of the spacecraft potential. Since the probe cannot collect electrons unless it is positive with respect to the surrounding plasma, we interpret the moment when it begins drawing electron current as being the time when it *first* becomes plasma positive. The probe is held at 3.0 volts positive with respect to the spacecraft, so the spacecraft potential is taken to be -3.0 volts at this

time (see section 5.2, figure 5-6).

3.7 The F Layer Ionosphere

The F layer ionosphere consists primarily of neutral gas at a temperature of approximately 1000 K [Kelley, 1990] and a density of approximately 10^{14} m^{-3}. The dominant constituents of the neutral gas are molecular nitrogen and atomic oxygen, with approximately twice as much oxygen as nitrogen.

While the composition is dominated by neutrals, a charged particle density of 10^{11} m^{-3} plays a crucial role in the dynamics. In this thesis, we will be concerned only with charged particles. The dominant species in our altitude range of 200-300 km are electrons and singly ionized atomic oxygen.

In the vicinity of the HF reflection layer, the plasma frequency and the heater frequency are the same, indicating a plasma density of 3.2×10^{11} m^{-3}. The temperature of both species, without the heater, is generally accepted to be on the order of 1000 K or 0.1 eV. This gives a plasma "beta", the ratio of thermal to magnetic pressure, of approximately 10^{-5} . The convective drift in this region is typically 100 m/s or less.

The dip angle over Puerto Rico is 48 degrees, and the field strength in the F region varies from 0.34-0.36 gauss, corresponding to an electron gyrofrequency of 0.8-1.0 MHz. The gyrofrequency is on the same order as the 5.1 MHz heater frequency, a fact which complicates the interpretation of some of our data [Nicholson, 1977].

Chapter 4

Results: A Tale of Two Beams

Several features stand out in the raw particle, field and density data and will be analyzed in detail in this thesis. All the data contain surprises, as might be expected for a new *in situ* experiment. First, the ion data show a high and time-variable level of spacecraft charging, as well as heating and acceleration by not only the HF heater *but also by the ISR beam!* The D.C. electric field data show a shear as we exit the heated region, which we interpret as the signature of a ponderomotively driven current system and convection around the heated volume. The fixed-bias density probe shows momentary bite-outs corresponding to 10-meter scale quasi-steady field aligned filaments (FAI) induced by the HF beam[Kelley et al., 1995]. There are corresponding double-pulsed signatures of these filaments (in the D.C. electric field data), which are in fact a measure of the temperature gradient in the heater induced filaments. Both the electric field and density instruments show remarkable coherent perturbations near the ISR beam. I will first discuss the data from each instrument, and then proceed to use them to paint pictures of the two distinct perturbed plasma environments encountered by Soliton: the vicinities of the HF and ISR beams.

4.1 Particle Data

The particle data on Soliton came from three detectors: the ion and electron Bagels, and an electron SESA. Of these three, only the ion Bagel produced reasonable differential energy flux (count-rate) spectra. The electron detectors were both disappointingly silent, as will be discussed in more detail below.

Particle data are most conveniently displayed as an energy-time spectrogram. This type of picture shows time along the horizontal axis, energy along the vertical, and is shaded or colored to show the intensity of the flux at different sampled energies as a function of time. Figure 4-1 shows a summary of the ion data, while figure 4-2 shows some typical electron data for Soliton.

4.1.1 Data from the Ion Bagel

The data in figure 4-1 contain some features typical of ions in the F layer ionosphere. For example, the dominant feature is clearly the thermal ions, which appear as a long, meandering red stripe. The width of this stripe indicates a temperature of a fraction of an eV, although the exact value of the temperature can only be obtained through a careful deconvolution of the phase space density from the detector's response, as detailed in section 5.2.

The thermal ions are measured at an apparent energy which is considerably larger than the expected thermal energy of 0.1 eV. This is because the spacecraft is charged negatively, to a potential corresponding to the energy at the lower edge of the red stripe. All ions collected by the spacecraft fall through this potential, and pick up this extra kinetic energy.

Crudely speaking, one expects the count rate, for a Maxwellian plasma, to have a maximum at $E = 2T$ (see section 5.3), where E is the sampled particle energy and T is the

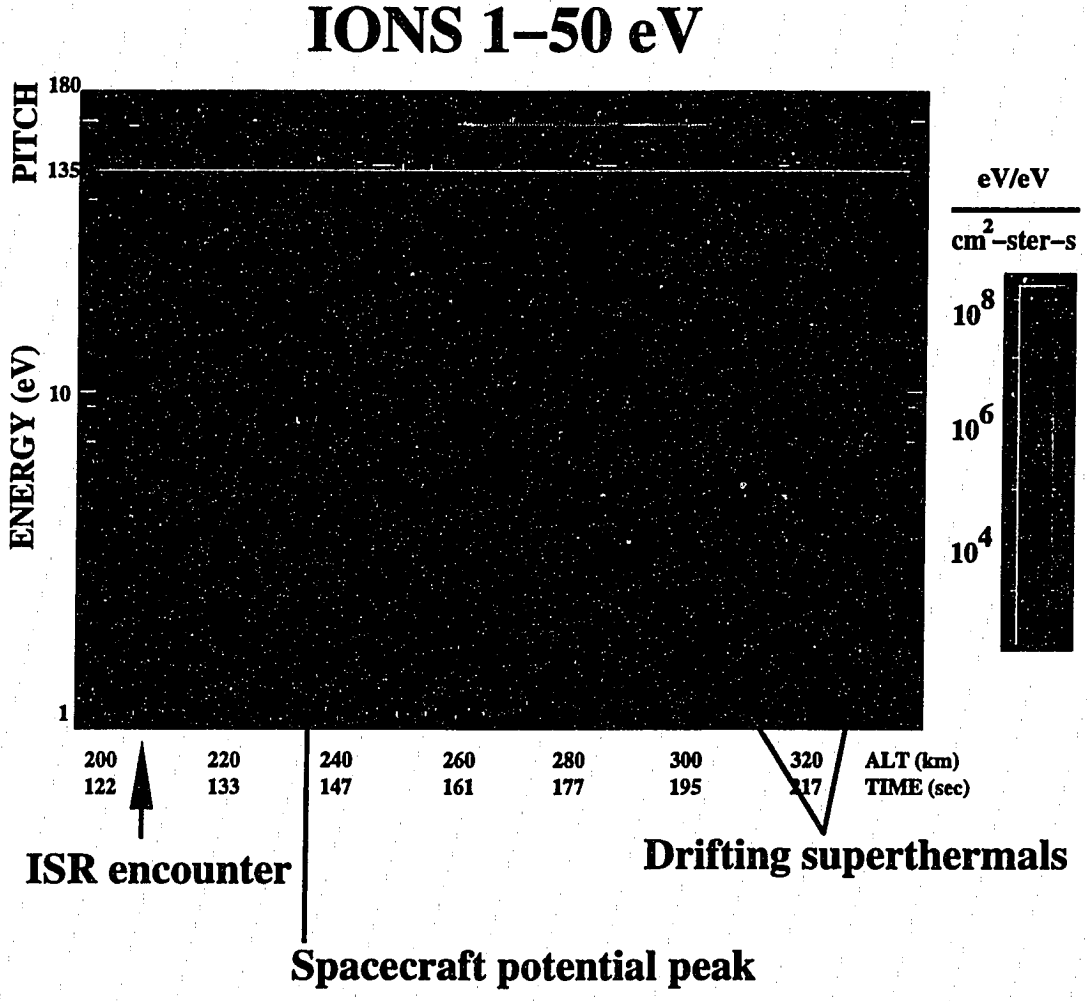

–Passing within a few kilometers of the Arecibo 430 MHz beam, Soliton saw superthermal ions and 10 Hz electrostatic waves.

–The spacecraft potential can be inferred from the ion fluxes; and is related to the characteristic energy of HF–energized electrons.

–Above reflection height, superthermal ions are observed drifting past the spacecraft from the HF interaction region.

Figure 4-1: *Ion survey spectrogram.*

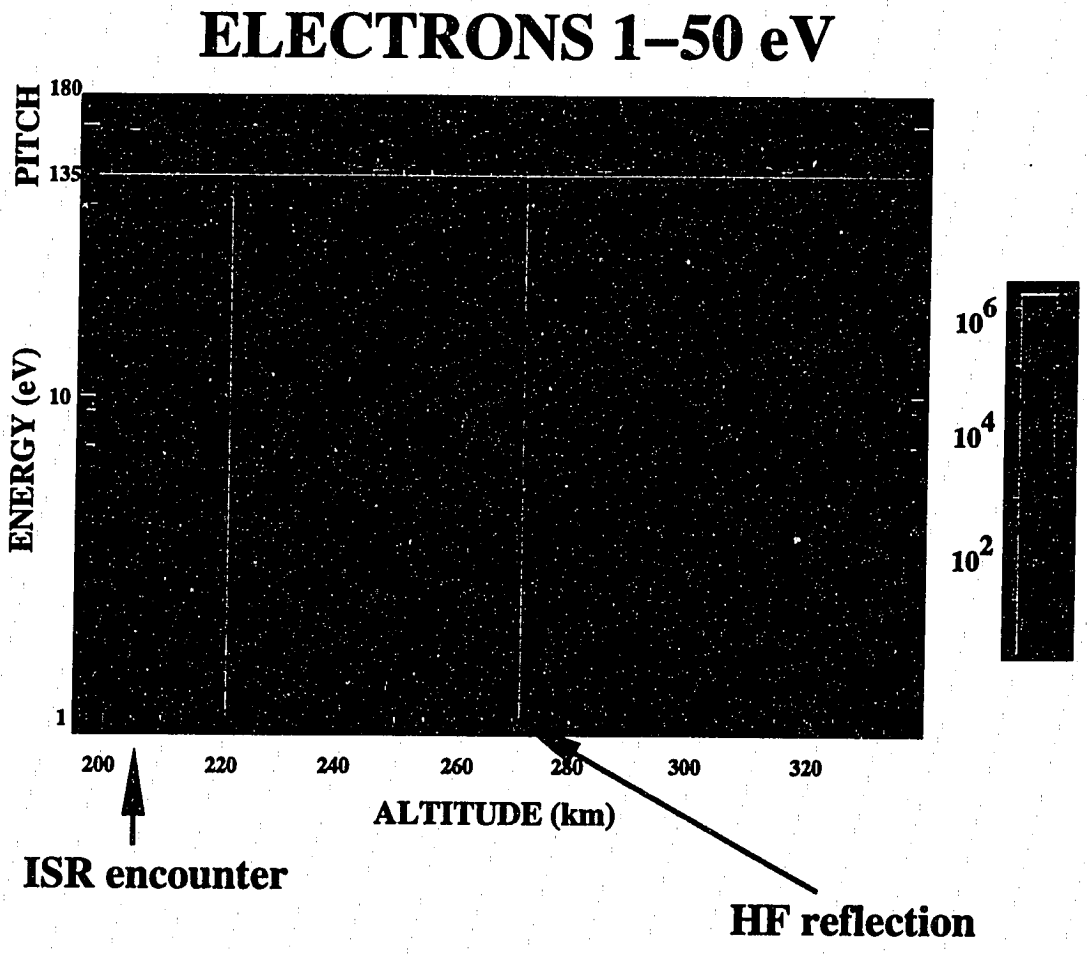

Figure 4-2: *Electron survey spectrogram.*

thermal energy. For the F layer equatorial ionosphere, then, we expect a peak at ~ 0.2 eV. The thermal ions in figure 4-1 appear at a much higher energy which must correspond to the charging of the spacecraft to a potential of 1-5 volts below that of the surrounding plasma. The value of the spacecraft potential indicates a balance between thermal electron and ion fluxes: a zero-current condition at the spacecraft. The charging of our spacecraft will be used to diagnose the superthermal electron flux from the heater, by a method described in section 5.3. Our rocket flight occurred entirely in darkness, so there is no photoelectron flux to effect the spacecraft charging.

Spin Modulation and Wake Effects

Upon closer examination it can be seen that the red thermal stripe varies in intensity and width at a rate corresponding to the spacecraft spin period of 1.6 seconds. This spin modulation is of course not natural, nor is it immediately obvious why it should be present. The field of view of the ion Bagel was nominally aligned with the rocket spin axis, and its response function is quite close to axisymmetric.

One plausible explanation for the spin modulation is based on the fact that the Bagel looked always into the spacecraft wake. Figure 4-3 illustrates the idea. The spacecraft spin axis $\vec{s}$ and the velocity vector $\vec{V}_R$ are generally not collinear. This means that as the spacecraft rotates, the Bagel is moved back and forth across the wake. In position (A), the Bagel is looking primarily at undisturbed plasma, while in position (B), most of the ions the Bagel will count are drawn from the disturbed region.

The data from a thermal ion detector on board a spacecraft are strongly influenced by spacecraft motion if the spacecraft speed is comparable to the ion thermal speed. In this case, with $T_i \sim 0.1$ eV, a thermal O^+ ion has a velocity of 750 m/s, compared to the

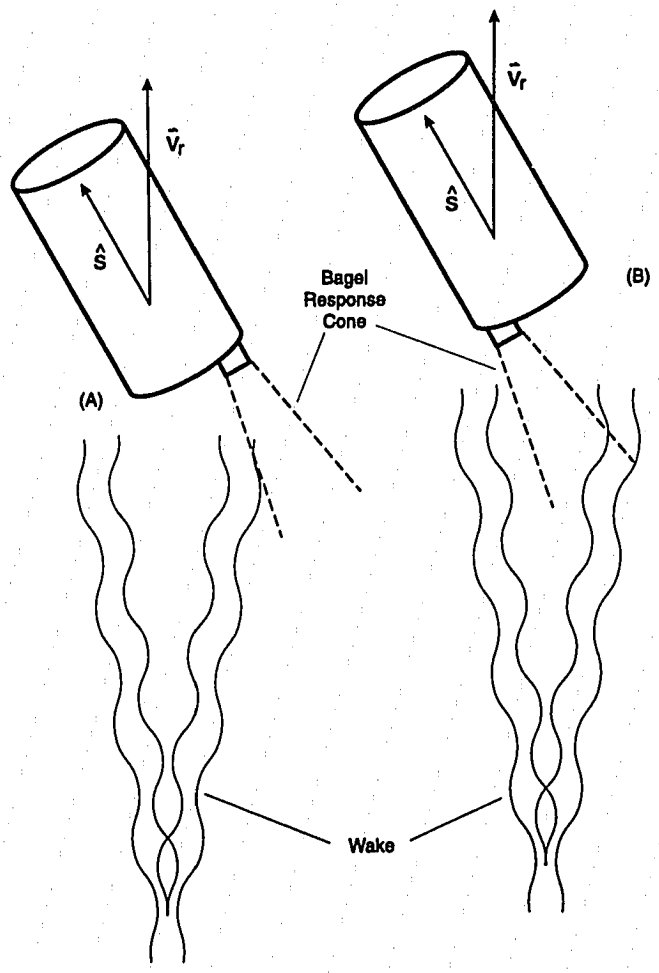

Figure 4-3: *Possible explanation for spin modulation in ion Bagel data.*

spacecraft velocity of about 1 km/s, so wake effects are likely to be present.

For the ion Bagel on board Soliton, wake effects are the cause of the easily visible spin modulations in thermal fluxes. Spin modulation from the ion Bagel is at first surprising, since the Bagel's look direction is aligned with the payload spin axis. The zeroth order wake effect is simply that the region immediately behind the spacecraft is not accessible to particles with speeds lower than the spacecraft speed. So, if a spacecraft is moving faster than a thermal ion, there will be a region behind the spacecraft where thermal ions are rare, and this region, with its anomalously high proportion of *superthermal* ions, will have an elevated ion temperature. The ion Bagel sampled from this region throughout the flight, therefore its output was always influenced by the shape, size and precise location of the wake. As the spacecraft rotated, the fraction of ions reaching the detector after crossing the wake region changed (see figure 4-3), resulting in spin modulations in ion fluxes, densities and temperatures.

Model Detector Results

The model for detector response (see section 5.2) was used to estimate T_i in the HF modified region. The result, displayed in figure 5-7 , shows a very high T_i of 0.3 to 0.4 eV, at the time of closest magnetic approach to the HF interaction region (145 seconds). This is an interesting result, but not a conclusive one. The wake effects just discussed do not allow for an unambiguous interpretation of the ion temperature.

4.1.2 Data from the Electron Detectors

One of the more surprising (and discouraging) aspects of the Soliton data is the almost complete absence of counts from either of the electron detectors. The explanation for this

is to be found in the unexpectedly high level of spacecraft charging which occurred on this flight. The spacecraft potential was always a few volts negative, tending to attract ions and repel electrons. In addition, charging produces an angular effect which tends to steer off-axis ions into the response cone, while electrons are deflected out. This angular effect amounts to a change in the detector's sensitivity; for a narrow field detector like the Bagel, it can change by a factor of 100 or more.

Several electron channels "saturated" at the moment of closest approach to the ISR beam. I am uncertain how to interpret this, except to note that not all pitch-angle bins on the SESA behaved the same way; in particular, the field-aligned bin did nothing. On the other hand, all four channels on the electron Bagel saw the "saturation", as did the two channels on either side of the SESA's field-aligned bin. Note that if this signal had occurred at some other time in the flight, it would have been disregarded as a "telemetry dropout", "power glitch", "ACS event", or other non-specific "hiccup".

An additional use of the model detector (see section 5.2) was to determine the significance, if any, of the absent electrons. It showed that the absence of electrons is not a true null result; conditions on the spacecraft were such that our detectors were simply not capable of seeing the expected superthermal electrons.

4.2 Data from the Cornell Wave Instruments

The wave data in this thesis consist almost exclusively of various incarnations of the data from the d.c. electric field probe (V1-2) and fixed-bias Langmuir probe (CAV5). Figure 5-10 shows the relative placement of these two instruments.

4.2.1 Data from the Electric Field Instrument

The convection electric field was obtained onboard Soliton by measuring the potential difference between a pair of 3.0 inch diameter conducting spheres separated by a 3-meter boom (see figure 5-10). Section 5.7 describes the method in detail. The raw data are shown in figure 4-4. The data from 370-400 seconds are particularly important, since they show that the spacecraft-frame electric field away from the heated volume is equal to $\vec{\mathbf{V}}_R \times \vec{\mathbf{B}}_0$, where $\vec{\mathbf{V}}_R$ is the spacecraft velocity and $\vec{\mathbf{B}}_0$ is the geomagnetic field, i.e., that the earth-frame convective drift, in a region away from the heated volume, is too small to measure. Note how the data from 140-310 seconds show that the envelope of the spin-modulated V1-2 signal is at times *larger* than the total magnitude of $\vec{\mathbf{V}}_R \times \vec{\mathbf{B}}_0$. This overshoot is the unambiguous signature of a non-zero earth-frame electric field $\vec{\mathbf{E}}_{earth}$, and the size of the overshoot represents a minimum for the magnitude of $\vec{\mathbf{E}}_{earth}$. Note that the overshoot tends to become smaller after 170 seconds, as the spacecraft moves away from the heater beam.

Figure 4-5 shows a short section of V1-2 data, along with the projection of $\vec{\mathbf{V}}_R \times \vec{\mathbf{B}}_0$ onto the V1-2 boom direction. The similarity of the two traces shows, in more detail than figure 4-4, that the V1-2 signal is due primarily to spacecraft motion. It would have been preferable to make figure 4-5 using data from some interval *after* 370 seconds. Unfortunately, no attitude solution is available after 240 seconds (see section 5.6), so there is no way, at those times, to project $\vec{\mathbf{V}}_R \times \vec{\mathbf{B}}_0$ onto the spin plane.

4.2.2 Data from the Density Probe

The density probe (CAV5), although held at a fixed-bias throughout the flight, was in effect operated in a few different modes because of the variations in the spacecraft potential. The intent of CAV5 was to measure the electron density by operating in the electron-saturation

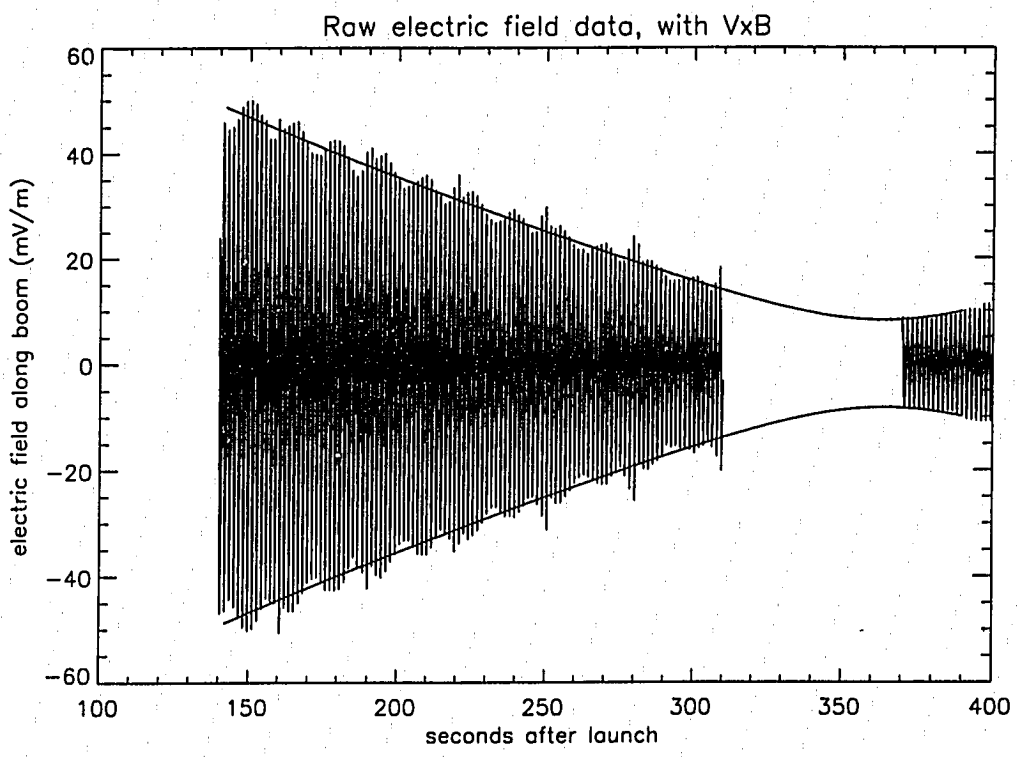

Figure 4-4: *Overview of the output signal from the V1-2 instrument.* Before 310 seconds, the spacecraft coning motion is reflected in the data. After 370 seconds, the spacecraft is aligned to $\vec{B}_0$, and no longer cones. The data between 310 and 370 seconds (and before 140 seconds) are corrupted by the attitude control system.

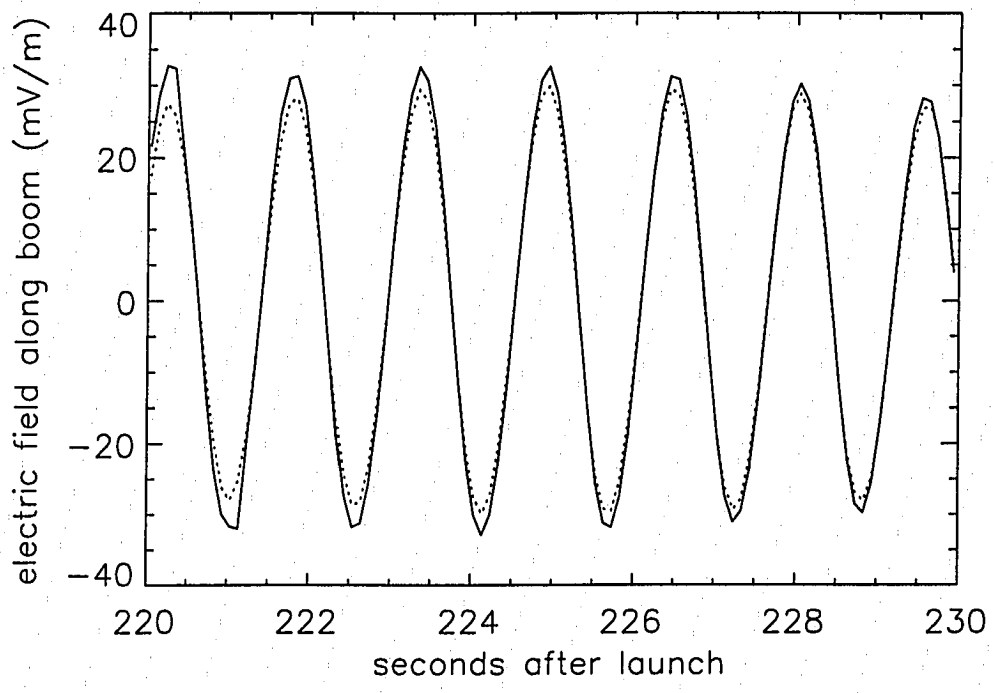

Figure 4-5: *Detail of the output signal from the V1-2 instrument.* In this short section of data, the motional e.m.f. $(\vec{V}_R \times \vec{B}_0) \cdot \vec{l}$ has been superimposed (dotted line) on the instrument's output. This shows that most of the V1-2 signal is due to motional emf, and also gives plausibility to the attitude solution.

regime, that is, by maintaining a positive probe potential with respect to the surrounding plasma. This is in fact realized after 145 seconds, when the spacecraft potential drops abruptly below 3.0 volts. Prior to 145 seconds, the probe is probably operating in the ion-linear regime, and the fluctuations are too small to be detected by CAV5; only the 12-bit CAV5' is capable of detecting fluctuations at these times. It is quite fortunate, from the point of view of this thesis, that a 12-bit sampler was applied to the density probe. Without it, we could not have detected density fluctuations near the ISR beam, and the data near the ISR would be a great deal more dubious.

4.3 Encounter with the Arecibo HF heater

Soliton did in fact barely accomplish its mission to explore the HF-heated ionosphere. Although we are unable to investigate the 0.1 meter, 100 μs scale processes to which the ideas of the Zakharov model (see chapter 2) are tailored, we nonetheless give new insight into processes occurring at the 10-meter scale and larger.

4.3.1 Reflection of HF power

Although Soliton did not fly through the center of the heater beam, it passed closely enough (within several kilometers of the -3 dB contour) to detect significant HF power with an onboard search coil and logarithmic receiver. Figure 4-6 shows the relative magnitude of the HF signal at the spacecraft as a function of time. The main feature of figure 4-6 is the abrupt disappearance of signal after 168 seconds, when the spacecraft passes the HF reflection height and exits the heater beam.

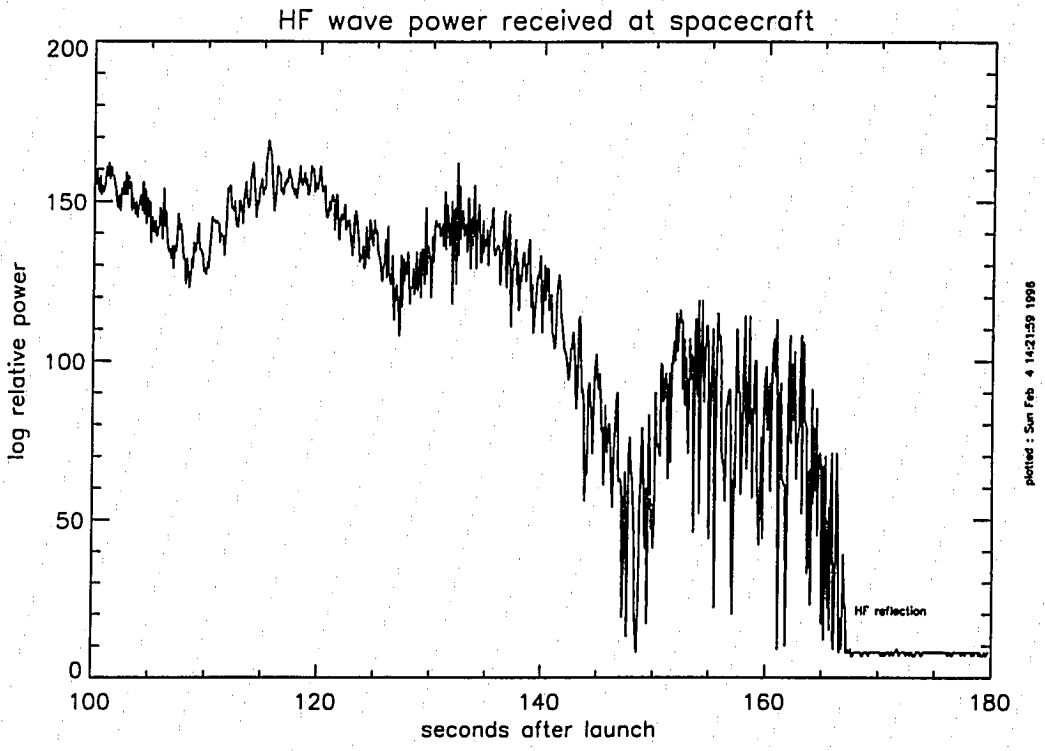

Figure 4-6: *HF wave power received at the spacecraft.*

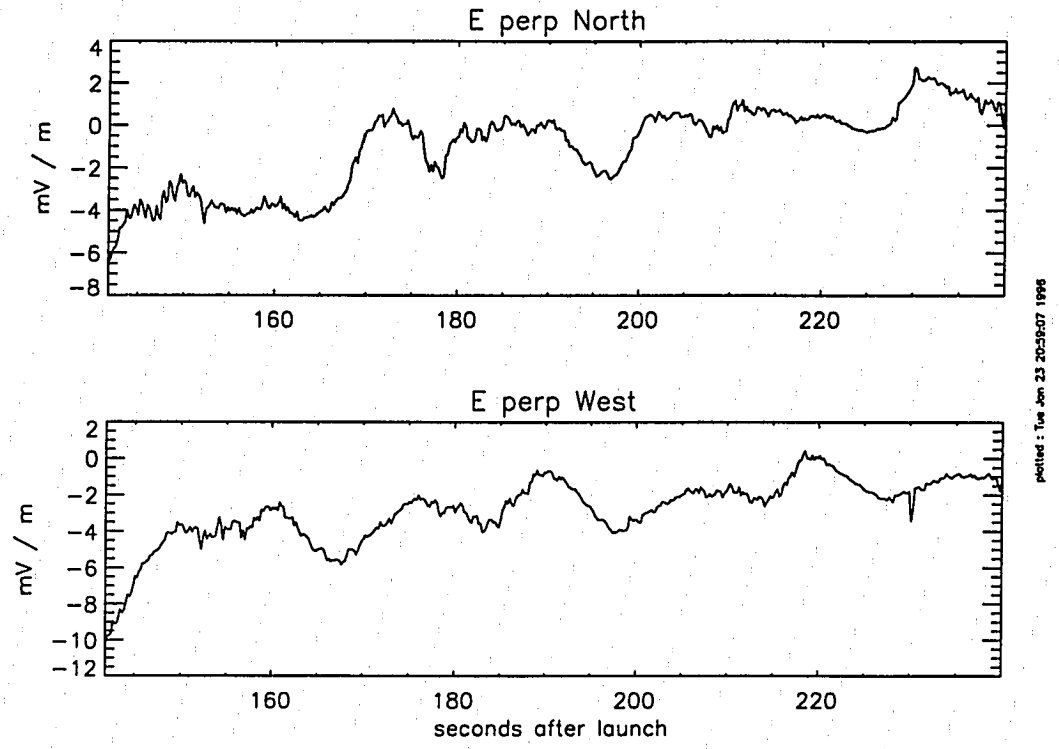

Figure 4-7: *Components of the Earth-frame convection electric field.* The heater beam is exited at 168 seconds after launch. The most interesting feature is the abrupt disappearance of the southward component of $\vec{\mathbf{E}}$ at this time.

4.3.2 Convection Within and Near the Heated Volume

Near the height of HF reflection, an examination of the electric field and drift reveals a shear in the horizontal drift. Below the height of HF reflection, the electric field has a substantial southward component which disappears abruptly when the spacecraft leaves the heater beam. Figure 4-7 shows the components of the perpendicular electric field. Figures 4-8 and 4-9 show the components of the perpendicular drift. The data are somewhat contaminated by the spinning and coning motions of the spacecraft; nevertheless, the abrupt decrease in drift speed, and shift in drift direction, as the spacecraft leaves the heated volume, point to a heater-driven convection pattern.

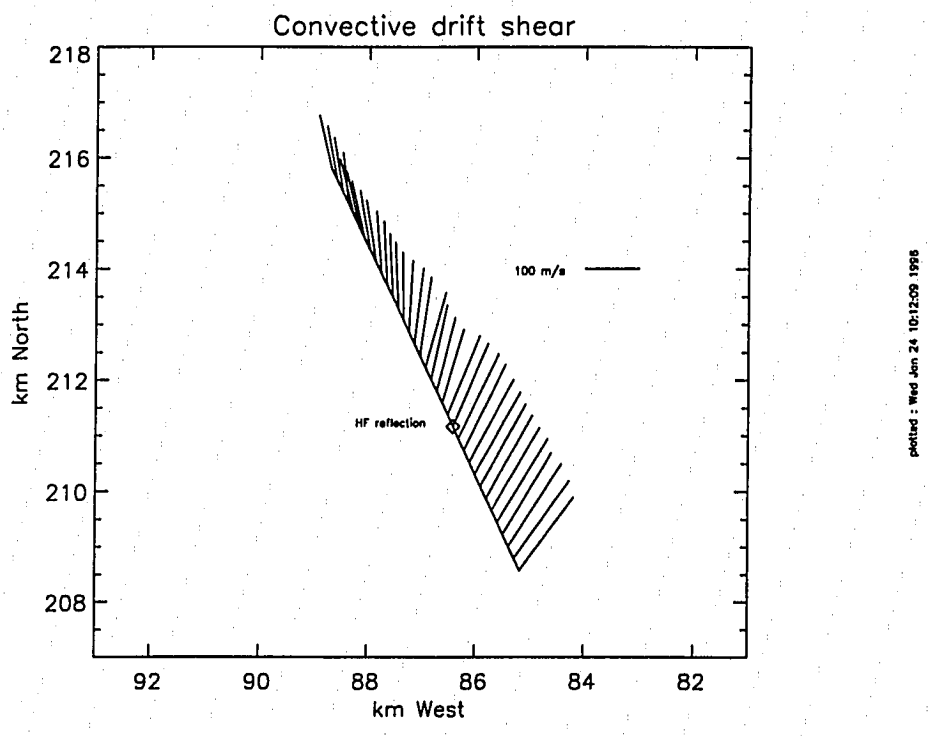

Figure 4-8: *Shear in the* $\vec{E} \times \vec{B}_0$ *drift deduced from the V1-2 data.* The magnetic field is perpendicular to the paper, pointing in. Data from 165-173 s are used.

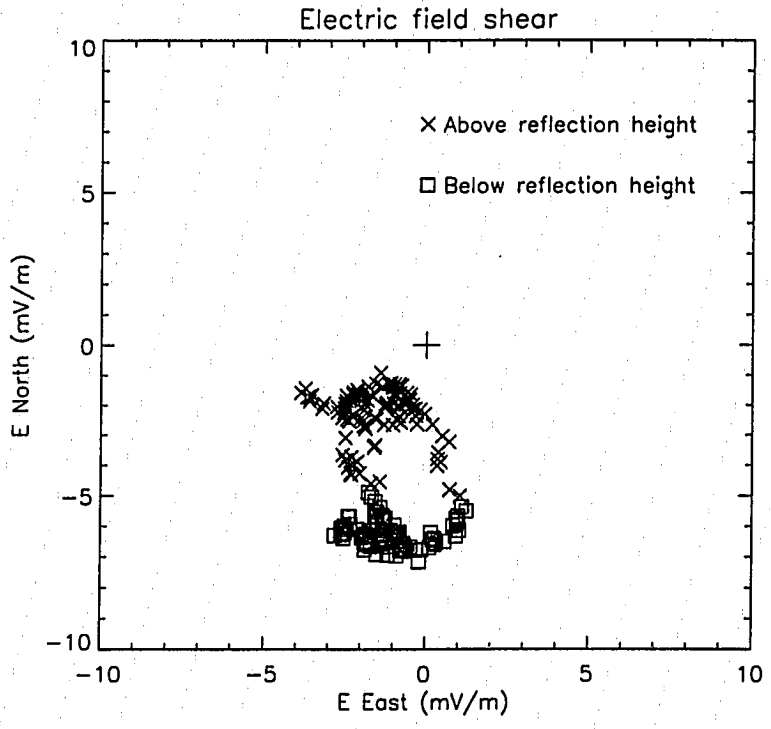

Figure 4-9: *The tip of the electric field vector, near the HF reflection altitude.* The squares mark measurements within the heater beam, while 'x' is used for above and to the west. Data from 150-190 s is used, and the heater beam exit is taken to be at 168 s.

It is possible that the shear observed on the electric field instrument is in fact due to sheath rectification of the HF heater wave[Boehm et al., 1994]. However, the false potentials produced on a floating probe by this mechanism would show a gradient corresponding to the gradient of wave power in the HF beam. Therefore, the false component of electric field produced by sheath rectification should point east or west, along the HF wave power gradient, whereas as we observe a southward component within the heated volume, *perpendicular* to the HF wave power gradient.

This shear in the convection electric field can be related to a heater-driven current system. The Pedersen current is obtained by taking the divergence of the perpendicular electric field, while any parallel current can be inferred by requiring the $\nabla \cdot \vec{J} = 0$ [Kelley, 1990]. To evaluate the divergence of $\vec{E}$, however, we must make some assumptions about its three dimensional structure.

Because of the extremely high conductivity parallel to $\vec{B}_0$, the convection electric field, measured at a single point, can be mapped along $\vec{B}_0$, using the field line as an equipotential. Since $\vec{B}_0$ is uniform over our (small) region of interest, we can assume that the derivatives of $\vec{E}$ along $\vec{B}_0$ are zero. Furthermore, since we interpret the electric field shear to be something connected with exiting the heater beam, we may plausibly assume that the only non-zero derivatives are those along the direction extending outwards, normal to the heater beam boundary.

Such a direction, however, is not simple to determine. Even the free-space radiation pattern of the heater beam is quite complex in its finer details, and it is strongly modified by the "patchy" nature of the heated ionosphere [Duncan et al., 1988]. In other words, while the large-scale heater beam can be drawn as it is in figure 3-1, it is not possible to determine the precise orientation of the heater beam boundary at the point where our single

spacecraft makes its exit from the heated volume. Even without these complications, it is somewhat unclear whether the abrupt decrease in received heater power seen in figure 4-6 is due to passing through the reflection height, out of the beam pattern to the West, or both. Furthermore, it seems likely that we exited the beam from a secondary side-lobe.

The electric field changes by 4 mV/m in the Northward direction, and the spacecraft travels 4.7 km Northward during this change. We can therefore place a maximum on $\nabla\cdot\vec{\mathbf{E}}$, namely 0.85 mV/m/km. Note that $\nabla\cdot\vec{\mathbf{E}}$ is in units of $\mu\mathrm{V/m^2}$. If we take Σ_P, the height-integrated Pedersen conductivity, to be a very approximate 1 mho[Kelley, 1990], we get a maximum parallel current of around $J_\parallel = 1\mu\mathrm{A/m^2}$. This is quite a large value, and it is important to remember that our measurements are also perfectly consistent with $\nabla\cdot\vec{\mathbf{E}} = 0$. However, it is interesting to speculate about a heater-driven current system, and our data indicate an upper limit on the parallel current available to close any heater-driven perpendicular currents.

In the next few sections, I will present a mechanism which *must* produce perpendicular currents at the height of HF reflection. Then, we can see whether or not the parallel current estimated above might in fact be the closure of these perpendicular currents.

Currents Driven by the Ponderomotive Force

An interesting and very intuitively appealing mechanism for coupling high frequency drivers to low frequency responses is the ponderomotive force [Chen, 1984]. This force is quite robust; it is present whenever the power of a high frequency wave has a spatial gradient. In many physical situations, the magnitude of this force is not terribly large. On the other hand, it has been considered as a candidate confinement mechanism for fusion plasmas [Vedenov, 1958]. It is physically analogous to the radiation pressure force, or to the force

acting upon sand diffusing to the nodal lines of a vibrating drumhead.

The ponderomotive force, acting on a single particle of species s can be written explicitly as

$$\vec{\mathbf{f}}_{NL} = -\frac{1}{4}\epsilon_0 \frac{\omega_{ps}^2}{n_0 \omega^2} \nabla \left\langle {E_{HF}}^2 \right\rangle,$$

where E_{HF} is the peak wave electric field amplitude. The concept of a ponderomotive force makes good physical sense whenever the distance traveled by a thermal particle during one period of the wave can be neglected in comparison to the wavelength of the driving wave. The ponderomotive force is typically invoked for driving frequencies near or above the electron plasma frequency; the validity condition therefore is that the driver wavelength be large compared to the Debye length. More generally and simply still, it can be said that the ponderomotive concept can be applied to a wave-particle interaction if the particle velocity is much smaller than the wave phase velocity.

Furthermore, in a background magnetic field $\vec{\mathbf{B}}_0$, if the driver frequency is much greater than the relevant cyclotron frequency, then the ponderomotive force, like any other low-frequency force in a plasma, has an associated drift[Kopecky, 1968], namely

$$\vec{\mathbf{v}}_{NL} = \frac{\vec{\mathbf{f}}_{NL} \times \vec{\mathbf{B}}_0}{q_s B_0^2}.$$

Figures 4-10, 4-11, and 4-12 show the result of a numerical calculation which demonstrates the ponderomotive drift. Note that $\vec{\mathbf{f}}_{NL}$ is larger for electrons than ions by $\frac{m_i}{m_e}$, and that the associated drifts are in opposite directions for electrons and positive ions (see figure 4-10). There is, therefore, a current driven by the ponderomotive force, given by

$$\vec{\mathbf{J}}_{NL} = \epsilon_0 \left(\frac{\omega_{ps}}{\omega}\right)^2 \frac{(\nabla E^2) \times \vec{\mathbf{B}}_0}{B_0^2},$$

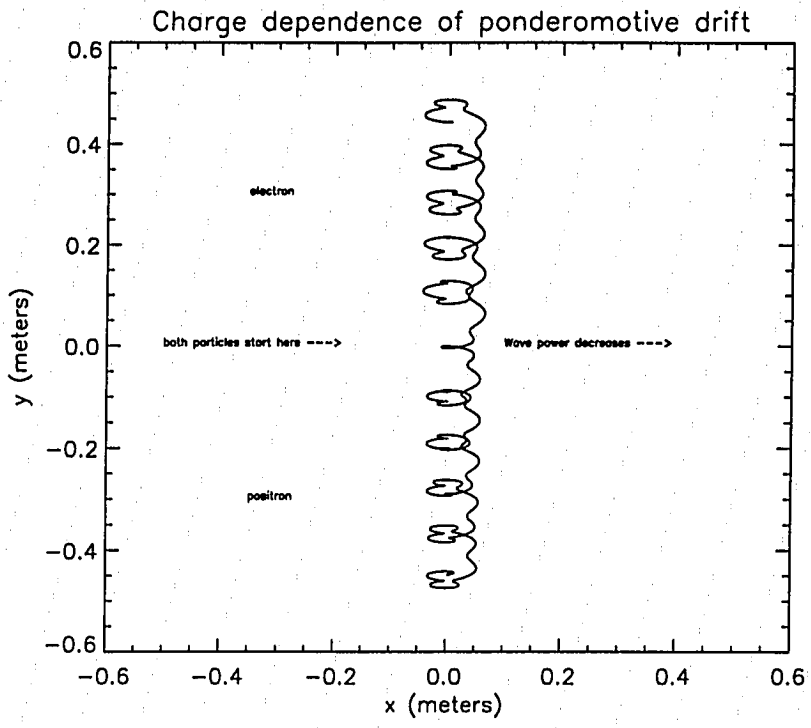

Figure 4-10: *Ponderomotive drift for an electron and a positron.* The parameters here are the same as for 4-12, except the field amplitude has been exaggerated to 100 V/m, to show the ponderomotive effect more clearly. The magnetic field points out of the paper.

or

$$J_{NL} = \epsilon_0 \frac{\omega_{ps}^2}{\omega^2} \frac{E^2}{LB_0}. \tag{4.1}$$

Note that the E in these equations includes the incident wave, a reflected wave, and any induced Langmuir waves. E is the self-consistent wave power profile, whose characteristics are known from radar and in situ measurements [Kelley et al., 1995][Sulzer, 1994a]. The exact dynamics of the reflection, mode conversion to Langmuir waves, dissipation and enhancement of the incident heater wave is unimaginably complex, but once the wave power profile has been measured, then the associated ponderomotive currents are straightforward to compute. While ponderomotive forces, drifts, and currents may in many situations be

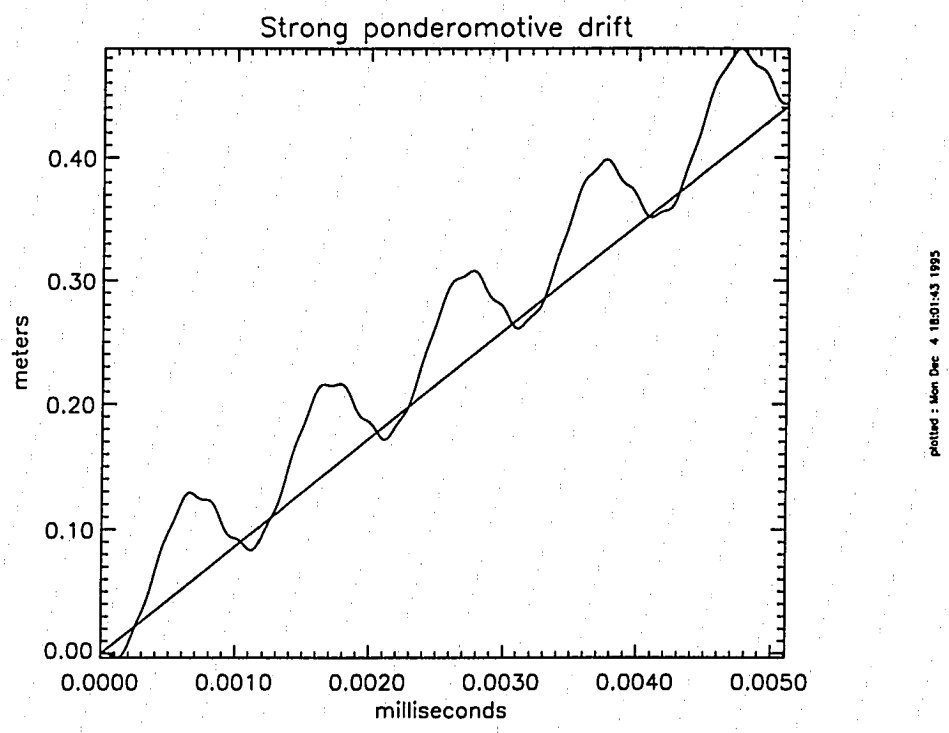

Figure 4-11: *Ponderomotive drift for an electron, with the exaggerated pump of figure 4-10.* The line shows the value of $(\vec{f}_{NL} \times \vec{B}_0/B_0^2)t$; in this case the drift is 86 km/s. Note that even with the extreme distortion of the gyro orbit shown in figure 4-10, the drift motion remains.

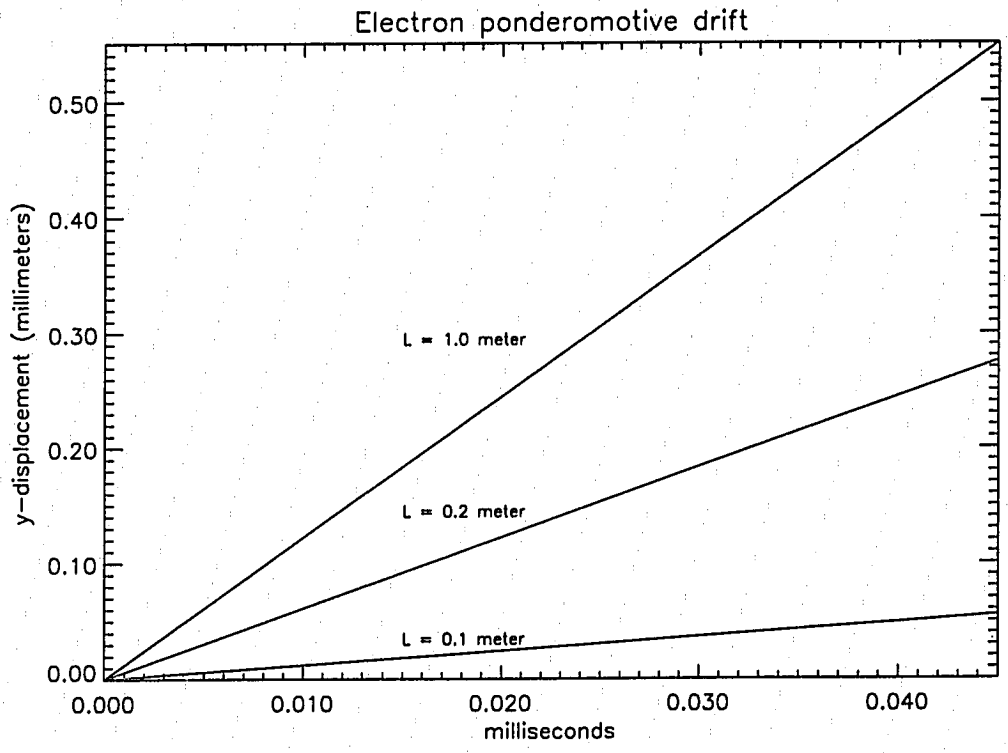

Figure 4-12: *The ponderomotive drift for an electron, at various wave power gradient length scales L.* The pump frequency is 5.1 MHz, $|\vec{B}_0|$ is 0.35 gauss, so ω/ω_{ce} is ~ 5. The full Lorentz force equation was integrated, then the gyro motion was averaged out to produce the guiding center drift shown here. This is exactly like figure 4-11, but with an electric field strength of 1 V/m, appropriate to the HF heater.

quite small, they are *not* first-order effects associated only with incremental departures from an artificially-imposed quiescent state. They are in fact an unavoidable consequence of the dynamics of wave-plasma interactions. There is nowhere to hide from the ponderomotive force.

It is fairly easy to estimate the magnitude of the ponderomotive current, given the fairly well-known properties of the wave power gradients associated with the heater. The heater has an equivalent spherically radiated power of 50 MW in its tilted configuration, which gives an electric field approximately of 1 V/m in the standing wave pattern at the reflection height. The Airy standing wave pattern has been observed frequently at Arecibo, and is typically 900 m thick with 4 or 5 wave amplitude maxima, the largest of these approaching 1 V/m [Sulzer, 1994b]. So the gradient length scale in equation 4.1 can be taken to be 100 meters, with an E_{HF} of 1 V/m. This results in $J_{NL} \sim 0.08\mu$ A/m^2, flowing west/east for wave power increasing/decreasing with altitude. The maximum parallel current density of 1 μA/m^2 is more than sufficient to close such a current at the edge of the beam.

By presenting this estimate, I am merely attempting to show that the ponderomotive force could plausibly produce measurable convection around the heated volume. The main difficulty with applying these ideas to the reflection layer in this experiment is that the electron gyro frequency and the heater frequency are on the same order, and so the motion of a single electron is perhaps not well described by the simple $\vec{\mathbf{f}}_{NL} \times \vec{\mathbf{B}}_0$ model. The numerical calculations presented in figures 4-10, 4-11, and 4-12 are somewhat reassuring in this regard.

4.3.3 Superthermal Ion Plume

Inspection of figure 4-1 reveals what appears to be a population of superthermal ions measured above the reflection height and to the west of the heater beam. Much of the original effort to compute an attitude solution and a convection electric field was directed toward strengthening this result. Could these ions have been accelerated to energies of 50 eV and higher by the heater, and be drifting west to meet the spacecraft? I will refer to this interpretation as the "ion plume".

More careful inspection of figure 4-1 shows some modulation of the plume ions at the spacecraft spin and coning rates. While this modulation probably eliminates "dark counts" as the source of the plume, its directionality is found, in a detailed calculation, to correlate with the spacecraft velocity vector, i.e. it is a wake effect (see section 4.1.1). Nonetheless, the plume can be said to be caused by particles entering the detector, on these grounds.

However, it is entirely possible that the "plume ions" are actually generated by secondary scattering of energetic electrons within the detector. This sort of contamination is sometimes observed by ion detectors passing over an auroral arc [Arnoldy, 1994]. If this is the case, it would be quite interesting, since the spacecraft is traveling ever farther from magnetic connection to the heater at the times where the plume is observed. There is unfortunately no way to estimate the total flux of such energetic electrons. It is presumably somewhat less than the energetic electron flux seen within the heater beam, since there appears to be no additional spacecraft charging accompanying the plume, as there is within the heater beam (see section 4.3.4) .

If the ion plume can be taken at face value, as a drifting, heater-energized population of superthermal ions, then it is energetically important. If the heater is taken to have an ERP of 50 MW, then its Poynting vector has a magnitude of 0.05 mW/m^2, at the

reflection height. The ion plume, being a directed energy flux, can reasonably be compared to the heater Poynting vector. Using the methods of section 5.1, we obtain the estimate 0.007 mW/m^2. If this number seems high, consider the laboratory results of *Wong and Stenzel*, who performed a microwave heating experiment near the plasma frequency. They found an equipartition of the dissipated microwave energy, between superthermal ions and electrons[Wong and Stenzel, 1975].

4.3.4 Superthermal Electrons

Figure 4-1 shows a peak in the spacecraft potential at an altitude of 237 km (145 seconds after launch). This is the time when the spacecraft is closest to magnetic connection with the center of the HF beam [Bernhardt et al., 1995]. Figure 4-13 shows our estimate of the superthermal electron flux below the heater reflection height, obtained from the spacecraft potential by the method described in section 5.3. There are difficulties with this method which cast some doubt on our absolute flux estimate (see section 5.3), but the variability in spacecraft charging presumably does map to variability in the superthermal electron flux. Such variability is absent outside the heater beam.

From figure 4-13 we estimate the peak in total collected electron flux to be 3-4 $\times$ 10^{14}/m^2-s. *Rose et al.* measured *in situ* the flux of electrons with energies of 9 eV or higher to be 10^{13} electrons/m^2-s, near the reflection height of the Tromsø heater, which supplied 60 MW ERP at 5.6 MHz. They used a retarding potential analyzer [Rose et al., 1985]. Groves estimated this flux at Arecibo to be 2-4 $\times$ 10^{11}/m^2-s, with a minimum energy of 12-14 eV, using an ISR technique[Groves, 1995].

Our estimate of total collected electron flux is rather higher than these estimates of the superthermal electron tail flux. Note that our low energy cutoff for "superthermal" is

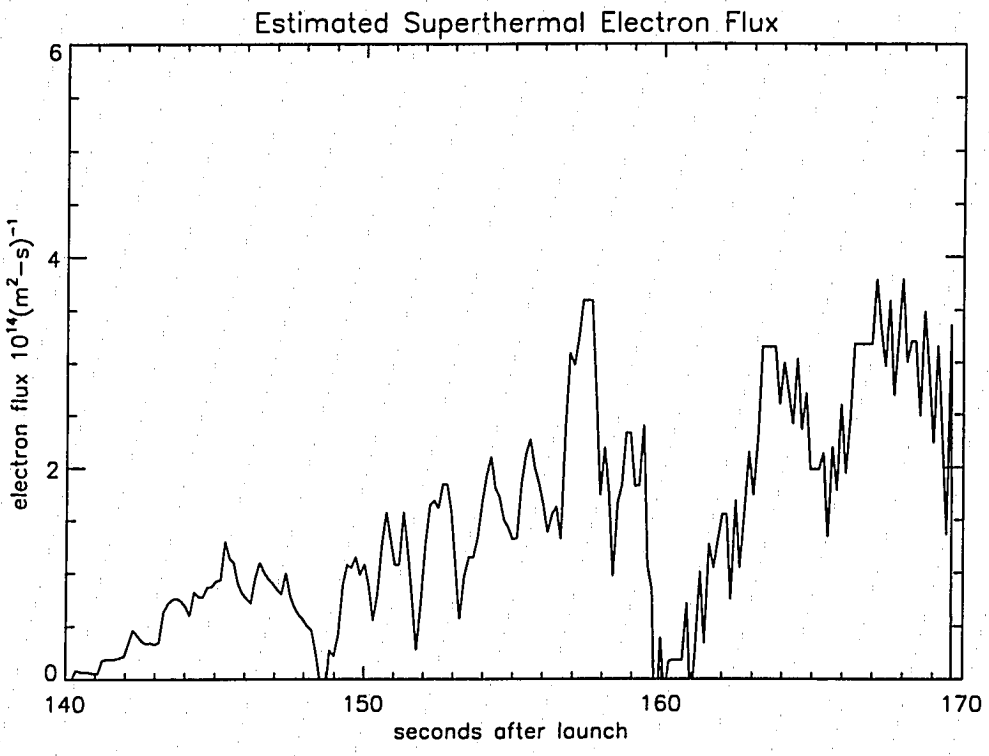

Figure 4-13: *The superthermal electron flux inferred from indirect measurement of the spacecraft potential.*

the lowest of these three estimates, being in fact the spacecraft potential itself (2-6 eV). If we assume a power law spectrum for the energetic electron tail, with an index α, then one finds the estimate of total superthermal flux depends on the choice of cutoff energy, going as $(E_1/E_2)^{\alpha+1}$, where E_1 and E_2 are the two different choices for the minimum "superthermal" energy. A spectral index of 4 can account for the difference between our estimate and that of *Rose et al.*, the point being primarily that this sort of comparison is somewhat shaky, due to discrepancies in what is meant by "superthermal electron flux"! Our method contains no estimate of the core electron temperature, but presumably that part of the thermal distribution which is sufficiently energetic to reach the charged spacecraft is utterly negligible. If the electrons charging the spacecraft were in fact representatives of a heated thermal population, the corresponding electron temperature would be on the order of 1.0 eV, which is 10 times larger than typically observed by ISR in an HF heated ionosphere [Djuth et al., 1987b].

A perfectly reasonable question now arises: if we estimate a high flux of superthermal electrons collected by the spacecraft, why are we unable to detect these electrons with our sophisticated superthermal electron detectors? The answer has basically to do with look directions. For the electron Bagel, things are simple. It is mounted on the end of the payload near the ion Bagel, and never has a chance to look along field lines *toward* the heater beam, only away. For the SESA, the situation is somewhat more complicated, but a detailed calculation using the attitude solution and the magnetometer data shows that the response function of the SESA rarely lies close enough to $\vec{\mathbf{B}}_0$ to see a field-aligned flux of electrons. Furthermore, as indicated in figure 4-14, the SESA apertures barely protrude beyond the spacecraft potential structure, making it difficult even for sufficiently energetic electrons to reach the SESA without being steered away by the sheath electric fields.

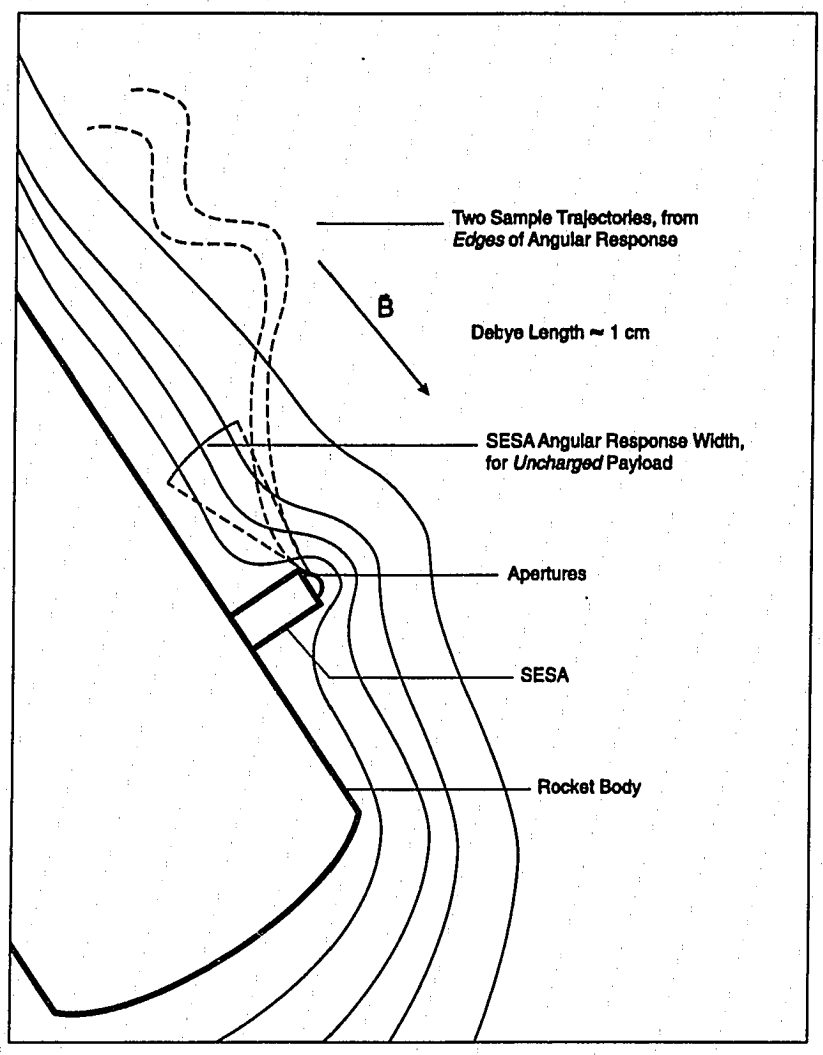

Figure 4-14: *Artist's conception of SESA with respect to spacecraft potential structure.* The spacecraft spin axis is within a few degrees of $\vec{B}_0$ in this drawing. The SESA looks in the plane perpendicular to the direction at which it protrudes from the payload. This plane contains the spin axis. The angular width, about this plane, of the SESA's response function is shown, as are two extreme trajectories which enter the SESA at either edge. Note that the trajectories are nearly parallel outside the sheath.

4.3.5 HF-induced Filaments

A common radar observation during HF heating is heater enhanced field-aligned structure (FAI) at short (0.5 to 5 m) wavelengths [Coster et al., 1985],[Das and Fejer, 1979], [Minkoff, 1974],[Noble and Djuth, 1990]. Soliton was able to reveal, for the first time, the detailed nature of the structures which produce these echoes. They turn out to be field-aligned density depletions, or filaments, which appear to exist on rather long ($\gg 1s$) time scales, and are approximately 10 meters in diameter, separated by 15 meters on average. The filaments are observed within 3 km altitude of the HF reflection height, both above and below, and contain plasma which is $\sim$ 100 K hotter than their surroundings.

The filaments first made themselves apparent as three groups of 10 millisecond-scale decreases in current collected by a Langmuir probe [Kelley et al., 1995]. They represent depletions in the background plasma density of at least 5-10%, since the hotter plasma inside the filaments tends to *increase* the probe current. Furthermore, difficulties associated with sheath rectification [Boehm et al., 1994] can be eliminated, because the third filament "bunch" is observed *above* the HF reflection height, where there is no significant HF wave power.

Filament "Electric Fields"

The decreases in probe current are accompanied by bipolar pulses on the electric field instrument, called V1-2. These bipolar pulses are roughly proportional to the time derivative of the current dips, and are precisely what would be expected from an instrument measuring a gradient in plasma density, potential, or temperature across a steady state density depletion. Figure 4-15 shows the density and field probe data for a typical filament.

By using the antenna directionality (from the attitude solution, see section 5.6), together

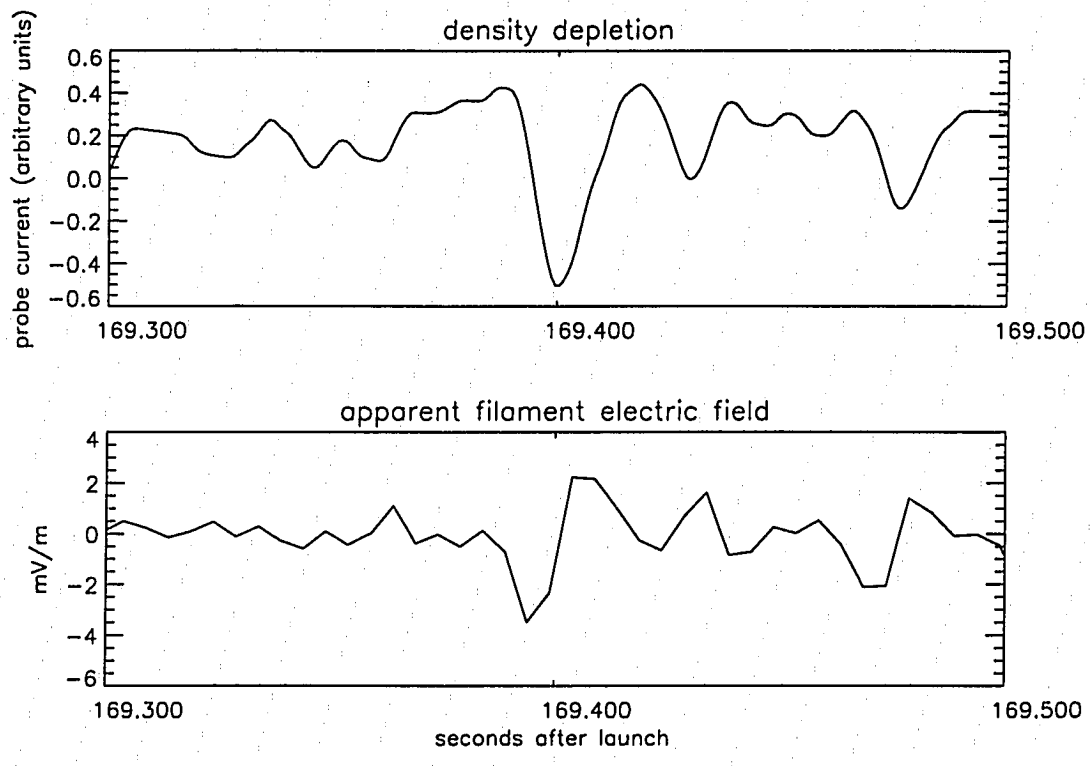

Figure 4-15: ***A typical HF induced filament.*** **There is an abrupt decrease in probe current, accompanied by a bipolar pulse on the electric field instrument.**

with the polarity of the bipolar pulses, it is possible to determine that the apparent electric field being detected by the electric field instrument consistently points *into* the density depletions, exactly the opposite of what would be expected from a filament-induced electric field (and, of course, opposite the density gradient).

Estimate of Filament Temperatures

We are measuring, therefore, a minimum value for the temperature gradient, since it is the only vector to which we are sensitive which points *into* the filaments. We don't know what the electric field is, therefore we know only the amount by which the temperature gradient exceeds the electric field. The gradient in floating potential, which is what V1-2 is responding to in this case, is roughly 5 times the gradient in temperature for an $O^+ - e^-$ plasma. Typical V1-2 data in the filaments shows perturbations of 15 mV/m, corresponding then to 3 meV/m of temperature gradient. Since the filaments are typically 10 m in diameter, [Kelley et al., 1995], we estimate a minimum internal temperature enhancement of 10 meV, or about 100 K, appropriate for a condition of zero filament electric field.

It is difficult to imagine a steady state filament electric field of more than 50 mV/m, since at that point the convective drift of electrons, around the filament, would be approximately equal to the ion acoustic speed, and the oscillating two stream instability would quickly disrupt the filament. More restrictive limits can be imagined, but this one suffices to place the maximum conceivable filament temperature enhancement at 400 K.

4.4 Encounter with the Arecibo ISR

Soliton flew within 2.2 km of the Arecibo ISR beam, and was magnetically connected to the beam center at the moment of closest approach. This statement is confirmed by direct

observation of a strong echo in the ISR data, as well as by calculation, from the trajectory and beam pointing data (see section 5.8).

The geometry of the ISR pass is shown in figure 4-16. The circle of radius 2.5 km, centered on the ISR beam, of course intersects the payload trajectory twice. Near the westward intersection, we observe low frequency electrostatic waves followed immediately by a burst of superthermal ions. At the eastward intersection, similar waves were observed, but unfortunately the ion detector was not yet activated.

Before looking at the ISR pass data in detail, it should be mentioned that the onboard attitude control system (ACS) was operating at this time, emitting neutral gas in a programmed attempt to align the payload to $\vec{B}_0$. It is possible that the effects observed near the ISR would not occur without this enhancement of neutral gas near the payload. (There are observations of ISR heating of the D region ionosphere over Arecibo, with the ISR in "long-pulse" mode [Duncan, 1995]). Unfortunately, the ACS is in "hard-fire" mode at this time, meaning that there is no time when all gas valves are closed. There are two valves firing alternately; the one facing *away* from $\vec{B}_0$ is the one firing at any given moment. There appears to be, at least, no relation between the eight valve-switching times near the ISR (two per spin) and the ISR effects.

4.4.1 Events Observed Near the ISR

I will summarize the sequence of events before proceeding to interpret them. The payload flew remarkably near the ISR beam. On approach to the beam, at a distance of 2.5 km from the beam center, ion waves were observed at 24 Hz, for a period of $\sim$ 300 ms(see figure 4-17). The ion detector was not yet activated. The payload reached its point of closest approach, 2.2 km, about 3 seconds later. Saturation of many electron channels was seen at this time.

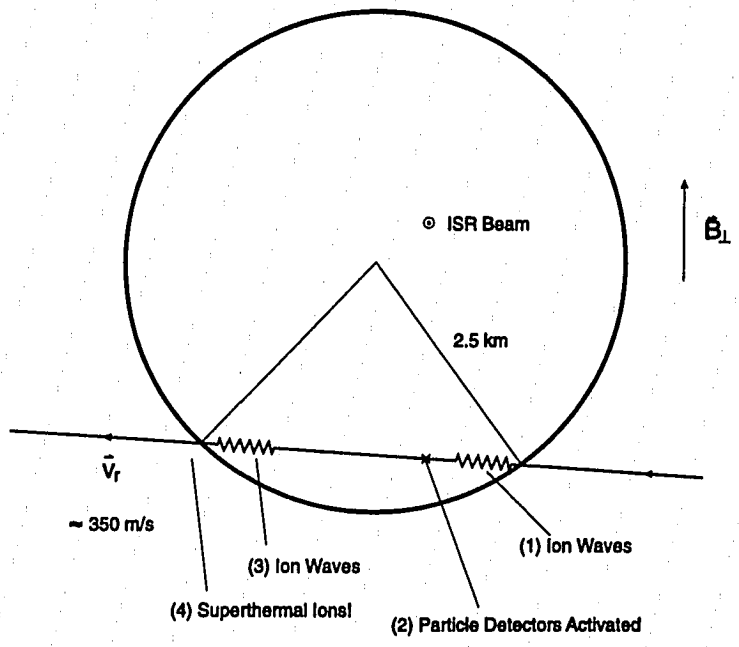

Figure 4-16: *Geometry of the ISR pass.* The rocket traveled from right to left. The ISR beam points out of the paper. The velocity of the payload perpendicular to the ISR was 350 m/s, while the total velocity was 1714 m/s.

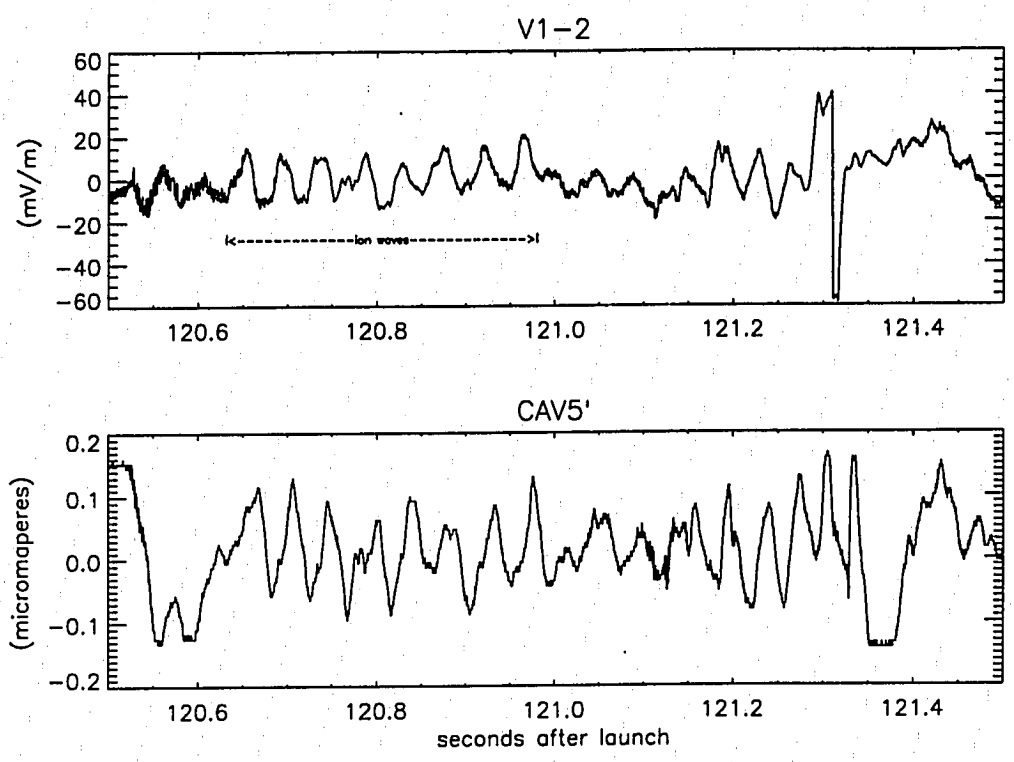

Figure 4-17: *Waveforms for the first ion wave event.*

As the payload receded from the beam, again at a distance of 2.5 km, more ion waves were observed, this time at a frequency of 10 Hz (see figure 4-18). The disappearance of these waves was followed immediately in time by a burst of superthermal ions, with a flat spectrum covering the detector's range from thermals to a maximum sampled energy of 50 eV. The ISR pass covers the altitude range 198-208 km, and the time interval 120-125 seconds after launch.

For the purpose of discussing these events efficiently, I will use the following names: "ISR electrons" for the saturated signal seen by any of the electron detectors near 122 seconds, "ISR ions" for the burst of superthermal ions, and "ion waves" for the low frequency electric field and density perturbations which, it will be argued, energize the superthermal ions.

By calling both sets of wave observations near 2.5 km "ion waves", I have, of course,

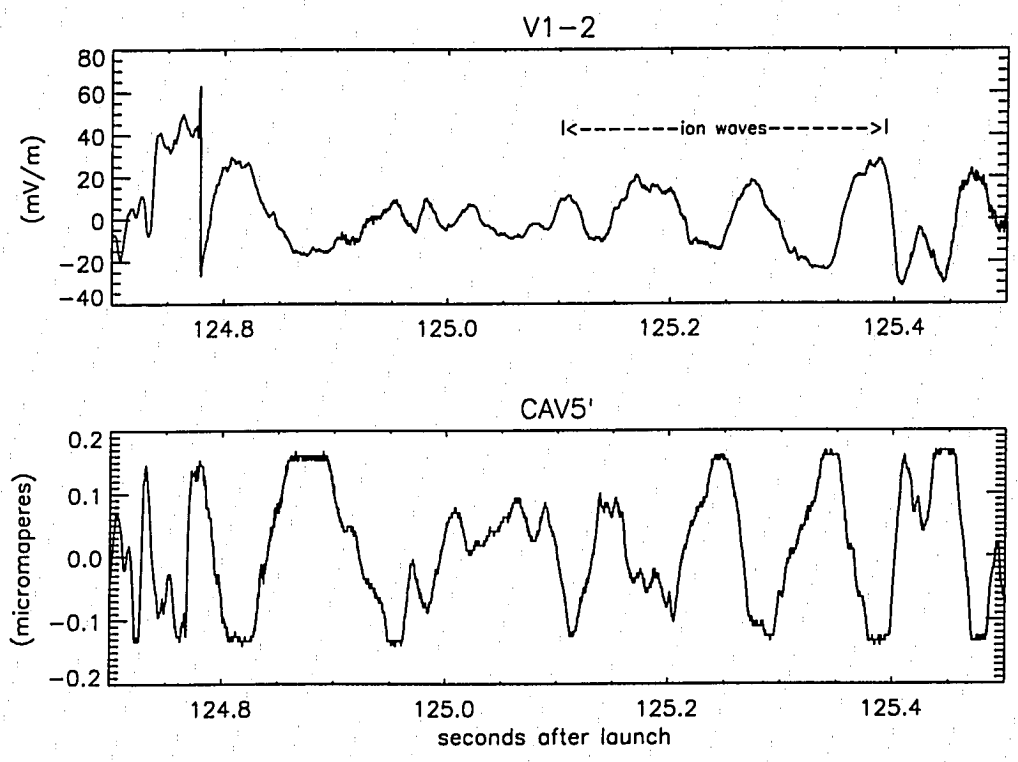

Figure 4-18: *Waveforms for the second ion wave event.*

implicitly interpreted them to be the same wave. There are several reasons why this is plausible. First of all, they are both observed at the same distance from the beam center. This suggests that they are a spatial phenomenon, in steady-state, and that their source is stationary with respect to the ISR beam. If so, then their frequency splitting (24 - 10 Hz) has a simple interpretation as Doppler shift due to spacecraft motion. Furthermore, the thickness of the cylindrical shell where each wave event occurs is $\sim$ 68 meters in each case.

Coincidence of Coherent Waves, Heated Ions

Figure 4-1 clearly shows a burst of superthermal ions following the closest approach to the ISR. The D.C. electric field probe, in the few hundred milliseconds preceding the observation of the energetic ions, displayed several cycles of a wave with a frequency near 10 Hz. These electric field perturbations have corresponding density fluctuations seen by a Langmuir probe, with a phase coherence greater than 0.9(see figures 4-17, 4-18, and 4-19) and a relative phase of $\pi/2$. These facts, taken together with the damping/disappearance of the wave in a region of elevated ion temperature, suggest an ion-acoustic or drift wave mode. Figure 4-20 shows the precise timing of the second ion wave/ion event.

The normalized cross spectrum (see section 5.5) of V1-2 with CAV5, shows, in its magnitude, a high level of broad band coherence at the time when the spacecraft is near the ISR. As can be seen in figure 4-19, such high coherence is unusual, though not unique, in the data. The presence of coherence between two instruments lends plausibility to weak signals, which might otherwise be considered instrumental noise. The time of high coherence, at the low frequencies associated with the ion waves, spans the interval between the ion wave events, and the coherence drops rather sharply before and after this interval (see figure 4-21).

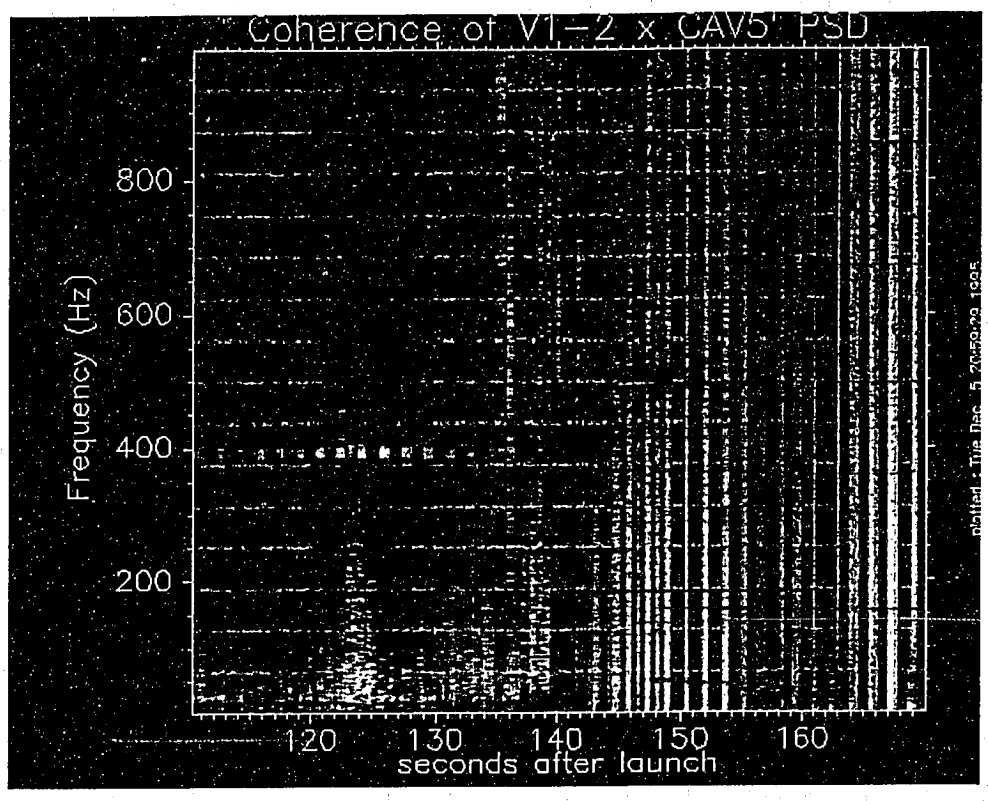

Figure 4-19: *Summary coherence spectrum for V1-2 x CAV5'.* The ISR pass occurs at 122 seconds, where a broad band of high coherence is seen.

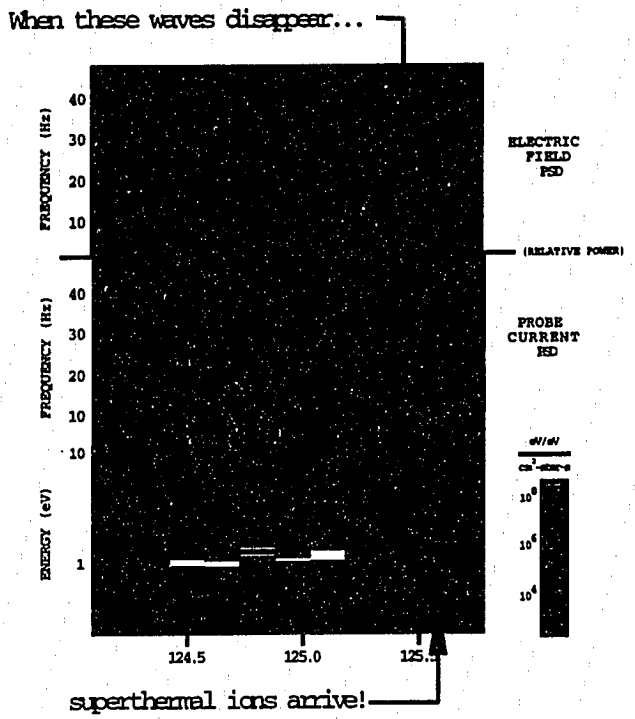

Figure 4-20: *The timing of the ion waves relative to the superthermal ion burst.*

4.4.2 Evidence for a Cylindrical Source Colocated with the ISR

The events I have described, when taken together and analyzed in greater detail, give indications of having a common cylindrical source centered on the ISR beam.

Geometrical Clues

The waveforms for the two "ion wave" events (at 120.6-121.0 s and 125.1-125.4 s) have in common their distance from the ISR beam, their phase relation between field and density, and the approximate length of time for which they are observed. They differ significantly in their location along the length of the ISR beam, and in their apparent period.

The fact that similar ion wave phenomena are observed at the same distance from the beam axis (2.5 km), but at different points along the beam (separated by 10 km) suggests

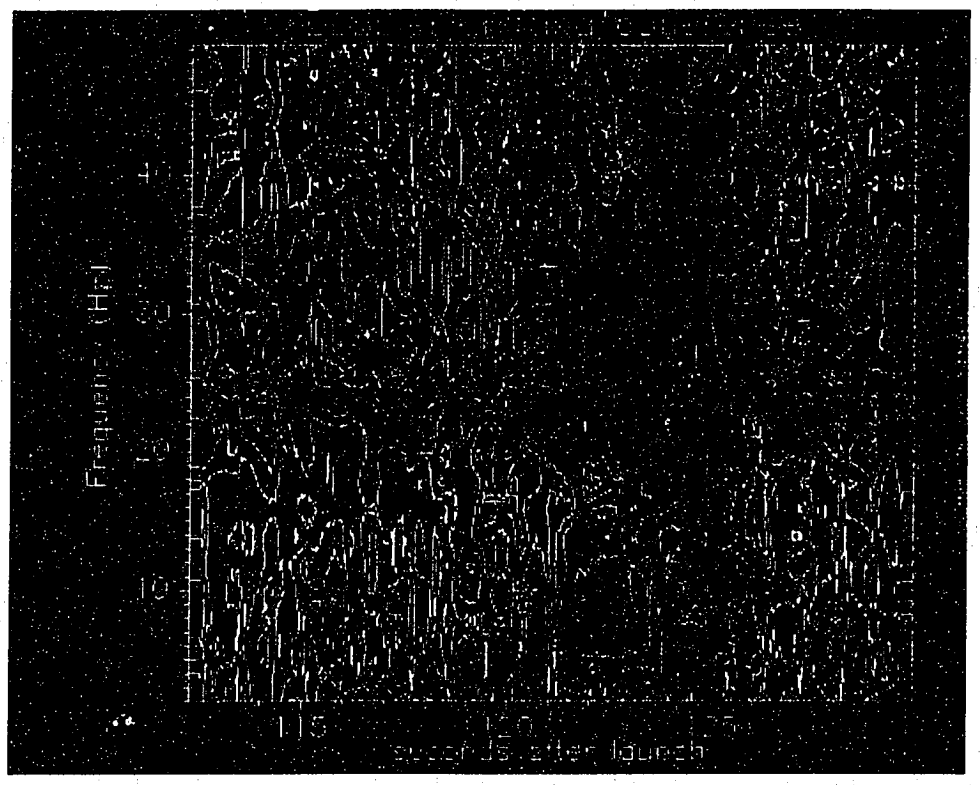

Figure 4-21: *Doppler shift of the V1-2 x CAV5' coherence spectrum.* The two small patches of coherence at (120.8 s, 24 Hz), and (125.0 s, 10 Hz) are both visible in waveform plots (see figure 4-17,4-18) and Fourier transforms(see figure 4-20.) The point of this figure is the band of coherence, the lower edge of which connects these two events.

a cylindrical symmetry for these phenomena. It is not likely that our spacecraft happened to encounter two preferred azimuthal locations at the 2.5 km radius, therefore I interpret our observations as indicative of a cylindrical shell of ion waves, near a radius of 2.5 km. Therefore, the length of time for which these waves are observed is an indication of the thickness of the shell ($\approx$ 68 meters) over which they have measurable amplitude.

Doppler Shifts

A cross-spectral analysis of the density and electric field data reveals several interesting features. First, there is a remarkably high level of coherence during the several seconds spent near the ISR which is not seen elsewhere in the flight (see figure 4-19). Note in figure 4-19 that the coherence exceeds 0.9 across much of the available bandwidth near the ISR, while elsewhere 0.5 is a more typical value. Furthermore, the lower edge of the coherent band can be seen to trace a path from 24 Hz down to 10 Hz in figure 4-21: the frequencies where wave power appears in the regular spectrogram. The relative phase at these two frequencies is $\pi/2$, as expected for an ion acoustic wave. Finally, a classic "thumbprint" pattern is visible in the frequency-time phase plot of figure 4-22. Although "thumbprints" are more typically seen as nulls in the *power* spectrum seen by a rotating antenna in a directed "acoustic" wave field [LaBelle and Kintner, 1989], the picture is qualitatively the same for the relative phase seen by a rotating interferometer. If we ask, "at what frequency will we measure a phase shift of zero?", we find that the answer depends on the angle of the interferometer baseline $\vec{\mathbf{d}}$ with respect to the wave vector $\vec{\mathbf{k}}$. When $\vec{\mathbf{d}}$ is perpendicular to $\hat{\mathbf{k}}$, there is no frequency high enough to squeeze a wavelength into $\vec{\mathbf{d}}$. On the other hand, when $\hat{\mathbf{k}}$ and $\vec{\mathbf{d}}$ are parallel, we find zero phase shift if $\omega = v_\phi/nd$, where v_ϕ is the wave phase speed and n is an integer. This is what produces the "thumbprint".

It is worth noting that there is no hint whatsoever of a thumbprint in a power spectrum of either V1-2 or CAV5. While CAV5, being a scalar measurement, is not expected to produce thumbprints, the absence of thumbprints in a V1-2 spectrum casts some doubt on the validity of the result presented in figure 4-22. Nevertheless, figure 4-22 is intriguing enough to warrant further investigation.

Note that there are, in figure 4-22, three thumbprints: the first extends from 113-122 s, the second from 122-135 s and the third beginning at 135 and fading out around 142 s. Only the second is complete. When considering the difference in the observation intervals of the two ion wave events (119.2-119.4 versus 125.1-125.4), it is noteworthy that the thumbprint pattern has this asymmetry as well, i.e. that the first thumbprint is somewhat compressed relative to the second. Also, note that the ion wave events occur at the same "phase" of the thumbprint sequence.

Because the ion wave events are both observed at the same distance from the beam center, and because the payload moves $\sim$ 10 km *along* the beam, and only 2 km *across* the beam between events, we might reasonably infer a cylindrical symmetry for the wave vectors. Furthermore, since the waves appear to damp out and deposit energy into the plasma, it is reasonable to assume that the $\vec{\mathbf{k}}$ vectors for these electrostatic waves are directed outward from the (admittedly small, and dubiously coupled) source of free energy: the ISR beam.

With these things in mind, it is possible to begin building a self-consistent picture of the plasma environment near the ISR beam. Ion waves are observed to propagate outward from ISR beam, and to damp out and deposit their energy in a layer of heated ions. The elevated ion temperature in this layer is consistent with a rapid damping of ion acoustic waves through ion Landau damping[Stix, 1992].

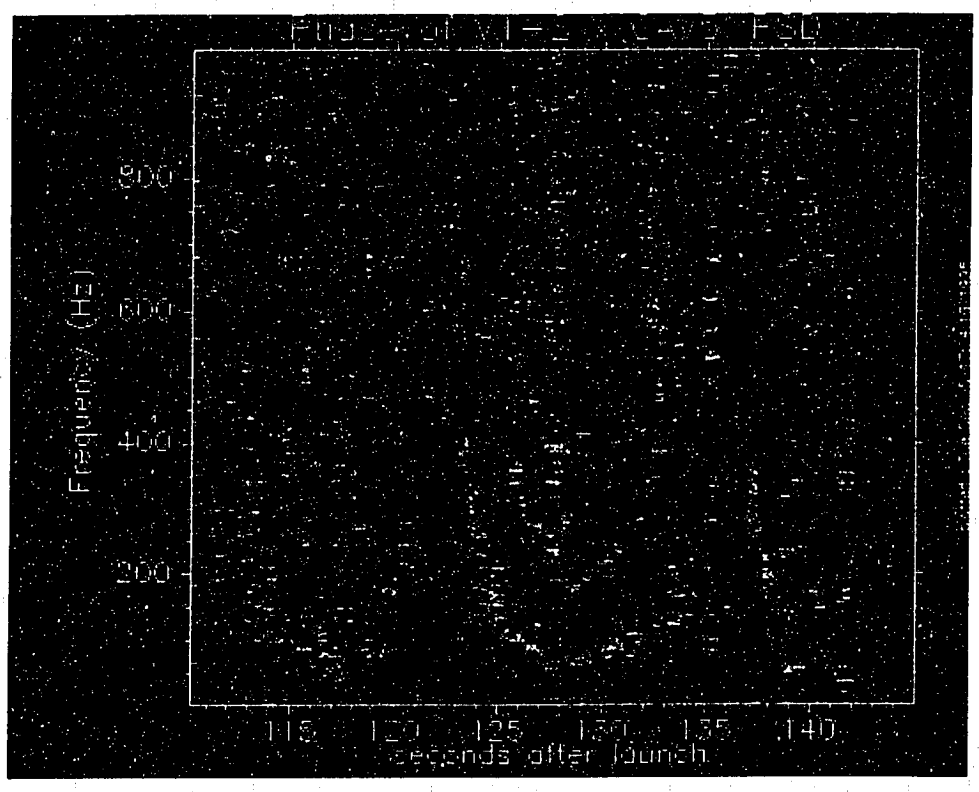

Figure 4-22: ***Phase of the electric field/density coherence spectrum.*** **This result is reminiscent of the classic "thumbprint" pattern for the power spectrum from a rotating antenna in a directed wave field.**

4.4.3 Tapping and Transporting Energy Away from the ISR Beam

Given that perturbations are observed in the vicinity of the ISR (section 4.4.1), and that there are indications that the source of these signals is cylindrical and colocated with the ISR beam (section 4.4.2), it is time to consider mechanisms by which energy might be deposited in the ionosphere by a powerful radio wave of frequency in excess of 100 times the local plasma frequency ω_{pe} . Using, for example, a simple frequency-dependent dielectric constant n to describe the ionospheric medium, we would have $n = 1 - (\frac{\omega_{pe}}{\omega})^2$. In this case, with $\omega = 430$ MHz and $\omega_{pe} < 1$ MHz, n is so close to 1 that it would be difficult to understand refraction, much less dissipation, of the incident wave. Indeed, any plausible mechanism for removing free energy from the ISR will probably employ the ISR's self-evident violation of the plane wave model (it's a beam!), as well as the inherent nonlinearity of its interaction with the ionospheric plasma.

Possible Electromagnetic Interference

It is fairly simple to eliminate electromagnetic interference (EMI) as the source of the ISR effects. The ISR is pulsed at a fairly low duty cycle: a 52 μs pulse is emitted every 11 ms. So, the ISR is usually *off*. If the interaction of this wave power with the ionosphere can be neglected, then the time signature of the ISR should be quite clear in data from this payload, which had dozens of channels with bandwidth in excess of 11 ms, or 91 Hz. And yet there is no such indication; the ISR effects occur on time scales of seconds, with no evident 11 ms pulsing. If on the other hand, the data near the ISR indicate not plasma effects but EMI, which has been somehow smoothed by the ionosphere, then that in itself is an interesting and unexpected interaction of the ionosphere with the ISR. Any mechanism capable of storing the electromagnetic energy of the ISR for a full 11 ms, and

smoothly releasing it at an intensity capable of overpowering the outputs of two entirely different species of electronics, while carefully covering its 90 Hz tracks, is definitely worthy of further study.

Acoustic Waves of Cylindrical Symmetry

In order to decide if the Doppler-shifted ion wave interpretation is correct, it was necessary to find a wave mode which has $\vec{k}$ vectors of the right magnitude and direction to give the measured Doppler shift, $\vec{k}\cdot\vec{v}$, of 14 Hz. The low frequency and ion accelerating characteristics of this wave suggested an ion acoustic wave, but the cylindrical symmetry of the problem put $\vec{k}$ at an oblique angle to $\vec{B}_0$. I therefore chose to test out the electrostatic ion waves derived in [Nicholson, 1983]. I modified his derivation slightly to allow for the cylindrical symmetry $(\hat{\rho},\hat{\phi},\hat{z})$, choosing solutions of the form $\sim \frac{e^{ik\rho}}{(k\rho)^{\frac{1}{2}}}$. This choice has the desired symmetry, and also conserves the wave energy density flux.

Having chosen a form for the solution, I can then proceed to derive a dispersion relation for such a wave. The following substitutions can be made for the vector operators in the linearized two-fluid plasma equations:

$$\nabla\cdot \rightarrow \left(i\vec{k}+\frac{\hat{\rho}}{2\rho}\right)\cdot,\ \ \nabla\times \rightarrow i\vec{k}\times +\frac{\hat{\phi}\cdot}{2\rho},\ \ \nabla \rightarrow i\vec{k}-\frac{\hat{\rho}}{2\rho}$$

The two-fluid equations then become:

$$-i\omega m_e n_0\vec{V}_e = -i\vec{k}\gamma_e T_e\, n_{e1} + \frac{\hat{\rho}}{2\rho}\gamma_e T_e\, n_{e1} - en_0\vec{E} - \frac{en_0}{c}[\vec{V}_e\times\vec{B}_0],$$

$$-i\omega m_i n_0\vec{V}_i = -i\vec{k}\gamma_i T_i\, n_{e1} + \frac{\hat{\rho}}{2\rho}\gamma_i T_i\, n_{e1} + en_0\vec{E} + \frac{en_0}{c}\vec{V}_i\times\vec{B}_0,$$

$$-i\omega n_{e1} + i\vec{\mathbf{k}} \cdot \vec{\mathbf{V}}_{e,i} n_0 + \frac{n_0 V_{e,i\rho}}{2\rho} = 0.$$

I have already assumed $n_{e1} = n_{i1}$, and that $\vec{\mathbf{E}}$ and $\vec{\mathbf{V}}_{e,i}$ are first order quantities. The two momentum equations can be added, eliminating $\vec{\mathbf{E}}$. The result can be dotted into $\vec{\mathbf{k}}$, and with $\vec{\mathbf{k}} \cdot \vec{\mathbf{V}}_{e,i} = \omega N - \frac{V_{e,i\rho}}{2\rho}$, where $N = \frac{n_{e1}}{n_0}$, we get the equation which eventually will form the dispersion relation:

$$-i\omega^2 N + \frac{\omega U_\rho}{2\rho} = (-ik^2 + \frac{k}{2\rho}) c_s^2 N + \frac{eB_0}{Mc} \vec{\mathbf{k}} \cdot \left[(\vec{\mathbf{V}}_i - \vec{\mathbf{V}}_e) \times \hat{\mathbf{b}} \right].$$

Now we can cross $\vec{\mathbf{k}}$ into the electron momentum equation, obtaining:

$$\vec{\mathbf{k}} \times \vec{\mathbf{V}}_e = \frac{\Omega_e}{-i\omega} \vec{\mathbf{k}} \times (\vec{\mathbf{V}}_e \times \hat{\mathbf{b}}),$$

where Ω_e is the electron cyclotron frequency, and the *additional* assumption $E_\phi = 0$ is made at this point. This last equation, together with the electron continuity equation, can be solved for the components of the two fluid velocities:

$$V_\rho = \frac{2i\omega\rho N}{1 + 2ik\rho},$$

$$V_{e,i\phi} = \frac{b_\rho b_\phi + i\alpha_{e,i} b_z}{b_\rho^2 - \alpha_{e,i}^2} V_\rho,$$

$$V_z = \frac{b_\rho b_z - i\alpha_{e,i} b_\phi}{b_\rho^2 - \alpha_{e,i}^2} V_\rho,$$

where $\alpha_{e,i} = \omega/\Omega_{e,i}$, and $\hat{\mathbf{b}}$ is a unit vector in the direction of $\vec{\mathbf{B}}_0$. If ψ is the angle

between $\vec{k}$ and $\vec{B}_0$, then we have $b_\phi^2 + b_z^2 = \sin^2\psi$ and $b_\rho = \cos\psi$. With these substitutions, the dispersion relation can be found:

$$1 = \left(\frac{kc_s}{\omega}\right)^2 \left(1 + \frac{1}{(2k\rho)^2}\right) - \frac{\sin^2\psi(\alpha_i - \alpha_e)(\cos^2\psi + \alpha_e\alpha_i)}{(\cos^2\psi - \alpha_i^2)(\cos^2\psi - \alpha_e^2)} \tag{4.2}$$

In the limit $\omega \ll \Omega_e$, with $b_\rho \gg \alpha_e$, the dispersion relation reduces to the relatively simple expression:

$$\frac{1 - \alpha_i^2}{\cos^2\psi - \alpha_i^2} = \left(\frac{kc_s}{\omega}\right)^2 \left(1 + \frac{1}{(2k\rho)^2}\right) \tag{4.3}$$

These results show that, since $\rho \approx 2500$ meters, and the wavelength is likely to be less than 100 meters, $k\rho \gg 1$, and the modification of the dispersion relation due to cylindrical symmetry is not appreciable in the region where the ion waves are observed.

The group velocity can be computed from the above expression, ignoring cylindrical effects. The result is:

$$\nabla_k \omega \equiv \vec{v}_g = \frac{\alpha^2\hat{\rho} - \cos\psi\hat{\mathbf{b}}}{\alpha^4 + \cos^2\psi(1 - 2\alpha^2)}(\alpha^2 - 1)v_\phi \tag{4.4}$$

The cylindrical electrostatic ion waves derived here have some difficulty explaining in detail the observed Doppler shifting of the ion wave frequencies. Basically, the phase velocity of such a wave (assuming minimal, ambient temperatures) is too large by a factor of 2; it cannot produce a sufficiently large Doppler shift as the source is passed. Furthermore, the wavelength of such a wave, at 15 Hz, is approximately 100 meters; so such a wave mode cannot be invoked to explain the "thumbprint" pattern of figure 4-22.

Stimulated Brillouin Scattering

The waves discussed in the previous section have some properties consistent with the observed ion waves. But how could such waves begin growing? *Fejer* [Fejer, 1979] has calculated threshold powers and spatial growth rates for the parametric instability known as stimulated Brillouin scattering. This instability entails the decay of a forward electromagnetic wave into a forward ion acoustic wave and a backscattered electromagnetic wave. In this case the incident wave from the ISR interacts with its own backscattered component. This produces a ponderomotive force at the difference frequency; it is this nonlinear effect which can be used to grow waves. The waves obey the well-known frequency and wave vector matching conditions, $\omega_{ia} + \omega_{bs} = \omega_{inc}$, and $\vec{k}_{ia} + \vec{k}_{bs} = \vec{k}_{inc}$. The spatial growth rate for this instability was calculated by *Fejer* to be on the order of 10^{-6} m^{-1}, which translates to an asymmetry in the backscattered power spectrum, at the receiver, on the order of 10%, favoring down-shifted EM waves.

Fejer showed that the forward scattered ion acoustic waves grow most rapidly when $\omega_{ia}/k_{ia} = \sigma\sqrt{\frac{2T_i}{m_i}}$ where $\sigma \sim 1 + \frac{1}{4}\frac{T_e}{T_i}$. Since the frequency shift of the backscattered EM wave is small ($\frac{\delta\omega}{\omega} \sim 3 \times 10^{-5}$ in a typical "ion line"), and the phase speed of both the incident and backscattered EM waves is essentially the speed of light, the magnitude of the ion acoustic wave vector is very close twice that of the ISR wave vector, i.e. $k_{ia} = |\vec{k}_{inc} - \vec{k}_{bs}| \approx 2k_{inc}$. For a T_i of 0.1 eV, and a dominant ion O^+, this implies a phase velocity of 1-2 km/s, or a frequency of 3-6 kHz. These numbers describe the shortest wavelength, highest frequency (highest phase velocity) wave which will grow as the forward scattered component of stimulated Brillouin scattering driven by the ISR. Such a wave could plausibly be down-shifted to zero frequency by our payload, which is, at the time of the ISR encounter, moving upwards at 1.7 km/s.

It is clear that the perturbations we see are caused by coupling of the ISR wave power to the local plasma. The exact manner in which this occurs is not entirely clear, but we have presented both an instability and a wave mode from which plausible coupling scenarios emerge. Furthermore, the amount of energy tapped from the beam is quite small. If the ion waves are imagined to be transporting the entire thermal energy density of the irradiated plasma out from the beam at the ion acoustic speed, they can still only account for about 1% of the ISR power flux of 22 mW/m^2. Therefore, it is clear that the perturbations could not manifest themselves as "missing power" at the radar receiver.

It is important to note both the somewhat surprising nature of these observations, and the fantastic improbability of the fact that we were able to gather them at all. The very words "incoherent scatter radar" imply that the scattering of radar power consists entirely of second-order randomly-phased kicks of electrons; indeed, the radar frequency here is over 100 times the local plasma frequency, and a thermal O^+ ion travels less than 10 *microns* during one ISR wave period. Furthermore, a proposal to deliberately fly an unguided sounding rocket into the Arecibo beam would rightly be considered laughable. The beam is simply too small a target, and a rather large body of evidence and experience suggests that the beam produces no measurable plasma effects. It is only the partial failure of a planned experiment, namely, to fly across the Arecibo HF beam, that allowed us to, quite accidently, make these measurements near the Arecibo ISR.

4.5 Summary of Results and Comparisons to Related Work

The *in situ* data gathered by Soliton can be compared with the ground-based measurements. The ion temperature estimate of ~ 0.4 eV is quite high. A more typical value, from ISR measurements, is 0.13 eV. It should be noted, however, that the ISR ion temperature

methods of which we are aware are either

- incapable of altitude resolving the volume of hot ions that we observe, or
- they must reject data as "contaminated by the HF enhanced ion-line". Since the HF enhanced ion line is the signature of strong ion-acoustic (ion heating) fluctuations, this represents an experimental bias towards lower T_i .

Our measurements of the ion temperature are difficult to take seriously. They are simply too much larger than other T_i measurements, and indeed, other T_e measurements. The most likely source of systematic error is the unmodeled spacecraft wake, which presumably causes serious disruptions of thermal ion trajectories behind the spacecraft. So, we see that a satisfactory measurement of T_i during an HF ionospheric heating experiment has yet to be made.

There are no measurements of fluxes of superthermal ions during ionospheric heating experiments. Such ions have, however, been observed in the laboratory during critical frequency heating experiments using microwaves [Wong and Stenzel, 1975]. If the ion plume result can be taken seriously, then it is somewhat revolutionary in this field, since it is difficult to imagine the mechanism for accelerating massive ions all the way up to 50 eV using RF wave power.

Bernhardt et al. have measured the motion of 630.0 nm airglow clouds at Arecibo [Bernhardt et al., 1989]. They interpret their drift as the convection of a density depletion/ HF interaction region; it is, therefore, directly comparable to our electric field based measurements. They obtain primarily zonal (east-west) drifts, with magnitudes as high as 70 m/s. Our drifts our somewhat faster, but in reasonable agreement with theirs. The main difference here is in interpretation: *Bernhardt et al.* considered their drifts to be ambient

ionospheric values, and in fact propose tracking of airglow clouds as a method to *measure* the natural ionospheric drift. We consider our drifts to be heater induced, based primarily on the abrupt shear we observe when the spacecraft exits the heater beam.

Finally, the data near the ISR cannot be compared to other results, simply because there are none. The phenomena we observe cannot represent a sink of a significant fraction of radar power, but they may have an impact on how we understand the details of the scattering of radar power. As ISR techniques grow more sophisticated and sensitive, this detailed understanding may prove crucial to the future of fruitful research at Arecibo.

Chapter 5

Methods of Data Analysis

The results presented in the previous chapter utilize many different techniques for wringing out a maximum of information from minimal data. This chapter will describe these methods in detail.

5.1 Simple Moment Computations

It is possible to obtain simple estimates of the plasma temperature, density, pressure, and perhaps higher moments using count rate vs. energy data and a few simple assumptions. The assumptions are not always terribly valid, but they do allow one a place to start when interpreting particle data, and the method is quite quick and painless to implement.

First of all, we should define what is meant by the effective temperature of a given (possibly non-Maxwellian) plasma. In this case, I simply mean, for each species s:

$$k_B T \equiv \sum_s \frac{1}{2} m_s (< v_s^2 > - < v_s >^2),$$

where

$$< >\equiv \frac{\int d^3v \, ()f}{\int d^3v \, f},$$

and f is the plasma distribution function.

We have, from a given detector after its flight, a set $C_i(E_i)$, of discretely sampled count rates as a function of energy, for a particular species, either ions or electrons. The n^{th} moment of the distribution f, defined as $< v^n >$, can be approximated as $\sum_i \Delta^3 v \; v_i^n f_i$, where $\Delta^3 v$ is the phase space volume over which f is approximated by f_i, and $v_i^n \equiv \left(\frac{2E_i}{m}\right)^{\frac{n}{2}}$. What is the connection between f_i and C_i?

Crudely, we can say that:

$$C_i = \int d^3v \; f v \delta A \eta,$$

which is to say that the count rate is built from the number of particles per unit volume near $\vec{\mathbf{v}}$, namely $f d^3 v$, the volume with access to the detector during the accumulation, namely $v\delta A$, and the efficiency with which events are recorded into the accumulator, namely η. The limits of integration are simply the boundaries of the phase space to which the detector is sensitive, inside these limits, the detector has an efficiency η. This idea is crude since it does not include the *shape* of the detector's *response function*, which will be defined carefully in section 6.1.

Assuming that f is isotropic over the detector's angular response and uniform over its apertures, the above equation becomes:

$$C_i = \eta \delta A \delta \Omega \int d^3v \; v^3 f,$$

or

$$C_i = \frac{2\eta \delta A \delta \Omega}{m^2} \int_{\delta E} dE E f.$$

Next we make the most crucial (and probably least valid) approximation of all, namely that $\int_{\delta E} dE E f \approx \delta E_i E_i f_i$, or, in words, that f is relatively constant over δE , and that

$|\delta E| \ll E$. If this is reasonably true, then we can say, finally:

$$C_i = \frac{2\eta\delta A\delta\Omega}{m^2}\delta E\, {}_i E_i f_i.$$

If we define the constant $G_0 \equiv \eta\delta A\delta\Omega\frac{\delta E_i}{E_i}$, which is independent of energy, we can say:

$$C_i = \frac{2G_0}{m^2}E_i^2 f_i,$$

or

$$f_i = \frac{m^2}{2G_0 E_i^2}C_i.$$

This is the connection between f_i and C_i.

Now we can substitute for f_i in our definition of the n^{th} moment. This yields:

$$< v^n >= \frac{\sum_i \left(\frac{2E_i}{m}\right)^{\frac{n-1}{2}} C_i}{\sum_i \left(\frac{2E_i}{m}\right)^{\frac{1}{2}} C_i},$$

or more specifically,

$$k_B T = \frac{\sum_i E_i^{1/2} Ci}{\sum_i E_i^{-1/2} Ci} - \left(\frac{\sum_i Ci}{\sum_i E_i^{-1/2} Ci}\right)^2.$$

Note that any dependence on G_0 has disappeared in the definition of the n^{th} moment, and that the mass dependence in the moment definition cancels out in the definition of effective temperature.

There are *many* difficulties with this method. First of all, a plasma with zero temperature will cause a detector of finite energy resolution to produce counts in more than one energy bin if the bins have some overlap. Therefore, a cold plasma appears to have a finite

temperature by the above formulas. Furthermore, if the plasma has a significant drift, then it is possible that a detector with a narrow angular field-of-view will be drawing particles from a region of phase space significantly removed from the core of the distribution. Lastly, if the spacecraft becomes charged relative to local plasma potential, then the numbers E_i in the above formula need to be modified. Despite these concerns, it is worth noting that this method yields physically plausible values for ion temperatures on Soliton, and provided a starting point for the search for HF ion heating in this thesis.

5.2 A Model Detector

In order to separate the effects of the heater beam from instrumental, spacecraft wake and charging effects, and effects of the ambient ionosphere , a model detector was developed. This model detector performed the integral convolution described in section 6.1, taking account of spacecraft motion and attitude, external electric field, scattering through the spacecraft sheath, and blind spots caused by objects on the same payload deck.

The response of the model detector is obtained from calibration data for the Soliton electron Bagel. A smoothed-lookup table is used by the model code to obtain the value of $R(E_s, \hat{\mathbf{n}})$, as in equation 6.2, where R is the response function, which represents the sensitivity of a detector to energy fluxes of plasma particles as a function of energy and incidence direction. Figure 5-1 shows a comparison of the measured and modeled detector response.

5.2.1 Plasma for the Model Detector

I used a drifting Maxwellian for a model distribution function $f(\vec{\mathbf{v}})$. Such a model distribution assumes that the ions have had time to reach thermal equilibrium, perhaps at a locally

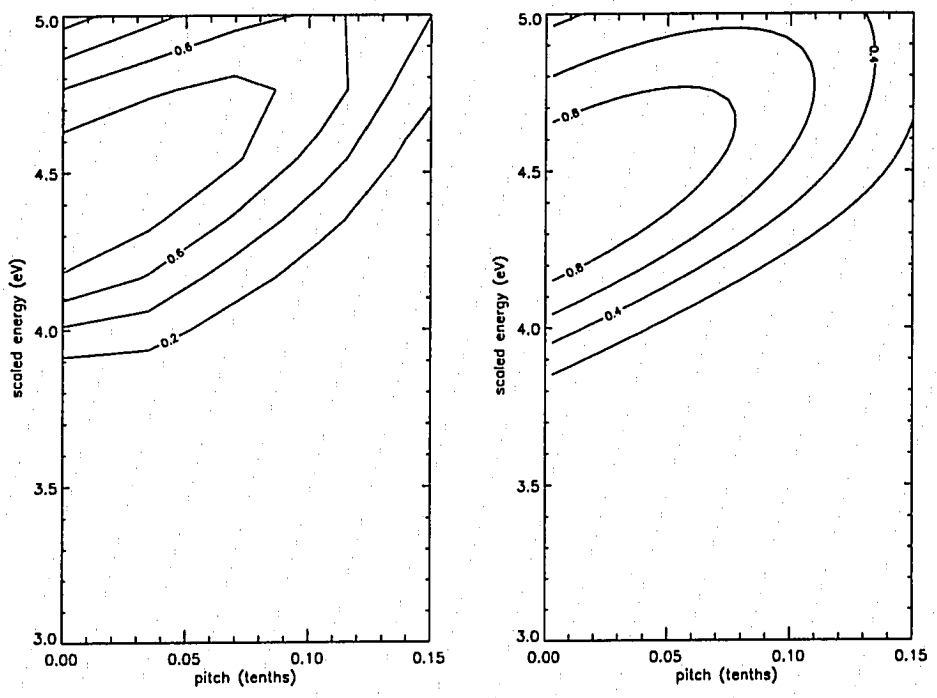

Figure 5-1: *The measured and modeled Bagel response functions*

elevated temperature or depleted density, but an equilibrium nonetheless. This assumption appears quite valid during those times when the spacecraft is above the heater beam; the ions there are either ambient populations unaware of the heater beam, or superthermal ions which have drifted out of the core heated region. In either case, their equilibration can be measured by the fact that they are well-modeled by the drifting Maxwellian, and that successive samplings of the ion population yield small fluctuations consistent with counting statistics. On the other hand, when the payload is in the heater beam, large fluctuations exist in successive samplings of the thermal ions, and the drifting Maxwellian models the ions rather poorly. It is these nonequilibrium qualities of our measurements which can be attributed to the heater beam.

The drifting Maxwellian model, for a species of mass m, number density n, thermal energy T and mean drift $\vec{\mathbf{v}}_D$ can be written as:

$$f(\vec{\mathbf{v}}) = n(\frac{m}{2\pi T})^{\frac{3}{2}} \exp(-\frac{\frac{1}{2}m(\vec{\mathbf{v}} - \vec{\mathbf{v}}_D)^2}{T}), \tag{5.1}$$

where the following definitions will be used:

$$v_{\|R} = \vec{\mathbf{v}}_R \cdot \vec{\mathbf{B}}_0,$$

$$\vec{\mathbf{v}}_D \equiv \frac{\vec{\mathbf{E}} \times \vec{\mathbf{B}}_0}{B_0^2} - v_{\|R}\hat{B},$$

$$\vec{\mathbf{v}} \cdot \vec{\mathbf{v}}_D \equiv v v_D \cos\alpha,$$

where $\vec{\mathbf{E}}$ is the spacecraft frame electric field, $\vec{\mathbf{B}}_0$ is the geomagnetic field, and $\vec{\mathbf{v}}_R$ is the

spacecraft velocity.

Since our detector measures ion energies, not velocities, it is useful to express equation 5.1 in terms of energies.

$$f(\vec{v}) = n(\frac{m}{2\pi T})^{\frac{3}{2}} \exp(-\frac{\frac{1}{2}m(v^2 - 2vv_D\cos\alpha + v_D^2)}{T}),$$

$$f(E,\alpha) = n(\frac{m}{2\pi T})^{\frac{3}{2}} \exp(-\frac{E - 2(EE_D)^{\frac{1}{2}}\cos\alpha + E_D}{T}),$$

where $E_D \equiv \frac{1}{2}m_i v_D^2$.

This equation describes the distribution function in the frame of reference moving with the payload, but outside the spacecraft sheath. Denoting the energy inside the spacecraft sheath as E_s, and the kinetic energy added to an ion falling through the spacecraft sheath as ϕ, we have

$$E = E_s - \phi,$$

which then gives

$$f(E_s,\phi,\alpha) = n(\frac{m}{2\pi T})^{\frac{3}{2}} \exp(-\frac{(E_s - \phi) - 2((E_s - \phi)E_D)^{\frac{1}{2}}\cos\alpha + E_D}{T}) \qquad (5.2)$$

This model distribution can be inserted into the convolution integral derived in the previous section, equation 6.2. The integral is then performed numerically, and the model parameters are adjusted to give the best fit to the data.

5.2.2 Evaluating the Convolution Integral

"Integrals of functions of several variables, over regions with dimensions greater than one, are *not easy*"[Press et al., 1989]. The integral in equation 6.2 is no exception. Initially, I handled all three dimensions of 6.2 numerically, which proved to be prohibitively slow. I was eventually able to find a way, however, to analytically reduce the dimensionality of the integrand, so that only two dimensions are handled numerically. I assumed that the azimuthal variation of the detectors response function was negligible, and was therefore able to evaluate this part of the integrand separately. If the detectors response function could be modeled as a rational function or something similar, it might even be possible to evaluate the energy part of the integral as a sum of residues, over all the poles of the resulting integrand. I was not successful at this however, and the integrations performed for this thesis were done numerically over energy and polar angle, and analytically over azimuth.

Evaluating the Integrand

There are several steps involved in the evaluation of the integrand of equation 6.2. First, it is necessary to choose the region of particle phase space which will be examined. The integral is performed in terms of the particle energy at the spacecraft E_s, the angle between the detector symmetry axis and the particle velocity, θ, and the azimuthal angle b between the payload zero degree mark and the projection of $\vec{\mathbf{v}}$ onto the spin plane. In other words, E_s, θ, and b are the independent variables over which the domain of the numerical integration is defined. The value of the model distribution function is then computed for each given value of these independent variables. Uniform steps are taken in θ and b, while E_s is sampled logarithmically, allowing the exponential nature of the Maxwellian model distribution to be

represented in the fewest possible energy steps.

In order to evaluate the model distribution function described in a previous section, it is necessary to translate from (E_s, θ, b) space into (E, α) space. It may seem that a variable has been lost somewhere: this is because the drift velocity $\vec{\mathbf{v}}_D$, about which the model distribution is symmetric, is a measured parameter and is not allowed to vary. For a given known spacecraft attitude and measured drift velocity, α can computed from (E_s, θ, b). Figure 5-2 shows the spherical triangles which must be solved to compute α.

The response function can be evaluated directly given (E_s, θ, b), and I chose to implement this as a lookup table derived from the raw detector calibration data. Figure 5-1 shows a plot of the detector's measured response function vs. E_s/V, along with the smoothed lookup table values for the same detector parameters. The plot is made for particles from a particular direction, near the symmetry axis of the detector. No attempt was made to model the measured (small) b dependence of the detector's response. However, b was initially used to model the obstruction of particles from the detector by a search coil housing located nearby the detector during its flight operations. If b was within 8^o of 135^o, the response function was set to zero.

The change in count rate due to such a blind spot proved to be insignificant, so I decided, as mentioned above, to perform the integration analytically. It is not immediately apparent in 5.2 where the azimuthal angle b enters; it is hidden in $\cos\alpha$. Using spherical trigonometry and figure 5-2, we can obtain

$$\cos\alpha = \cos\theta_i \cos\beta + \sin\theta_i \sin\beta \cos\psi,$$

where ψ is the measured in the sense of a right-handed rotation of $\vec{\mathbf{v}}_D$ around $\hat{\mathbf{n}}_D$, and is

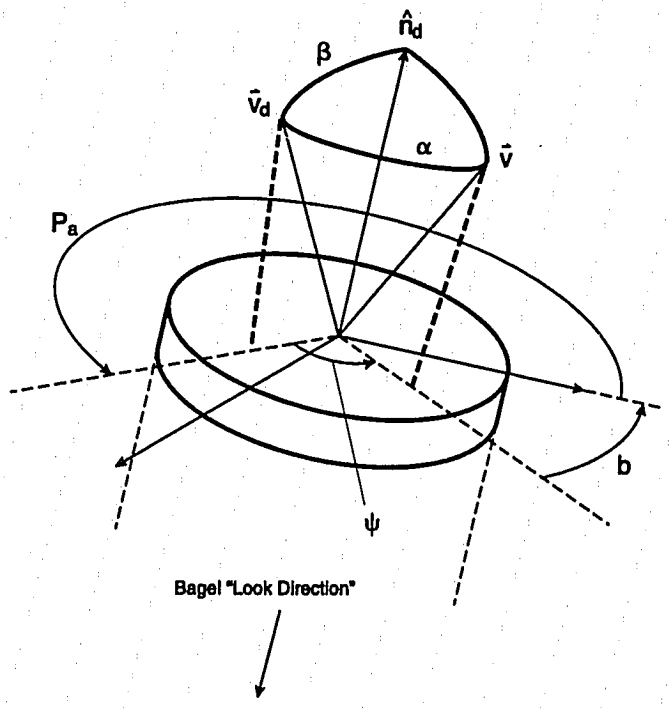

Figure 5-2: *The spherical triangles used in evaluating the model detector response function.*

the angle between the plane defined by $\vec{\mathbf{v}}_D$ and $\hat{\mathbf{n}}_D$ and that defined by $\vec{\mathbf{v}}$ and $\hat{\mathbf{n}}_D$. There is also the angle p_a, such that

$$p_a + b + \psi = 2\pi.$$

Note that figure 5-2 uses an angle θ_i, rather than θ, which is used to evaluate the response function. This is because a charged particle, on entering the spacecraft sheath, is scattered according to the relation:

$$\sqrt{\frac{E}{E+\phi}} = \frac{\sin\theta}{\sin\theta_i},$$

which can be rewritten as:

$$\sin\theta_i = \sqrt{\frac{E_s}{E_s - \phi}}\sin\theta.$$

Performing the Integration

The integrand in equation 5.2 is zero for $E_s < \phi_p$, so the energy part of the integration can use this as a lower limit. The azimuthal part is of the form

$$\int_0^{2\pi} \exp(p\cos b + q\sin b)db.$$

This can be evaluated analytically, using the following formula [Gradshteyn and Rhyzhik, 1994]:

$$\int_0^{2\pi} \exp(p\cos x + q\sin x)(a\cos x + b_*\sin x - mx)dx =$$

$$\pi[(b_* - p)^2 + (a+q)^2]^{\frac{-m}{2}}\{(A+iB)^{\frac{-m}{2}} I_m(\sqrt{C-iD}) + (A-iB)^{\frac{-m}{2}} I_m(\sqrt{C+iD})\},$$

where

$$A = p^2 - q^2 + a^2 - b_*^2,$$

$$B = (2pq + ab_*),$$

$$C = p^2 + q^2 - a^2 - b_*^2,$$

and

$$D = 2(ap + b_*q),$$

and I_m is the modified Bessel function of order m. For our case, this simplifies to

$$\int_0^{2\pi} \exp(p\cos x + q\sin x) = 2\pi I_0(\sqrt{p^2+q^2}).$$

This procedure, while it leaves out any possible b dependence in the detector response function, *greatly* reduces the computation time.

The integrand to be evaluated is, explicitly,

$$\eta = E_s n_0 \left(\frac{m}{2\pi T_i}\right)^{\frac{3}{2}} \exp\left(\frac{-1}{T_i}((E_s - \phi_p) - 2(E_s - \phi_p)^{\frac{1}{2}} E_D^{\frac{1}{2}} \cos\alpha + E_D)\right) R_i(E_s, \hat{\mathbf{n}}).$$

Defining

$$Z = n_0 \left(\frac{m}{2\pi T_i}\right)^{\frac{3}{2}} \exp(\phi_p - E_D)/T_i\,,$$

$\epsilon = E_s/T_i$, $\epsilon_D = E_D/T_i$, and $p = \phi_p/T_i$, we get

$$\eta = Z E_s e^{-\epsilon} e^{c} e^{s\cos p_a \cos b} e^{-s\sin p_a \sin b} R_i,$$

where

$$c \equiv 2(\epsilon - p)^{1/2}\epsilon_D^{1/2}\cos\theta_i\cos\beta,$$

and

$$s \equiv 2(\epsilon - p)^{1/2}\epsilon_D^{1/2}\sin\theta_i\sin\beta.$$

From the formula discussed above, integration over b gives

$$\eta_b \equiv 2\pi Z E_s e^{-\epsilon} e^c R_i(E_s,\theta) I_0(s).$$

5.2.3 Dead-time Saturation

Any system which measures event rates by accumulating or tagging events suffers from what is called dead-time limiting or saturation[Knoll, 1989], a condition which puts an upper bound on measurable event rates. In essence, dead-time saturation is caused by the fact that a finite time is required for the recording of an event, and no other event may be recorded during this time, called the dead-time or τ_D . The maximum recorded event rate is then typically on the order of $1/\tau_D$.

In our detector systems, there is dead-time limiting in several places, primarily in the electronics. The charge-sensitive amplifier (CSA) typically has a dead-time of 1.3 μs. τ_D is measured by applying appropriately conditioned pairs of pulses to the CSA inputs and measuring the minimum inter-pulse delay for which the CSA produces output pulses.

There are two distinct types of dead-time saturation, and therefore two distinct means of correcting the corresponding systematic error. One type is called non-paralyzable, and has the basic desirable property that as the event rate tends to infinity, the recorded event rate (or count rate) tends asymptotically toward a finite value, namely $1/\tau_D$. The other

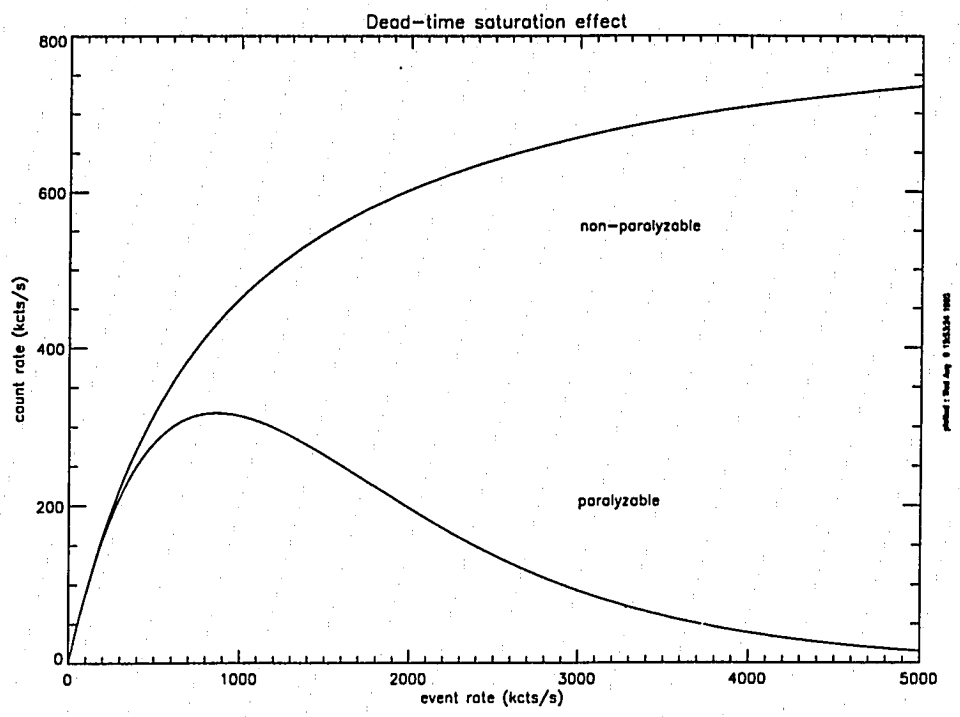

Figure 5-3: *Two possible models for dead-time saturation*

type, called paralyzable, has the hugely undesirable property that as the event rate tends to infinity, the count rate reaches a maximum ($1/e\tau_D$), and then drops rather steeply back to zero. As can be seen in figure 5-3, this results in a multi-valued relation between recorded counts and events, and therefore when one is trying to invert count rates to obtain differential energy flux, there is always the additional complication, with paralyzable dead-time saturation, that there are two possible event rates for every recorded count rate.

Derivation of the Dead-time Corrections

It is possible to derive formulas for dead-time saturation using simple assumptions about the probability of events per unit time. If every instant δt is equally likely to contain an event, then the distribution of finite time intervals t between events is the Poisson distribution:

$$P(t) = r\exp(-rt),$$

where r is the probability per unit time of an event occurring. The mean time between events can thus be calculated:

$$< t >= \int tP(t)dt,$$

resulting in a "count rate" of

$$\frac{1}{< t >} \equiv c_m = r,$$

which is not particularly surprising. Note that $P(t)$ is properly normalized, and that in this case the probability per unit time of an event is numerically equal to the count rate.

In the non-paralyzable model, $P(t)$ is zero for $t < \tau_D$, and must be renormalized, since the probability of seeing another event, after waiting an infinitely long time, must be equal to 1. So

$$< t >= \frac{\int_{\tau_D}^{\infty} tP(t)dt}{\int_{\tau_D}^{\infty} P(t)dt}.$$

Inserting $P(t)$ and performing the integration, we get

$$< t >= \frac{\exp(-c_a\tau_D\ )[\tau_D\ + \frac{1}{c_a}]}{\exp(-c_a\tau_D\ )},$$

or

$$c_a = \frac{c_m}{1 - c_m \tau_D},$$

where $c_a \equiv r$.

The paralyzable model for dead-time alters this procedure somewhat. Fundamentally, the difference is that there is no longer any reason to expect that a second event will ever be recorded. Imagine that an event has just occurred. A succeeding event, if it occurs during the dead-time, will not only fail to be recorded, but will cause a restart of the dead-time interval. In the limit of an infinite event rate, then, the measured count rate will be zero. Since the recording of an event must be preceded by an event-free interval equal to or longer than the dead-time, the probability per unit time of *recording* an event, r_m, is equal to the probability per unit time of the *occurrence* of an event, r, *times* the probability of a sufficiently long open interval, $\exp(-r\tau_D)$, i.e.

$$r_m = r \exp(-r\tau_D).$$

As we saw above, in the case with zero dead-time, this probability per unit time r_m can be identified with the count rate c_m, since no renormalization is necessary. So, we have

$$c_m = c_a \exp(-c_a \tau_D).$$

This result is also derived by [Knoll, 1989], although with a somewhat different intuitive perspective.

Avoiding Paralyzable Deadtime Ambiguity

The model detector method avoids the difficulty of deciding how to invert counts into differential energy flux by approaching the problem from the opposite direction. In other words, the output of the model detector has, like the real system it is simulating, a dead-time saturation built into it. The only decision which needs to be made is in fact which type of dead-time should be built into a given model detector. There is, fortunately, a straightforward method for making this decision.

It is possible to distinguish between the two types of deadtime saturation by examining a histogram of count rates recorded by a detector during its flight. This has been done in figures 5-4 and figure 5-5 which shows such histograms from two different rocket flights, Soliton and TOPAZ3. Note that while both histograms fall to zero above a certain maximum count rate, the manner in which they do so is dramatically different. Soliton, which has a paralyzable dead-time, shows an order of magnitude drop in the count rate occurrence frequency just above 300 kHz. TOPAZ, on the other hand, shows a count rate occurrence frequency which drops smoothly to zero at around 175 kHz. The Soliton data are consistent with the case where event rates are visiting the region of figure 5-3 where the count rate maximum is observed: as the event rates occur more or less uniformly in this neighborhood, count rates are recorded more or less uniformly, but *never* larger than the maximum allowed by dead-time. On the other hand, the TOPAZ3 data are consistent with either non-paralyzable dead-time, or with paralyzable dead-time with event rates well below the limit seen in figure 5-3. As event rates vary in the region of the asymptotic limit, there are indeed fewer samplings of higher count rates, but the occurrence frequency goes to zero gradually; there is no sharp cutoff.

Furthermore, on Soliton, the dead-time was measured in the lab in the manner described

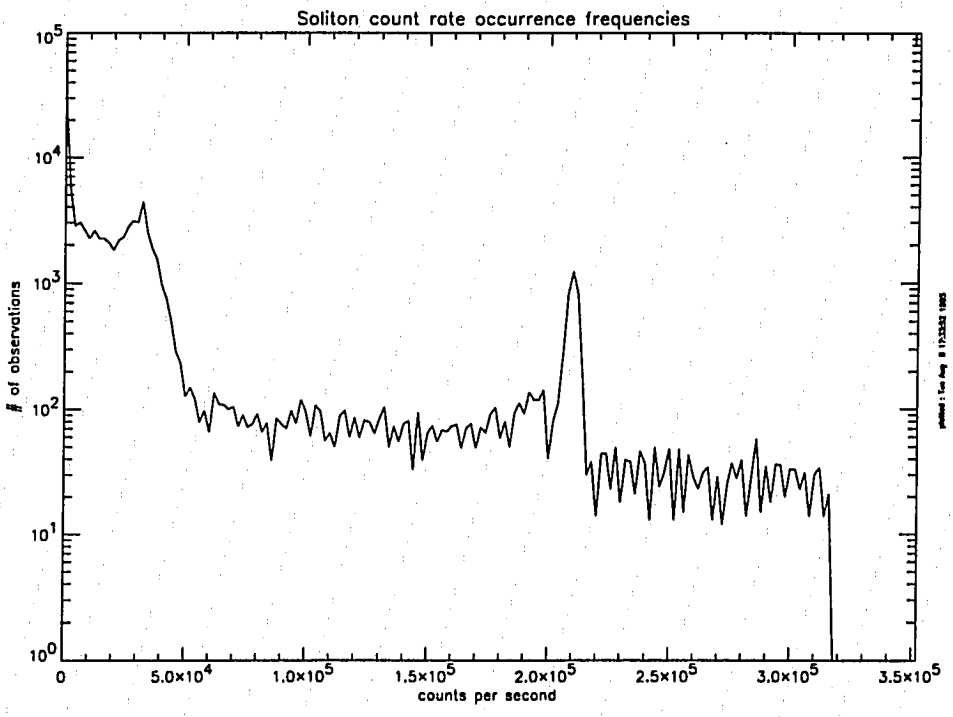

Figure 5-4: *Count rate occurrence frequencies for Soliton.* The sharp cutoff at 310 kHz indicates paralyzable dead-time.

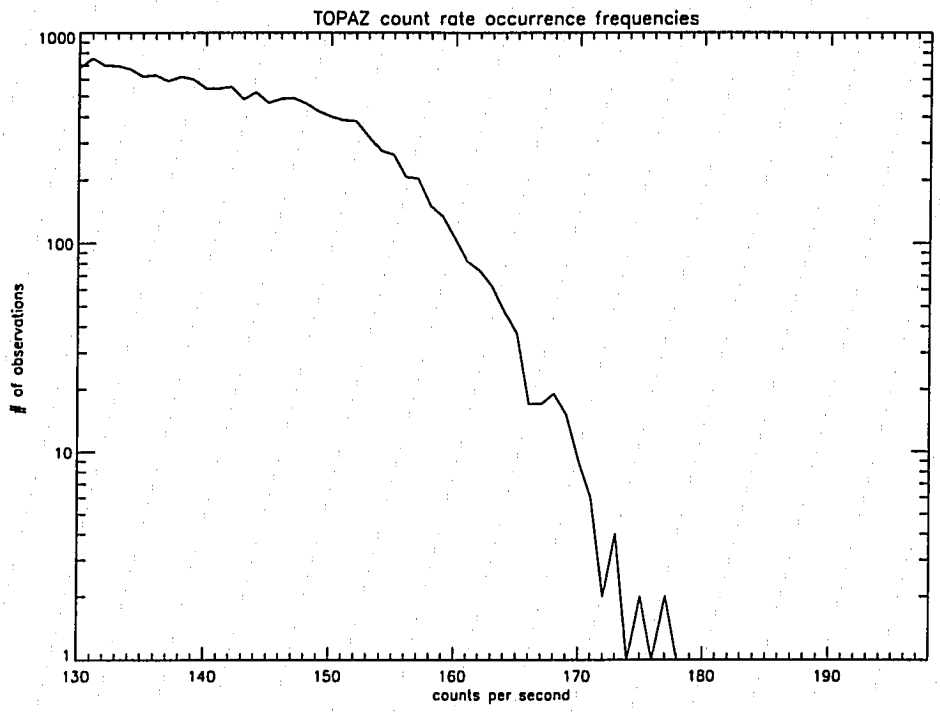

Figure 5-5: *Count rate occurrence frequencies for TOPAZ3.* No sign of paralyzable dead-time saturation is visible.

above. The value recorded there agrees exactly with the paralyzable dead-time inferred from the sharp cutoff in count rate occurrence frequency seen on Soliton. Thus, there is no difficulty in choosing a dead-time saturation algorithm for use in the model detector.

Using the Model to Estimate Parameters

The model detector has several free parameters which one may use to try to match the data from the actual physical detector. Of these, the most important, both scientifically and for determining the output, are the temperature, density, and spacecraft potential. The drift is inferred from the electric field data, and the dominant ion mass is occasionally varied, but generally taken, with some confidence, to be 16 amu for O^+.

In this particular experiment, the density is well-known at the heater reflection altitude, where the heater frequency of 5.1 MHz matches the local plasma frequency. While it is possible to derive information on the ion temperature from incoherent scatter radar [Djuth et al., 1987a], this was not done during the Soliton rocket flight. Nevertheless, the temperature is expected to be in the range of 500-2000K. The truly difficult parameter, in terms of a reasonable starting value for the model, is the spacecraft potential. Note that the model distribution is normalized by a factor $n_0 \exp(\phi/T_i)$. ϕ also determines the rate at which f decays, in combination with E_s under the square root.

A general rule-of-thumb for spacecraft in the night-time F layer is that they will charge negatively to around $5T_e/e$, as discussed in section 5.3. Soliton appears to have not obeyed this particular rule; however, a clue about the precise value of the spacecraft potential can be obtained from the probe current at 146 seconds after launch. At this time, the probe current comes abruptly on scale, at the same time that the poorly known but apparently rather high spacecraft potential drops rapidly (see figure 5-6, 4-1). I interpret this to be the

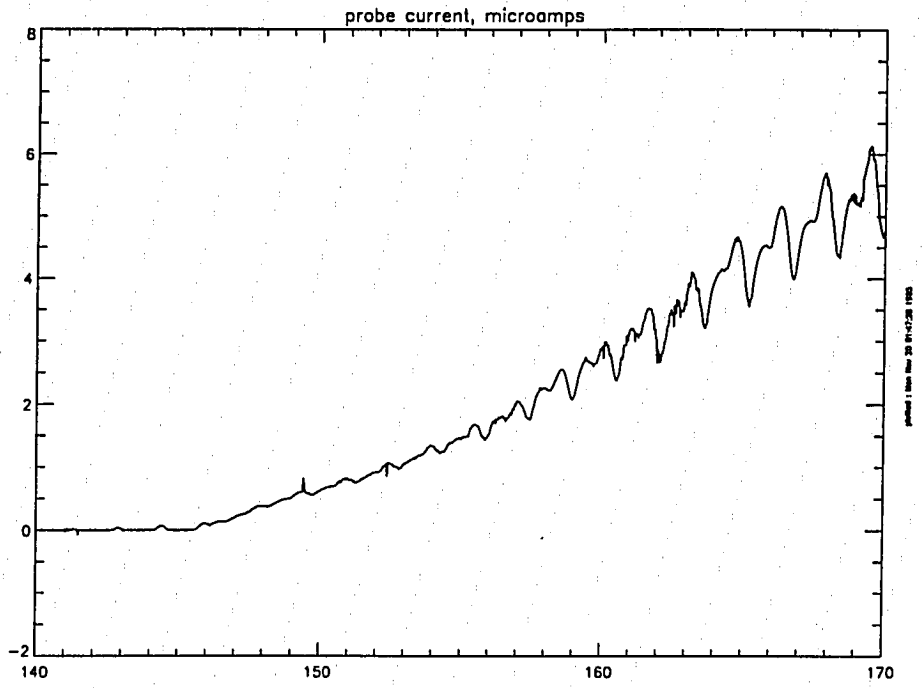

Figure 5-6: *Survey of CAV5' data.*The probe begins drawing electron curren when at 145 seconds. At this time, therefore, its bias must be close to the plasma potential.

moment when the spacecraft potential is equal to the probe bias of 3.04 volts.

At this time therefore, I attempted to obtain a best fit of the model output to the particle data. The result is summarized in figure 5-7.

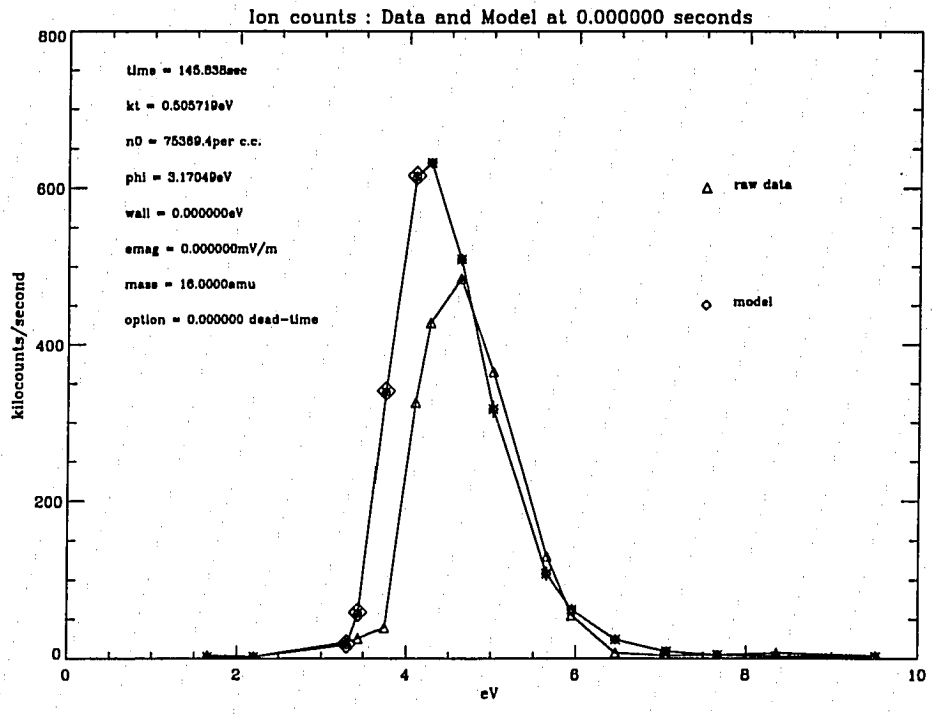

Figure 5-7: *A sample of the model detector's output.*

5.3 Spacecraft Charging

The red stripe of thermal ions in figure 4-1 sits at an apparent energy which is surprisingly high. Crudely speaking, one expects the count rate, for a Maxwellian plasma, to be

$$C = \alpha E^2 \exp(-E/T),$$

where E is the sampled particle energy, T is the thermal energy, and α is a constant which is independent of energy, so that

$$\frac{\partial C}{\partial E} = C\left(\frac{2}{E} - \frac{1}{T}\right).$$

Thus, the maximum count rate is expected at $E = 2T$, which, for the F layer ionosphere, is ~ 0.2 eV. The thermal ions in figure 4-1 appear at a much higher energy which must correspond to the charging of the spacecraft to a potential of 1-5 volts below that of the surrounding plasma. Any electrode placed in a dense plasma will charge negatively, because, at the plasma potential, the thermal electron current to its surface is much larger than the thermal ion current. The electrode therefore accumulates a negative charge and begins repelling the mobile electrons. An equilibrium or zero-current condition is reached, for a sphere in a dense $O^+ - e^-$ plasma, at around $5\frac{T_e}{e}$. Such effects are well-known from geosynchronous satellites, in the Earth's shadow (i.e. in the absence of photoelectrons), *kilovolt* spacecraft potentials are sometimes observed. Our rocket flight occurred entirely in darkness, so there is no photoelectron flux to affect the spacecraft charging. The value of our spacecraft potential, then, indicates a simple balance between thermal electron and ion fluxes: a zero-current condition at the spacecraft. In this section, I will describe method

for using the charging of our spacecraft to measure the superthermal electron flux from the heater.

The standard way of inferring the spacecraft charging potential from an ion distribution measurement is to locate the apparent energy at which the maximum count rate is recorded, E_p. If E_p is much larger than the accepted ion temperature, it must then be the case that thermal ions have been accelerated through the spacecraft potential drop ϕ_p , and the energy at which they appear, E_p, is in fact a good approximation to ϕ_p . (Actually, one expects an electrostatic analyzer to measure the peak count rate at an energy approximately equal to ϕ_p plus *twice* the thermal energy, but the thermal energy is typically much smaller than the spacing between adjacent energy steps, so it can be ignored for the purpose of determining ϕ_p .) It is worthwhile to note at this point that ϕ_p is a positive number, equal to the kinetic energy added to an ion as it's collected by the spacecraft.

A glance at the summary ion spectrogram from Soliton thus immediately reveals a level of spacecraft charging of 3-5 volts negative with respect to the surrounding plasma. For the typical mid-latitude F region (T_e ~0.1 eV). The charging seen on Soliton, therefore, is between $30\frac{T_e}{e}$ and $50\frac{T_e}{e}$ an order of magnitude larger than expected. Furthermore, this charging is time-variable, indicating that it may in fact be a diagnostic of plasma conditions in and around the HF beam.

The high level (for the ionosphere) of spacecraft charging seen on Soliton may be caused by heater-induced fluxes of superthermal electrons. If so, it should be possible to use the inferred spacecraft potential as a probe of the total electron flux collected by the spacecraft. As will be seen below, a steady spacecraft potential of such large magnitude is an indicator of a balance between the *thermal* ion flux and the *superthermal* electron flux to the payload skin.(This is because the thermal *electron* flux is reduced by a factor $\exp(-\frac{\phi_p}{T})$ and can be

ignored). Therefore, since we have measured the thermal ion flux directly and inferred the spacecraft potential, we can infer the energy-integrated superthermal electron flux.

First it is necessary to compute the total number flux, of each species, seen by an element δA of a large electrode, at a potential -ϕ_p , in an equilibrium plasma. Note the unusual sign convention of ϕ_p ; it was chosen so that ϕ_p represents the kinetic energy added to a collected particle as it passes through the spacecraft sheath. For each species, the number flux per unit area is

$$dJ_s = v_f f d^3 v_f,$$

where f is the phase space density, and v_f is the velocity of a particle as it is collected by the payload, i.e. after passing through the spacecraft sheath. Note that f is known in terms of v_i, which is the particle velocity *outside* the spacecraft sheath. In particular take

$$f = \alpha \exp(-\frac{\frac{1}{2}m_s v_i^2}{T_s})$$

with $\alpha \equiv n\left(\frac{m_s}{2\pi T_s}\right)^{3/2}$. In terms of v_f, then,

$$f = \exp(\phi_p/T_s)\alpha \exp(-\frac{\frac{1}{2}m_s v_f^2}{T_s}).$$

Note that none of the factors forming dJ_s, other than the phase space volume element itself, has any angular dependence. Therefore the angular integration can be done immediately, over the plasma-filled half-space, to yield:

$$J_s = 2\pi \exp(\phi_p/T_s)\alpha \int_A^B v_f^3 \exp(-\frac{\frac{1}{2}m_s v_f^2}{T_s}) dv_f,$$

where A and B are the limits of integration for each species. Note that while B is infinite

for both species, A is equal to zero for the repelled species, and equal to $\sqrt{2\phi_p/m_s}$ for the collected species.The integral evaluates to

$$\sqrt{\frac{2}{\pi}}\exp(\phi_p/T_s)\exp(-\frac{1}{2}m_sA^2/T_s)(1+\frac{1}{2}m_sA^2/T_s).$$

For an electron-ion Maxwellian plasma, then, with electron and ion masses m_e and m_i, temperatures T_e and T_i , of locally uniform density n, the thermal ion flux Γ_i to a negatively-charged spacecraft is

$$\Gamma_i = \sqrt{\frac{2}{\pi}}n\sqrt{\frac{T_i}{m_i}}\left(1+\frac{\phi_p}{T_i}\right),$$

while the electron flux Γ_e (thermal *and* superthermal) is

$$\Gamma_e = \sqrt{\frac{2}{\pi}}n\sqrt{\frac{T_e}{m_e}}\exp(-\phi_p/T_e\ ) + \Gamma_s,$$

where Γ_s represents the *superthermal* electron flux.

Since $\Gamma_{e-thermal} \sim e^{-50}$, we can simply say that

$$\Gamma_s = \sqrt{\frac{2}{\pi}}n\sqrt{\frac{T_i}{m_i}}\left(1+\frac{\phi_p}{T_i}\right),$$

which directly yields the superthermal electron flux. Note that in this regime ($\phi_p \gg T_e$), the superthermal electron flux varies linearly with ϕ_p .

This method can fail however, in the case where the spacecraft potential sheath structure is not simple but in fact has one or more extrema [Hutchinson, 1987][McFadden, 1995]. Ions with energies less than the largest *positive* potential peak are repelled and unable to reach

the spacecraft. If the magnitude of the positive potential peak is larger than that of the final sheath drop, then this latter effect plays a larger role in determining the energy where the maximum count rate is observed.

Another difficulty with this method is that the superthermal flux is directly proportional to the plasma density, which is changing rather rapidly as we approach the heated layer. Unless n is known quite accurately, it is difficult to get a *profile* of the superthermal electron flux. We, can however, still make a point estimate at the reflection height, where the density is well-known. Finally, neither the ion temperature nor the electron temperature is measured in this experiment. To produce figure 4-13 I simply used a "typical value" of 0.1 eV.

After 170 seconds on Soliton, the spacecraft potential appears to settle out at 3.0 volts, which, coincidentally or otherwise, is the Langmuir probe bias potential. In order to make figure 4-13, I removed this 3.0 volt contribution. I cannot give a satisfying reason for doing so, except that it yields the physically reasonable result that the spacecraft potential (and the superthermal electron flux!) decreases to a constant value of zero away from the heater, rather than a constant value of 3.0 volts.

The entire payload is being used as a floating Langmuir probe in this method, and the probe theory analysis for this case (magnetized, "collisionless") is not simple (as above), unless the dimensions of the probe perpendicular to $\vec{\mathbf{B}}$ are much smaller than the ion gyroradius. If this condition is violated, then it is collisional effects, rather than the decay of collected trajectories, which causes a return to quasi-neutrality at the sheath edge [Hutchinson, 1987]. It may be that complexities of this nature are defeating the simple method I have described.

5.4 Spectral Analysis

Standard methods of spectral analysis were employed in this thesis for the purpose of picking out interesting features in the wave data in the presence of noise. The fast-Fourier transform (FFT) algorithm [Press et al., 1989] for computing Fourier series [Churchill and Brown, 1963] provided with the Interactive Data Language (IDL) software package was used as the basis for computing frequency-time spectrograms of the time series from the V1-2, V3-4 electric field booms, as well as the CAV5 fixed-bias Langmuir probe. The IDL routine GETSPEC.PRO was written and used to compute individual FFT's. GETSPEC removes average values and linear trends from the time series, applies a tapering window to make the data periodic, and returns the amplitude spectrum.

In order to compute a frequency-time spectrogram (DFT), it is necessary to first choose the range of frequencies to be examined and the required frequency resolution, or, similarly, the time scales of the phenomena to be investigated. A given time series places mathematical limits on all of these.

First, it is clear that a discretely sampled time series cannot contain information about arbitrarily short time scales. It turns out that the shortest resolvable time scale for the FFT is in fact equal to $2\Delta t$, where Δt is the time required to obtain one time series point [Press et al., 1989]. One can imagine that to uniquely reconstruct a continuous sinusoid from discretely sampled points, at least two points are required for each period. This intuition turns out to be valid, and the maximum frequency which appears in a FFT is $\frac{1}{2\Delta t}$, which is often called the Nyquist frequency.

Second, one must choose the frequency resolution required for a given investigation. One might imagine that the lowest frequency (besides a zero-frequency or average-value term) in a Fourier series would be that of a wave whose period was equal to the length of

the time series. Succeeding terms in the Fourier series correspond to waves which fit into the interval successively larger integral numbers of times, with periods decreasing as $1/n$ (frequency rising as n). The difference in frequency between the n^{th} wave and the $n+1^{th}$ wave (the frequency resolution) is clearly equal to the frequency of the $n=1$ wave, namely $\Delta f = \frac{1}{N\Delta t}$, where N is the number of time series points in a single transform.

The ideal situation for the application of spectral analysis would be one in which the phenomena under study had characteristic time scales much longer than $N\Delta t$, and frequency structure coarser than Δf defined above. For example, to resolve a Doppler shift from an approaching/receding wave source would require $\frac{v_R}{v_\phi} \gg \frac{\Delta f}{f}$, where v_R is the spacecraft velocity with respect to the source, and v_ϕ is the wave phase speed. Resolving a shift in plasma frequency due a density gradient ∇n, on the other hand, would require $\left(\frac{v_R}{\nabla n/n}\right) \ll N\Delta t$, so that in both cases the frequency shift occurring *during* a transform interval is negligible. Practically speaking, the user of spectral analysis is often pinched between conflicting requirements: choosing N too large means that the system is not effectively stationary during the transform interval, choosing N too small means that fine frequency structure must go unresolved.

5.5 Cross-spectral Analysis

A standard interferometry technique is employed in this thesis in order to gain information about the relative phase and degree of coherence of the waves observed near the Arecibo ISR. This technique, called cross-spectral analysis, allows coherent monochromatic waves to be detected in the presence of noise, and aids in the identification of wave modes and the measurement of wavelengths. Cross-spectral analysis begins with the computing of a

complex quantity: the normalized cross-spectrum, defined as:

$$C_{12} = \frac{< x_1^* x_2 >}{< |x_1| >< |x_2| >}.$$

The angle brackets denote an ensemble average. The transformed signals $x_1(\omega)$ and $x_2(\omega)$, whose cross-spectrum is being computed, are the Fourier transforms of two (typically real-valued) time series taken by our instruments. The ensembles over which averages are taken are simply sets of transforms of consecutive (or perhaps overlapping) chunks of our time series data.

The use of such consecutive time series chunks as a proxy for a true statistical ensemble of identical systems is quite common, though rarely made explicit. Such use depends on the time stationarity of the system under study, and is *always* a judgment call on the part of the user. The best that one can do is to remain skeptical of "phenomena" which depend strongly on particular choices of ensemble size or partitioning. In this thesis, cross-spectral analysis will be utilized near its limits of validity for the case being studied, its results will be presented because they are the best that is available, and because of the difficulty of obtaining more data with which to do a more comfortably valid analysis. The normalized cross spectra was implemented for this thesis work as an extension of the regular spectral analysis described above. First, the routine DFT.PRO was modified to include a /COMPLEX option for returning complex-valued spectra. Once an ordinary DFT of a segment of data has been made, a cross-spectrum or CFT can be computed in the manner described above.

It is worth pointing out some subtleties in the way in which these ensembles are constructed, and in how this relates to the blurring of transient events in the data. Note first

that any transient event on the time scales shorter than the interval from which the ensemble is drawn casts doubt on the validity of using cross-spectral analysis at all. With this in mind, consider the "radius of influence" of a single time series point in the final CFT. Each column of DFT contains the Fourier transform of N time series points. The transform window shifts by n_s between transforms, so a single point exerts some influence over $\frac{N}{n_s}$ transforms. In computing the CFT, one averages over n_E columns of DFT, shifting by one DFT column between consecutive ensembles, so that a single time series point exerts influence over $\frac{N}{n_s} + 2n_E$ CFT columns. If the interval between time series points is called Δt, then the CFT interval over which a single time series point can exert influence is

$$\tau_c = \Delta t(N + 2n_E n_s).$$

The time scale for changes in the system under study should be shorter than τ_c, otherwise the collections of DFT columns cannot be considered as members of a statistical ensemble.

5.6 Spacecraft Attitude Solution

Computing the attitude solution for Soliton was a difficult and time-consuming task. In the end, I met with success for only a section of the data, namely from 140 to 240 seconds after launch. During this interval, the attitude control system (ACS) was turned off, and the payload was performing torque-free motion. Before 140 seconds, the ACS was operating. At 240 seconds, there was a perturbation of the spacecraft motion: perhaps the CAV6 boom finally deployed or flopped or fell off, perhaps the ACS began leaking, perhaps the spacecraft collided with some tiny solid object. At any rate, I was unable to fit the ensuing motion to Euler's solution for a torque-free rigid body.

Why a Gyro Is Not Enough

The basic method I used involved fitting torque-free motion to the on-board magnetometer data. Since Soliton carried a gyro, one might reasonably ask why I did not use the gyro data, with its ready-made Euler angle outputs, to determine the attitude solution. This method, although appealing, proved impossible on Soliton. The source of the difficulty was not known until I had achieved an attitude solution by other means, and compared the Euler angles implied by my attitude solution to those indicated by the gyro. I found that the gyro outputs were multi-valued, or more precisely, exhibited hysteresis. In other words, as the spacecraft coned, if one plotted the gyro outputs against the Euler angles, one found not a linear relation, but a loop, so that the value of spacecraft pitch, for example, depended on whether the spacecraft yaw was increasing or decreasing with time. While this difficulty may be unique to Soliton, I would nevertheless like to share a few words of discouragement with anyone considering relying *entirely* on a gyro for attitude determination.

The determination of spacecraft attitude from a payload gyro is *not* a simple task. The widely-held myth that attitude solutions are straightforward, standard, or routinely found by NASA personnel does not, in fact, expedite their computation in the slightest. As pointed out by Goldstein [Goldstein, 1980], there are at least 24 different conventions to choose from in describing a rotation; only one of these is correct for your gyro. Deciding which convention is appropriate is made considerably more difficult by the propensity of certain NASA personnel to "relabel" the gyro axes, as though they were in fact interchangeable. Furthermore, the interpretation of the signals from the gyro as rotation angles is typically not well calibrated, and it will drift as time goes by and the gyro rotor slows down.

That being said, there are, nevertheless, certain things which can be relied upon to remain true. For example, if there are times in the flight when no attitude control system

(ACS) is being operated, then the payload motion will be well described by Euler's equations of motion for a torque-free rigid body [Goldstein, 1980] at those times, provided only that the payload is, in fact, sufficiently rigid. Furthermore, every gyro rotation convention of which I am aware has three distinct axes: one is fixed in *space* (points always at the same star), another is fixed in the payload (or *body*), while a third lies in the plane perpendicular to the space-fixed axis, *intermediate* to the other two. These angles, in whatever convention is chosen, have the following extremely helpful property: as the instantaneous angular velocity of the payload marches uniformly around the fixed total angular momentum vector, the rate of change of the intermediate angle is independent of the *value* of the space-fixed angle. The reverse is definitely not true: the time rate-of-change of the space fixed angle *does* depend on the value of the intermediate angle (unless, of course, the space-fixed gyro axis and the spacecraft's angular momentum vector happen to coincide). The space fixed angle is somewhat analogous to longitude in this sense: on a flight at uniform speed over the surface of the Earth, one's longitude changes abruptly when passing near the North or South Pole. In addition, the roll rate, or the rate of rotation around the rocket-fixed axis, can be reliably determined without knowing the gyro's calibration. This is possible because the sensor for roll rate is periodic; the rocket-fixed angle is known only modulo 2π. The rate of change of the rocket-fixed angle can be determined from the time required for the data labeled "roll" to return to the same value.

5.6.1 Obtaining Torque-free Parameters From Magnetometer Data

The torque-free motion of a nearly rigid axisymmetric payload is nearly easy to understand. The single best place to begin is with the figure in Marion's book[Marion, 1970], which tells the entire story. Most derivations of the equations of motion for this case, including

Marion's, contain the extremely misleading statement that in the rotating (spacecraft) reference frame, the angular velocity vector "precesses" around the body symmetry axis at a rate given by Ω. The misleading part is that this Ω is numerically quite close to what one identifies, for example in the magnetometer data, with the spacecraft *spin* rate. For a typical spacecraft this Ω is much faster than what we would call the precession or coning rate. On Soliton, the spin rate Ω is around 4 rad/s, while the coning rate is only 0.2 rad/s.

The first task to accomplish in determining the attitude solution is to estimate the coning rate. In Marion's notation, this is written $\dot{\phi}$. If the spacecraft in question carried a magnetometer, then this task truly is straightforward. $\dot{\phi}$ is directly proportional to the magnitude of the total angular momentum, and is therefore perhaps the most constant quantity encountered in spacecraft data analysis. $\dot{\phi}$ can be determined by looking at the "spin axis" magnetometer record; it is simply 2π divided by the time between the peaks.

The next task is to determine the "spacecraft spin rate". This is not so simple as it may at first appear. Again, if the spacecraft carried a magnetometer, one might think of applying the method of measuring the time between peaks and taking 2π times its reciprocal. In so doing one would discover a systematic variation in the spin rate, of a magnitude sufficiently large to spoil many perfectly reasonable attitude solution schemes. The reason for this is demonstrated in figure 5-8. In words, one might say that the time between identical phases of the magnetometer signal differs from the time between identical phases of the spacecraft attitude. On Soliton, this variation was approximately 15 % over the course of a coning period. Also, please note that performing a Fast-Fourier-Transform (see section 5.4) and selecting the frequency of the "spin peak" cannot yield a sufficiently accurate value for the spin rate. It is first of all unlikely to find a section of torque-free data sufficiently long to yield fine enough frequency resolution in the FFT. Then, having found such a section, the

FFT can yield only the *average, apparent* spin rate, which is correct only twice per coning period and will contaminate any transformed vector with "spin and cone noise". Finally, the FFT cannot even begin to model any slow decay in spin rate due to payload non-rigidity.

However, by using the spherical triangles of figure 5-8, one can derive much information from the systematic variations in "spin rate" seen by measuring, say, the "time between zeroes" of the magnetometer record. It is worthwhile to describe this procedure.

Figure 5-8 suggests a mathematical model for the rate of change of ψ_a, the "apparent spin rate" estimated from the magnetometer data. First of all,

$$\sin(\psi - \psi_a) = \sin\beta \frac{\sin\phi}{\sin p}$$

and

$$\cos(\psi - \psi_a) = \frac{\cos\beta - \cos\theta\cos p}{\sin\theta\sin p},$$

where, from the figure: ψ and ψ_a are the phase angles of the sensor $\hat{\mathbf{x}}$ with respect to the angular momentum vector $\vec{\mathbf{L}}$ and the Earth's magnetic field $\vec{\mathbf{B}}_0$, respectively, β is the angle between $\vec{\mathbf{B}}_0$ and $\vec{\mathbf{L}}$, and p is the angle between $\vec{\mathbf{B}}_0$ and the principal axis $\hat{\mathbf{e}}_3$. Note that $\hat{\mathbf{e}}_3$ is not aligned with the instantaneous angular velocity of the spacecraft ($\vec{\omega}$), nor is it likely to be precisely the same as the symmetry axis of the spacecraft. The important thing is that the angle θ_x between $\hat{\mathbf{e}}_3$ and $\hat{\mathbf{x}}$ is constant in time, which is true to the degree that the payload's moments of inertia are constant.

These formulas can be manipulated to give:

$$\psi - \psi_a = \arctan\left(\frac{\sin\theta\sin\beta\sin\phi}{\cos\beta - \cos\theta\cos p}\right)$$

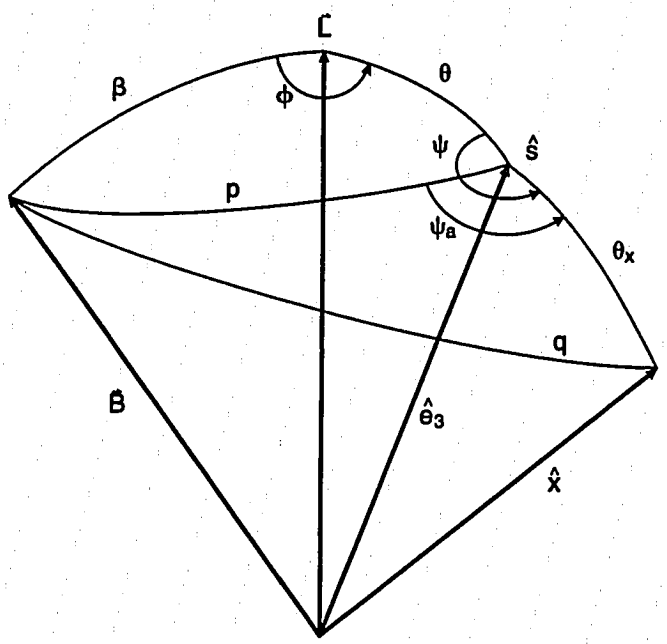

Figure 5-8: *The spherical triangles for determining spacecraft spin rate from a magnetometer record.* There are 4 vectors shown. The spin axis $\hat{\mathbf{s}}$ (also called $\vec{\mathbf{e}}_3$) cones around the total angular momentum $\vec{\mathbf{L}}$, while the sensor axis $\hat{\mathbf{x}}$ spins around $\hat{\mathbf{s}}$. The dot product of $\hat{\mathbf{x}}$ with the background magnetic field $\vec{\mathbf{B}}_0$ produces the magnetometer data.

where, again from the figure, we have $\cos p = \cos\theta\cos\beta + \sin\theta\sin\beta\cos\phi$, where θ is the $\frac{1}{2}$ angle of the spacecraft coning motion and ϕ is the coning phase.

We now write $\psi - \psi_a = (\Omega - \omega)t + \psi_0$ where ψ_0 is the value of ψ when the time t is zero, Ω is the spin rate which we are seeking, and ω is the empirically determined estimate for the rate of change of ψ_a . This allows us to obtain the formula

$$\omega = \Omega - \frac{\partial}{\partial t}\left[\arctan\left(\frac{\sin\theta\sin\beta\sin\phi}{\cos\beta - \cos\theta\cos p}\right)\right]. \tag{5.3}$$

Thus, we have a model which can be fitted to the empirically estimated spin rates ω using the free parameters $\Omega, \theta, \beta, \dot{\phi}$, ϕ_0, and ψ_0. Note that the partial time derivative in equation 5.3 could be evaluated analytically if desired. I chose not to do so, since performing the derivative numerically yielded sufficiently small uncertainties for all of the free parameters in the fitting procedure.

For a perfectly rigid body under torque-free motion, the angles θ and β are constant in time, while ψ and ϕ increase linearly with time. However, a real spacecraft nearly always has some non-rigid components, such as electric field booms. The flexing of a non-rigid part dissipates mechanical energy, and this energy may be drawn from the angular kinetic energy of the payload. Any decrease in the angular kinetic energy of the payload manifests itself as a reduced spin rate Ω, and a larger cone angle θ. In the fitting procedure outlined above, I found it best to model Ω as a constant plus a small linear decrease:

$$\Omega = c_0 + c_1 t,$$

which requires, for conservation of angular momentum,

$$\theta = \theta_0 - \frac{c_1}{c_0} \frac{t}{\tan(\theta_0)},$$

in the limit where the cumulative change in θ is small.

In summary, it is possible to nearly fully determine the torque-free motion of a spacecraft from a single magnetometer. It is necessary to have a sufficiently long section of torque-free data; a few coning periods should be adequate. A rough estimate of the coning period can be made by inspection of the data, and the apparent spin rate should be estimated approximately once per spin. Then, the model I derived above can be fitted to this apparent spin rate. In so doing, the coning rate $\dot{\phi}$, the initial coning phase ϕ_0, the initial cone angle θ_0, the angle β between the angular momentum vector $\vec{\mathbf{L}}$ and the magnetic field $\vec{\mathbf{B}}_0$, the initial spin phase ψ_0, the spin rate c_0 and any linear trend c_1 in the spin rate, can all be estimated fairly precisely. Figure 5-9 shows the results of performing this fitting procedure on the Soliton data.

The connection between a coordinate system based on $\vec{\mathbf{L}}$ and an Earth-based system can be made at this point, using a magnetic field model. A simple body-centered dipole model is probably sufficient [Fraser-Smith, 1987]. The remaining step is to determine the azimuth of $\vec{\mathbf{L}}$ with respect to $\vec{\mathbf{B}}_0$. In other words, $\vec{\mathbf{L}}$ can be rotated *around* $\vec{\mathbf{B}}_0$ without changing the magnetometer outputs, therefore this azimuth is not yet determined. However, a sufficiently long section of data can be used to restrict the range of possible values for this azimuth, since $\vec{\mathbf{B}}_0$ will not appear constant over a sufficiently large distance, and its slow shift with time can be used to determine the azimuth.

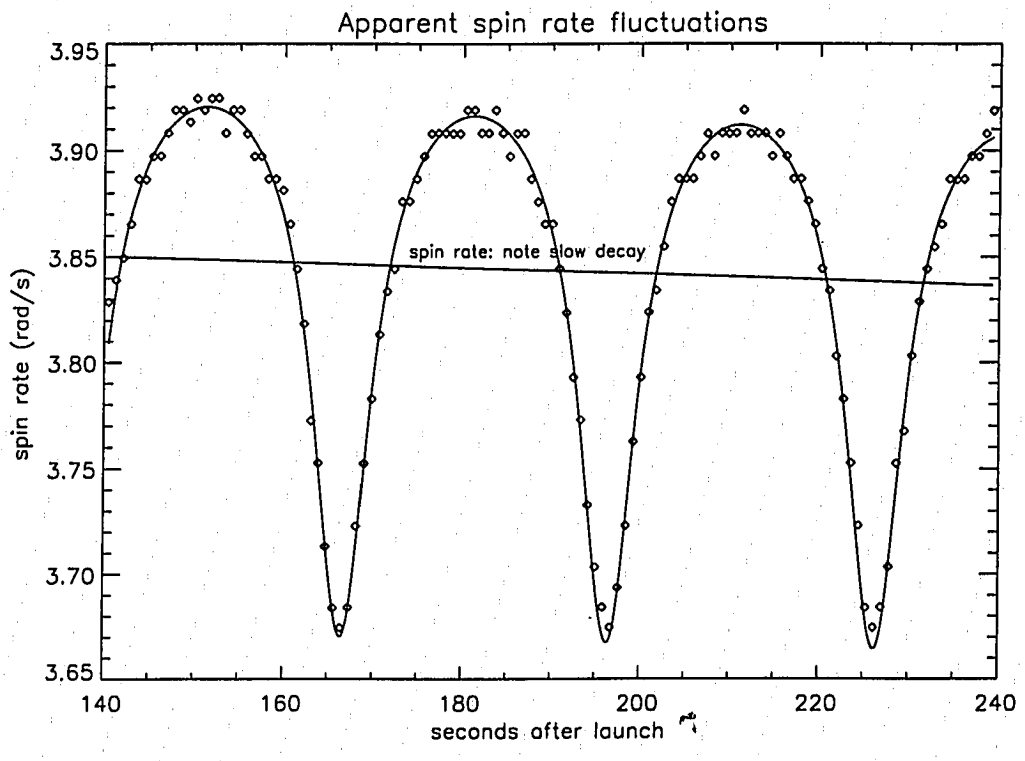

Figure 5-9: *Results of precise spin-rate determination.*The apparent spin rate, estimated from the time between zero-crossings in the x-magnetometer data, is plotted with diamonds, with a best-fit model superimposed. The spin rate Ω, extracted from the fitting parameters, is also shown.

5.7 Determination of the Convection Electric Field

The primary driving force behind our quest for a precise attitude solution for Soliton was the importance of determining the convection electric field. Such fields have not, to my knowledge, been measured *in situ* during a heating experiment. In this thesis, measurement of the convection electric field contributes to the physics of heater-driven convection, the superthermal ion plume, and the plasma drift as a fixed parameter for use in the model detector.

The signal used to determine the convection electric field is called V1-2, and it is linearly related to the difference in potential measured between the spheres marked "1" and "2" in figure 5-10. There is a subtlety here, however. The potential at each sphere is due not only to the plasma potential (as it would be in the absence of the spacecraft) but also has a contribution determined by the current collection characteristics of the sphere itself, called the sphere's "floating potential" (see section 5.3). The variability in floating potential between the spheres can be comparable to the difference in plasma potential, i.e. the difference due to convection electric field [Fahleson, 1967].

Fortunately, the variability in floating potential, which manifests itself on Soliton as a slow drift of the zero-level of the V1-2 signal, can be removed by fitting a specially modified sinusoid to the V1-2 data. In particular, I modeled the data as

$$(a_0 + a_1(t - t_i)\sin((\omega_s + a_2)t + a_3) + a_4,$$

where the various a constants are self-explanatory, t is the time and t_i is the center time of the section of data being fitted. I chose to make each section a few spins in length, and shifted t_i by a small fraction of a spin between each section. The constant a_4 shows a slow

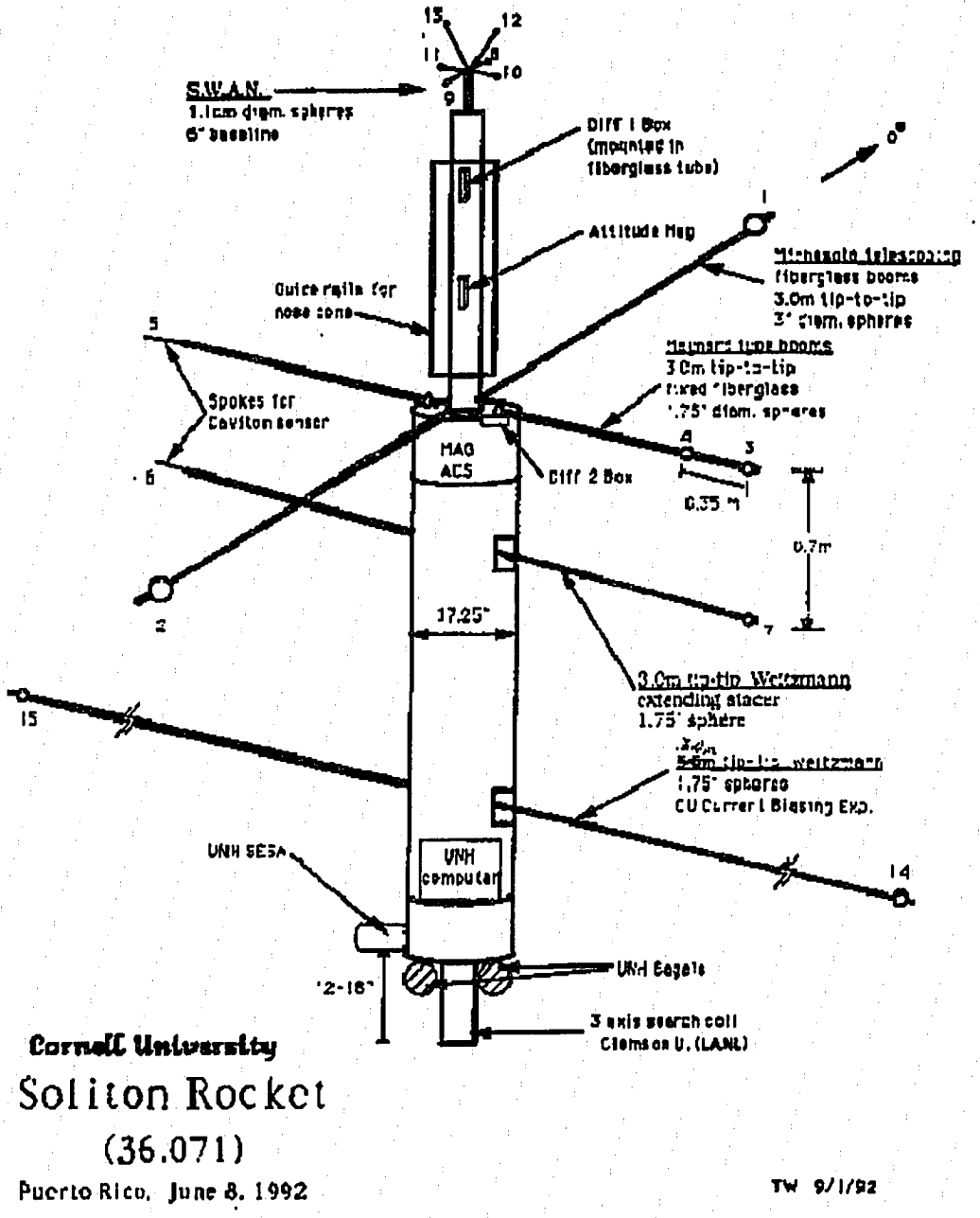

Figure 5-10: *Schematic drawing of the Soliton payload.*

drift with time, corresponding to a small, evolving asymmetry in the floating potentials of the two spheres. The constant a_2 accounts for variations in the apparent spin rate (see section 5.6), a_1 allows for small changes in amplitude within each data section, while a_0 and a_3 determine the magnitude and direction of that part of the spacecraft frame electric field which lies in the plane in which the V1-2 boom rotates. The uncertainties in these fitting parameters are quite small; most of the uncertainty in the electric field measurement comes from uncertainties in the effective "gain" of the V1-2 system, and uncertainties in the attitude solution.

The gain of the V1-2 electronics was, of course, measured in the lab prior to launch. However, when this gain is applied to the data collected between 370 and 400 seconds after launch, with the spin plane perpendicular to $\vec{\mathbf{B}}_0$, it is found that the resulting spin plane electric field is smaller than $|\vec{\mathbf{V}}_R \times \vec{\mathbf{B}}_0|$ by a constant *factor* of 0.89. Such a factor indicates either an angular alignment discrepancy of around 27 degrees (the cosine of 27 degrees is approximately 0.89), or an effective gain of 0.89. Direct inspection of the magnetometer data shows that the spacecraft spin axis was at this time well-aligned (within a few degrees) to $\vec{\mathbf{B}}_0$. Therefore, the spin plane coincided with the plane perpendicular to $\vec{\mathbf{B}}_0$, and one would expect, if anything, to see a constant *difference* between $|\vec{\mathbf{V}}_R \times \vec{\mathbf{B}}_0|$ and the envelope of V1-2. A constant difference would correspond to a small Earth-frame electric field, while a constant factor suggests a systematic instrumental error.

Because of this, I chose to increase the gain by 13 % in the interpretation of V1-2, relative to the laboratory calibration. Doing so made the V1-2 envelope coincide with $|\vec{\mathbf{V}}_R \times \vec{\mathbf{B}}_0|$ from 370-400 seconds after launch (see figure 4-5). While this choice produces a physically plausible result, it is important to be clear about how and why such "adjustments" are made. Note that the period from 370 to 400 seconds is after apogee, and is about as far as

possible from the heater, and that the gain chosen there is applied throughout the flight.

It should be noted that the attitude solution, since it was derived primarily from magnetometer data, was determined only up to a rotation around the geomagnetic field. Furthermore, it depends, for its connection to Earth-based coordinate systems, on the accuracy of the IGRF90 model for Earth's magnetic field. The choice for rotation around the geomagnetic field was made by matching the magnetic field to the IGRF model *over a sufficiently long section of the flight.* In other words, if the spacecraft moves far enough during its torque-free interval (see section 5.6) to observe a measurable change in $\vec{B}_0$, then the azimuth of the angular momentum $\vec{L}$ with respect to $\vec{B}_0$ can be determined. On Soliton, this procedure determined the azimuth of $\vec{L}$ around $\vec{B}_0$ to within 10 degrees. The precise orientation of $\vec{L}$, within that 10 degree interval, was determined by minimizing the difference between $(\vec{V}_R \times \vec{B}_0) \cdot \hat{I}$ and V1-2 for the interval 230-240 seconds. It was necessary to perform this minimization here, rather than at later times, because I was unable to find a reasonable attitude solution after 240 seconds. This choice is far more dubious than the choice of gain, since it is made much closer to the HF heater, and in fact there was no azimuth which satisfied the criterion uniformly from 230-240 seconds.

V1-2 measures the spin-plane components of the spacecraft frame electric field. It is necessary to infer the spin *axis* component by assuming that the total vector $\vec{E}$ is perpendicular to $\vec{B}_0$. This can be done by solving the equation $\vec{E} \cdot \vec{B}_0 = 0$ in the spacecraft frame, using the magnetometer signals and axes. This yields a measurement of the spacecraft frame electric field, which must be transformed to an Earth-based coordinate system. The attitude solution provides the correct rotation, while the trajectory data, together with the IGRF model for the geomagnetic field, allow one to compute $\vec{V}_R \times \vec{B}_0$, the subtraction of which yields $\vec{E}$ in an Earth-based coordinate system (the system in which $\vec{V}_R$ is measured).

5.8 Computing Miss Distances

The results of section 4.4 require the computation of the distance between points along the spacecraft trajectory and the center of the ISR beam. The spacecraft trajectory is obtained at NASA by a least-squares fit to the radar tracking data, to an accuracy of several meters [Parks, 1996]. The ISR beam location is determined from Arecibo pointing data, with arc-minute accuracy. With those two data sets in hand, a bit of vector algebra can be used to compute the desired miss distance to an accuracy on the order of 10 meters. Although the problem is quite basic, it is worth mentioning how it is solved.

Consider figure 5-11. The origin of the coordinate axes is located at the rocket launch site, and the trajectory data are expressed in this rectangular system. I chose launcher-local North, West, and Up on Soliton. The vector $\vec{s}$ describes the position of the Arecibo dish in this coordinate system, and $\hat{l}$ is a unit vector in the ISR pointing direction. Therefore, in the original coordinate system, points along the beam are given by a vector $\vec{q}$, where

$$\vec{q} = \vec{s} + t\hat{l},$$

and t gives the distance along the beam, or slant range.

If $\vec{p}$ is a point along the trajectory, we can compute the "miss vector" $\vec{d}$ by requiring $\hat{l} \cdot \vec{d} = 0$. This condition determines which point along the beam ($\vec{q}$) is closest to the rocket trajectory. We can then solve for the unknown slant range t_0, which satisfies $\hat{l} \cdot \vec{d} = 0$, obtaining $t_0 = \hat{l} \cdot (\vec{p} - \vec{s})$. So finally

$$\vec{d} = \vec{s} + t_0\hat{l} - \vec{p}.$$

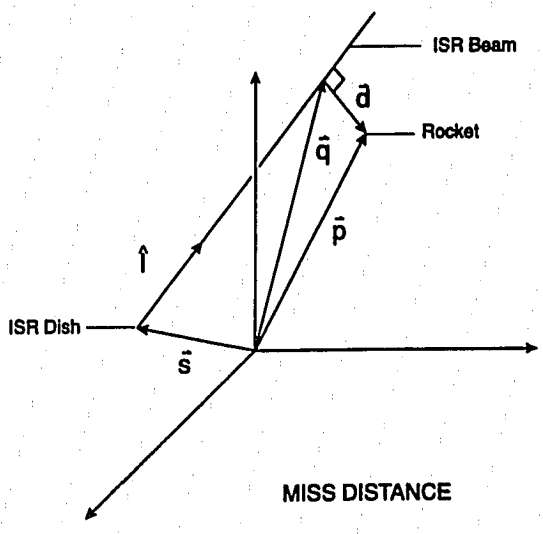

Figure 5-11: *Vectors for computing the distance between the ISR beam and the spacecraft.*

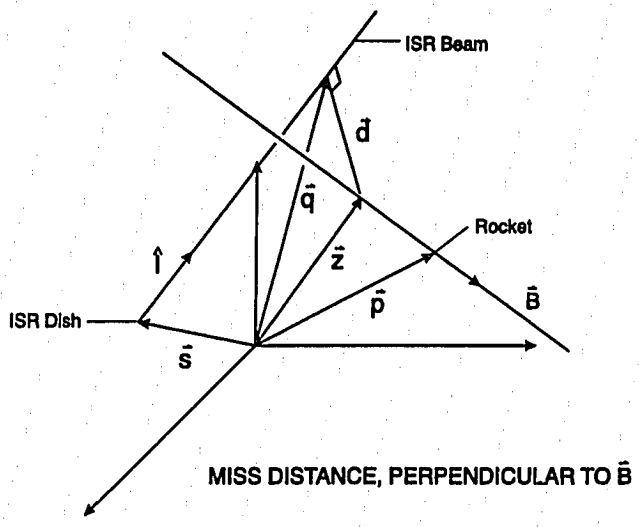

Figure 5-12: *Vectors for computing the magnetic miss distance.*

A similar calculation can be performed to determine the distance, perpendicular to $\vec{\mathbf{B}}_0$, between the payload and the ISR beam. A slight rephrasing makes the solution easy: what is the distance of closest approach between the field line threading the payload and the center of the ISR beam? Points along this field line will be called $\vec{\mathbf{z}} = \vec{\mathbf{p}} + r\hat{\mathbf{B}}$, where r parameterizes the field line, $\hat{\mathbf{B}}$ is a unit vector along the geomagnetic field, and $\vec{\mathbf{p}}$ is as before. Let r_0 be the value of r where the field line is closet to the ISR beam. Defining $l_B \equiv \hat{\mathbf{l}} \cdot \hat{\mathbf{B}}$, $p_B \equiv (\vec{\mathbf{p}} - \vec{\mathbf{s}}) \cdot \hat{\mathbf{B}}$, $p_l \equiv (\vec{\mathbf{p}} - \vec{\mathbf{s}}) \cdot \hat{\mathbf{l}}$, and $b_l^{\pm} \equiv 1 \pm l_B$. There are now two conditions on the magnetic miss vector $\vec{\mathbf{d}}_B$: $\vec{\mathbf{d}}_B \cdot \hat{\mathbf{B}} = 0$ and $\vec{\mathbf{d}}_B \cdot \hat{\mathbf{l}} = 0$. These can be solved for t_0 and r_0, yielding

$$t_0 = \frac{1}{2}\left\{\frac{p_l(b_l^+ + b_l^-) - p_B(b_l^+ - b_l^-)}{b_l^+ b_l^-}\right\}$$

$$r_0 = \frac{1}{2}\left\{\frac{p_l(b_l^+ - b_l^-) - p_B(b_l^+ + b_l^-)}{b_l^+ b_l^-}\right\}.$$

These values can then be used to compute $\vec{\mathbf{d}}_B = \vec{\mathbf{q}} - \vec{\mathbf{z}}$.

5.9 The Use of Count Rate Fluctuations

A somewhat subtle feature may be visible in the spectrogram of figure 4-1. Before 170 seconds, when the rocket is below the heater reflection altitude, measurements of the particle flux are rather noisy. After 170 seconds, when the rocket is no longer illuminated by the heater, the data appear quite regular, repeatable, and quiet. Ordinarily, it is expected that a detector of this type will see fluctuations consistent with Poisson statistics; the standard deviation in successive samples should be equal to the square root of the mean. For the ion Bagel, however, if one plots the ratio of variance to mean as a function of energy, one finds that before 170 seconds there are large fluctuations at low energies, and that there is always an energy above which the fluctuations quickly return to Poisson levels. Above the heated

region, after 170 seconds, the fluctuations are always consistent with Poisson statistics.

What is the meaning of these energy dependent fluctuations within the heater beam? It is possible that they are related to heater induced density fluctuations. To understand this , it is important to realize that a detector like the ion Bagel gathered particles from a region of finite size. The ion Bagel accepted the counts for one sample over a period of approximately 1 millisecond. During this time, the ions which will eventually enter the detector travel a distance proportional to the square root of the selected energy (their velocity). The mean time between collisions was always at least one second in this case, while the gyro frequency was approximately 35 Hz for O^+. So, large angle collisions were rare and ions typically went through 1 degree or so of gyration during a sample time. Therefore, ion trajectories can be imagined as straight lines filling a cone converging on the Bagel with a 1/2 angle of 10 degrees. For a given ion species, say O^+, the length of this cone's axis is proportional to the square root of the energy of the sampled particles. If the plasma is isotropic, at least over the sampled cone angle, the action of the Bagel can be thought of as an integration over density fluctuations up to a maximum length scale which depends on the sampled energy and the mass composition. As the energy is increased, the maximum sampled length scale increases as well. If the density fluctuations have a preferred length scale L_p , then the result of sampling over scales smaller than L_p will depend strongly on which phase of the fluctuation is sampled. On the other hand, when sampling high energy ions, at maximum length scales longer than L_p , the relative fluctuation level will decrease dramatically as many cycles of spatial density fluctuation are integrated into one count rate. More precisely, the relative fluctuation amplitude in counts for a sinusoidal density fluctuation of wave number k_0 is given by $\frac{\sin(x)}{x}$ where $x = \frac{k_0 L}{2}$ and L is the length scale being sampled. In this case L_p is about $\frac{3}{2}L_{max}$ where L_{max} is the

scale where the fluctuations are decreasing most rapidly.

Attempts to utilize these ideas on Soliton are defeated by our imperfect knowledge of the dead-time saturation of our detectors. Dead-time saturation generates an effective gain (or attenuation) of the fluctuations proportional to $\frac{\partial C_m}{\partial C_a}$. Since this factor is smallest for high (paralyzed) count rates (see figure 5-3), the fluctuation spectrum typically displays a maximum at an intermediate energy, corresponding to the descent of the event rate into the non-paralyzed regime.

Chapter 6

Detector calibration

Part of the goal of this thesis is to improve our ability to interpret data from our particle detectors. Our lab uses electrostatic analyzers (biased, shaped plates) for energy selection, and microchannel plates for particle detection. The considerations of this chapter apply to this type of detector.

It is relatively straightforward under certain conditions to relate counts recorded by a detector in space to the plasma distribution function near the spacecraft. Under these conditions, the count rate is basically proportional to the differential energy flux $E \cdot J(E, \hat{\mathbf{n}})$, where J is the number of particles of energy E which pass through a unit area in a unit time traveling in direction $\hat{\mathbf{n}}$. The main difficulty, under these favorable conditions, is to eliminate systematic errors in our knowledge of the gain of the detector, or its geometric factor. These systematic errors are primarily associated with uncertainty in the input during calibration; we don't know how many electrons are coming at the detector in the calibration tank, so we aren't certain of the detector's absolute calibration. Relative calibration, i.e. the determination of the relative sensitivity of a detector at various look angles and particle energies, is routinely obtained at the time of this writing. So, what are the favorable conditions allowing straightforward interpretation of rocket data?

6.1 The Action of a Detector

The required conditions are best illustrated by deriving a fairly precise mathematical model for the action of a detector, i.e. what a detector *does* to produce counts. To do this, we need the concepts of the plasma *distribution function*, the detector's *response function*, and the idea of integral *convolution*. The plasma distribution function $f(\vec{x}, \vec{v})$ describes how many particles one would expect to find at $\vec{x}$ having a velocity of $\vec{v}$. It can be imagined, when properly normalized, as a probability density in a six-dimensional phase space [Chen, 1984], i.e. a three-dimensional position $\vec{x}$ and a three-dimensional velocity $\vec{v}$. The detector's response function $g(E, V, \hat{n})$ describes the likelihood that a given count appearing in the data stream resulted from a particle coming from a direction $\hat{n}$, having an energy E, given that the detector's analyzer voltage was V. To produce counts, a detector basically integrates the product of these two functions over all the energies and look directions where they are both non-zero. In the calibration tank, we use a spatially broad and uniform electron beam with narrow angular and energy widths; thus the counts produced by a detector in the calibration beam are proportional to the response function at $(E, V, \hat{n})$. In this way we can sample the response function at various specific energies, look directions, and analyzer voltages[Garbe, 1990].

The conventional intuitive model for how our detectors work in space contains the idea of *combing* out the value of f in the vicinity of the detector at the energy selected by the analyzer voltage. Note that here we are operating in the opposite limit from the one found in the lab : in space, in this intuitive model, the *input* flux is assumed to be flat in energy space and isotropic compared to the narrow comb of the response function. This limit is sometimes realized in space: for example, in the aurora, the tail of the electron distribution may have an effective temperature of 1 keV at energies of several keV[Lynch, 1992] compared

to the response function width of 150 eV. Yet even in the aurora, the intuitive model fails to appreciate the fact that auroral electrons may be highly field-aligned (less than one degree); they are not isotropic over the angular width of a typical detector. Therefore, the plasma angular distribution may be combing out the detector's angular response: just the opposite of what intuition assumes.

To go beyond the intuitive model, we need to write down the convolution integral describing the action of a detector. The combing ideas described above then correspond to a situation where one or the other of the factors in the convolution can be reasonably well modeled by a delta function. Imagine a small section of the detector's response function: the analyzer has been set to V, and some particles with energy E are incident from direction $\hat{\mathbf{n}}$. The *value* of the response function g, at this point $(E, V, \hat{\mathbf{n}})$, then tells us what fraction of these particles will be recorded as counts. The integral then collects all these contributions into the output count rate.

$$\delta C = \eta \delta A \cos\theta f(\vec{\mathbf{v}})\, d^3v\, v\delta t \tag{6.1}$$

Equation 6.1 shows the contribution to the counts of the particles in the phase space volume $d^3v\ \ \delta A\ v\ \delta t$. There are $f d^3v\, \delta A v \delta t$ such particles. Each passes thru the detector aperture δA where it is detected with an efficiency of η. The factor $\cos\theta$ describes the reduction in effective aperture area for particles incident at an angle θ to the aperture normal. Note that both δC and η are dimensionless numbers, and that $\eta = \eta(E, \hat{\mathbf{n}})$ and finally that $E = \frac{1}{2}mv^2$. Equation 6.1 simply says that f is translationally invariant across δA , that it is constant in time throughout δt , and that spatial variations in f along $\vec{\mathbf{v}}$ occur on length scales longer than $v\delta t$. The following manipulations are helpful :

$$d^3v = v^2 \sin\theta d\theta d\phi$$

$$\delta C = \eta \delta A \cos\theta f v^2 dv \sin\theta d\phi v \delta t$$

$$\frac{\delta C}{\delta t} = \eta \delta A \cos\theta f \cdot (\frac{2E}{m})^{\frac{3}{2}} d((\frac{2E}{m})^{\frac{1}{2}}) d\Omega$$

Thus we obtain:

$$\frac{\delta C}{\delta t} = \frac{2}{m^2} \eta \delta A \cos\theta E f dE d\Omega.$$

Note that ϕ is an azimuthal angle, and that $d\Omega$ is the element of solid angle near the direction $\hat{\mathbf{n}}$. This is our standard model for the action of our detectors. Note especially the odd mixture of finite and infinitesimal elements. The main difficulty in interpreting particle data arises from the standard procedure of simply replacing the infinitesimals dE and $d\Omega$ with their finite cousins, and then continuing to assume that f is constant over these *finite* ranges.

6.1.1 Alternative Model for the Action of a Detector

There is another, simpler, more geometrical way of looking at the action of the detector. Instead of viewing the detector as a counter constantly responding in time to a given flux, we can imagine it as taking snapshots of a particular region of six-dimensional phase space. The response function described above determines what part of three-dimensional velocity space is sampled. How is a particular region of real space selected? Imagine that a particle has just been successfully counted. If we follow its trajectory backwards in time until the time when counting began, and do similarly with every count in a given accumulation time, we will

describe a region of real space which contains all these initial positions. If instead of tracing particles back in time, we calculate all possible successful trajectories, we can describe the boundary of this region fairly precisely. A particle contained in this region at the beginning of an accumulation will be counted during that accumulation. The only limitation to this method is that the mean time between large angle scatters must be long compared to the accumulation time. This is usually satisfied quite well; the experiment described in this thesis has an accumulation time of around 1 millisecond, while the relevant collision time is about one second. Viewing the action of a detector in this way: taking *instantaneous* snapshots of a region of phase space at the exact moment when counting begins; allows the use of statistical mechanical methods relating the fluctuations in the particle number N to the form of the two particle correlation function [Bogoliubov, 1962][Ichimaru, 1980][Pathria, 1991].

6.1.2 "Response Function" Depends on Context

The quantity $\eta(E, V, \hat{\mathbf{n}})$ is what would naturally be called the "response function" by a person doing a computer simulation of a detector. Particles would be launched with equal likelihood from various points across the aperture with various initial velocities. The trajectories of these particles are integrated through the analyzer's electric field. They will eventually either hit the analyzer and be absorbed or succeed in reaching the channel plates. The fraction of successful trajectories is then recorded; this fraction is equal to η in the limit of perfectly efficient channel plates. (Channel plate efficiency is typically $\sim 50\%$ [Kurz, 1979].)

In the calibration tank, the situation is slightly different. It is difficult to isolate particular regions of δA and shoot actual physical particles through only those regions[Kletzing, 1991]. Furthermore, the aperture reducing effect for off-axis particles, described by the factor $\cos\theta$,

cannot be unfolded from variations in other factors, in the lab. So the natural choice for for what "response function" refers to in the lab is not η but $\eta\delta A\cos\theta \equiv g(E,V,\hat{\mathbf{n}})$. So, finally:

$$\delta\dot{C} = g\frac{2E}{m^2}f dE d\Omega$$

$$\dot{C} = \frac{2}{m^2}\int g(E,V,\hat{\mathbf{n}})Ef(E,\hat{\mathbf{n}})dEd\Omega\ . \tag{6.2}$$

Equation 6.2 is the convolution integral which describes the action of our detectors in a plasma which is spatially uniform, but possibly anisotropic in velocity space. It can often be reduced to a simpler relation, but not always. As it is, it is correct provided only that the plasma is in steady-state on time scales of at least δt , and uniform on length scales of at least $v\delta t$.

6.2 Computing the Geometric Factor

For the purpose of comparing the sensitivity of various detectors, and for estimating their relative count rates in generic plasmas, a number called the geometric factor can be derived. The geometric factor can be thought of as an integral over the response function, as the effective target area of a detector, or as the response of the detector to a particular sort of plasma: one which is isotropic, and uniform in energy wherever $g(E,\hat{\mathbf{n}})$ is nonzero. With these things in mind, the geometric factor is a useful number.

It is helpful at this point to define the differential energy flux $J(E,\hat{\mathbf{n}})$. It is the number of particles with kinetic energy E, going a direction $\hat{\mathbf{n}}$, which cross a unit area normal to $\hat{\mathbf{n}}$ per unit time. The units of J are $(cm^2-ster-eV)^{-1}$. J can be found hiding in equation 6.1.

By following the manipulations after equation 6.1, we can pull out the relation:

$$J(E, \hat{\mathbf{n}}) = \frac{2E}{m^2} f,$$

so that

$$\dot{C} = \int g(E, V, \hat{\mathbf{n}}) J(E, \hat{\mathbf{n}}) dE d\Omega \,. \tag{6.3}$$

If J is indeed constant where g is nonzero, it can be factored out of the integral, leaving

$$\dot{C} = J(E_0, \hat{\mathbf{n}}_0) \cdot \int g(E, V, \hat{\mathbf{n}}) dE d\Omega \equiv J(E_0, \hat{\mathbf{n}}_0) \cdot G(V) \,.$$

Note that G still depends on V. Now we can use a convenient fact about electrostatic analyzers to remove this dependence. The energy width δE of a detector's response function is proportional to the voltage applied to the analyzer. In fact, δE contains the entire voltage dependence of G. The center energy of the response, E_0, is also proportional to the analyzer voltage. Therefore the ratio $\delta E / E_0$ is a constant, call it ϵ. Now, we can express $G(V)$ like this:

$$G(V) = \delta E \cdot \int g^*(\hat{\mathbf{n}}) d\Omega \,,$$

where g^* is the average value of the response function over the energy width. Using the definition of ϵ, we get:

$$G(V) = \epsilon E_0 \int g^* d\Omega \equiv E_0 G_0 \,.$$

Note that the V dependence of G is now hidden in E_0, and that G_0 is now a constant, characteristic of a *detector*. G_0 is often called the energy-independent geometric factor.

Note that G and G_0 are not the same: G_0 is smaller by the factor E_0 and has a different relationship to flux and counts, namely

$$\dot{C} = E_0 G_0 J(E_0, \hat{\mathbf{n}}_0) \ .$$

6.3 Absolute Calibration:Faraday Cup Measurements

It is possible to learn a great deal using a detector calibrated with the methods described thus far. However, in order to measure density, compare with previous measurements by other detectors, and insure physical validity and meaningfulness, it is necessary to do an *absolute* calibration. In practical terms, this means that it is necessary to have an independent measure of the flux of the particle beam from the electron or ion source used in the calibration. Since the energy, angular, translational dependencies of the calibration beam used in this thesis had already been carefully measured [Garbe, 1990], the task undertaken in this thesis was to measure the absolute flux near the center of the usable beam, providing a normalization factor for the entire beam.

This absolute measurement of beam flux is provided by a simple Faraday cup[Moore, 1983]. The Faraday cup is an isolated electrode of appropriate (and well known) size and shape which can catch the calibration beam and feed the collected current to an electrometer. In our lab, cup currents are in the picoampere range, and the measurement is a bit tenuous and noisy. However, our Faraday cup does provide us with a reasonable estimate of the absolute response function of our detectors where none was available before.

Figure 6-1 shows the design and dimensions of the cup. The elongated aspect was intended to trap secondary electrons since their escape would constitute an error in the collected current. The cup collection surface is heavy-duty copper foil which was rolled into

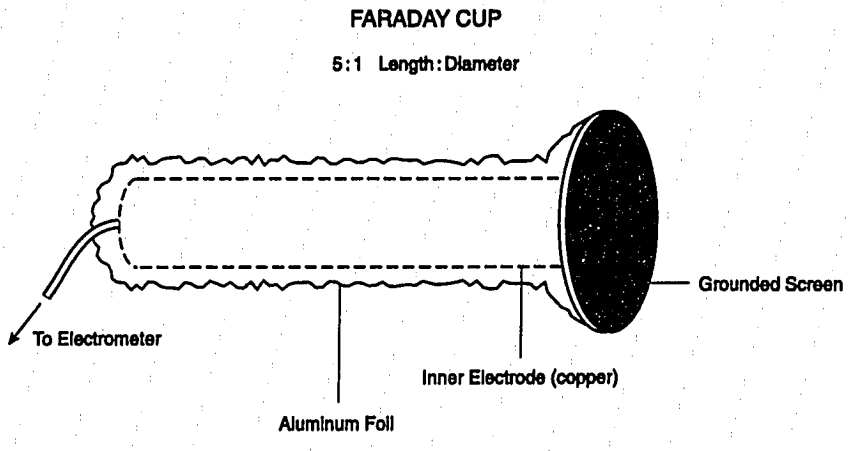

Figure 6-1: *The Faraday cup.* The right-hand end is open, while the left is closed to catch the calibration beam.

a tube. A circular piece of foil was soldered to the back end. The center conductor of a coax cable is soldered to this bottom piece. The tube has a cross-sectional area of 3.33 cm^2. The Faraday cup was tried in several different situations in order to determine its range of usefulness. First, the cup was placed in our small bell jar with the Kimball Physics electron source, where it collected currents in the nanoampere to microampere range. Here the cup made it easy to see the exponential dependence of beam current on the current fed to the source's filament, as well as a linear dependence (with eventual saturation) of beam current on accelerating voltage. Neither of these effects was new or surprising, but the Faraday cup allowed these observations to be made over a wide range of beam currents without the complication of analyzers, microchannel plates, or paralyzable dead-time saturation.

The most important measurement to make with the cup was of course the total flux of the calibration beam. In this thesis, the electron source in the Arnoldy lab was used. It produces electrons by photoionization using a diffuse ultraviolet source. I measured the beam flux as a function of the current delivered to the mercury-vapor tube of the UV lamp. The result is shown in figure 6-2. The cup current depends approximately linearly on the beam current. Since the UV flux from the lamp is dependent on the pressure in its mercury vapor tube, it is subject to slow thermal variations as the lamp current is varied. Figure 6-2 displays some of this variability. The lamp current was swept up and down over a period of several minutes. Note how the beam current values from the upward sweep are not reproduced on the downward sweep. Also, many measurements of cup current were made over a 30 minute period for a lamp current of 15 mA. These data give us some idea of the relative precision of our Faraday cup measurements.

The Faraday cup has a secondary grid which can be biased to a negative potential in order to help push any ejected secondary electrons back into the cup. It was found during

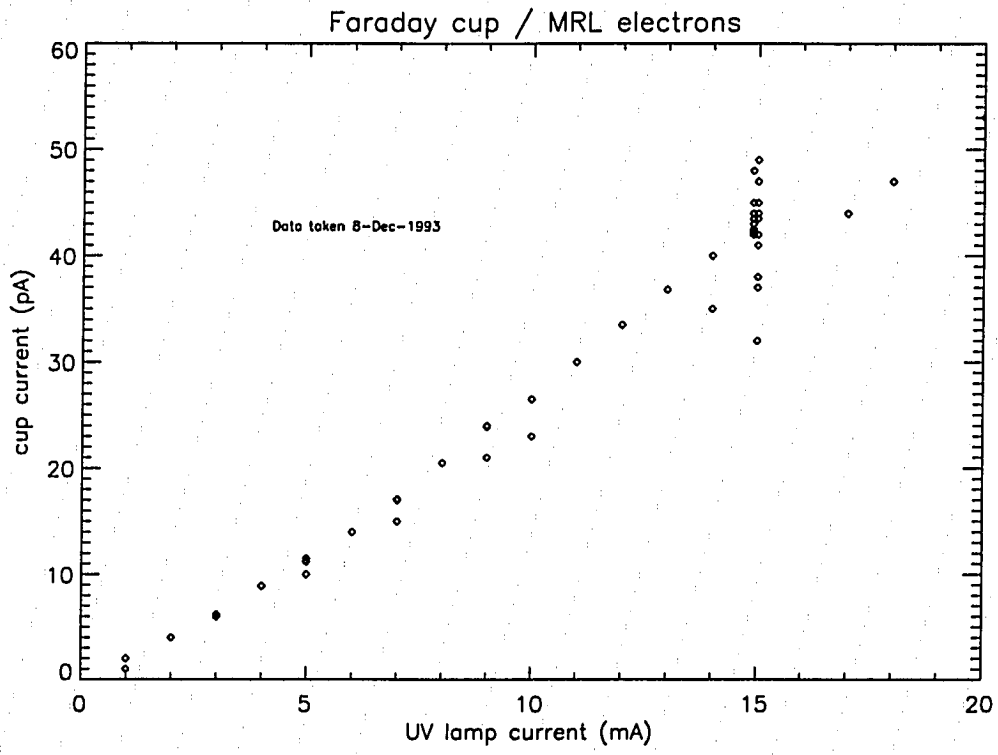

Figure 6-2: *Sample of Faraday cup data from Arnoldy calibration tank*

testing that this grid has very little effect on the measured current for the primary energies (0-4 keV) typically used in our lab. In particular, an empty coffee can was placed in the calibration beam, with suitable external insulation, with results similar to those shown in figure 6-2.

Using the Faraday cup involves placing it in the calibration beam alongside the detector being calibrated. As the detector is being stepped through its states (two angles and the analyzer voltage), one should, every few minutes, measure the current collected by the cup using the Keithley electrometer owned by the Magnetospheric Research Lab (Arnoldy). It is necessary to do this *during* the calibration of each particle detector, because of the high degree of variability exhibited by the UV lamp, both during each run, and with the passage of time.

Chapter 7

Difficulties and Recommendations for Future Work

7.1 Tales of Woe and Possible Remedies

The greatest disappointment on Soliton was the complete absence of electron data. All plans for the analysis of Soliton data revolved around searches for bursts of superthermal electrons and their correlation with the heater wave, and without these data, the project was initially considered a total loss.

Spacecraft charging is probably responsible for the lack of electron data. The cause of the anomalously high level of spacecraft charging is not completely known, but its effect is clear: the thermal electron distribution has no access to the spacecraft, and the sensitivity to superthermal particles is drastically reduced as they scatter out of the angular field-of-view of our detectors on entering the spacecraft sheath.

It is also possible that incorrect connection of the electron high voltage supplies accounts for the lack of electron data. I wrote down in my notebook that I had connected them correctly, but this does not prove anything, of course. I strongly recommend that large numbers of photographs be taken at all stages of payload final assembly, particularly of something so crucial as high voltage connections, regardless of the feelings of naïve and

arrogant graduate students that this may be unnecessary. I learned a hard lesson here. There is nothing to say the connections were made incorrectly on Soliton, other than that it would explain the lack of electron data. And there is no longer any way to know for sure.

Since spacecraft charging appears to be a fact of life for payloads passing near the HF interaction region, I would recommend the use of an active biasing system for the electron detectors, allowing them to remain near the plasma potential. Such systems have already been used [Bernhardt et al., 1995], and while their construction is not trivial, it is considerably easier than reconstructing an electron distribution function from count rates of zero.

Soliton flew far enough off its intended trajectory as to nearly fail to enter the heated region. In fact, the azimuthal error in trajectory was approximately equal to the wind-weighting; a wind-weight of zero may have put it directly on target! The use of a heater such as the HAARP facility, with rapid beam steering capability, would alleviate this problem of course, as would the use of guided sounding rockets.

The ACS was responsible for some unfortunate ambiguity on Soliton. In my opinion, the ACS should be programmed to avoid the "hard-fire" mode. It is difficult to believe that allowing at least 25% of each payload rotation to be gas-free would significantly diminish the ACS performance. Precision is not an issue in this case; the only thing "hard-fire" can do is avoid an all out tumble, which 75 % fire could probably do just as well. It would be better to have more coning and more gas-free data than to corrupt *all* the data in a given period, and then cone like crazy anyway after the programmed-off time.

7.2 New Experiments Suggested by Soliton

The data which Soliton gathered near the ISR may be hinting at important phenomena caused by the ISR. If so, it is crucial to understand these phenomena in detail, in order to continue the evolution and development of what has been, without a doubt, the single most important and reliable diagnostic tool in the equatorial ionosphere.

Since our data seem to indicate the presence of electrostatic waves in the 1-100 meter wavelength range, it would make sense to search for these waves with a second radar, with a frequency of 3-300 MHz, viewing the Arecibo beam obliquely. A possible difficulty with this idea is that the waves we observed were quite localized, existing in a cylindrical shell of less than 100 meters in thickness.

Nevertheless, given the importance of confirming the data of this thesis, and the fact that two-radar campaigns are relatively common, I feel that some time should be devoted exclusively to the search for low frequency waves launched by Arecibo.

During the Soliton flight, the Arecibo ISR was operated only in a total power mode; no attempt was made to measure other parameters, most notably the ion temperature and background drift. It is difficult to over-emphasize the importance of having "redundant" measurements of these parameters during an *in situ* heating experiment. In this thesis, such additional measurements of say, HF-driven convection, might have given the results of section 4.3.2 much more concreteness and plausibility.

The data near the HF reflection height are hopelessly ambiguous. Which phenomena are temporal? Which phenomena are spatial? With a single spacecraft, there is no way to know. A rocket with one or more separate sub-payloads would be well worth the effort in a new *in situ* heater experiment. It would be particularly interesting to see ISR passes from two different spacecraft, but this is not likely, for reasons discussed in section 4.4.

Another very interesting experiment, which could be conducted simultaneously with the multi-radar and heater campaigns, would involve the use of the Fast Auroral Snapshot (FAST) spacecraft, scheduled for launch in July, 1996. FAST has a polar orbit, and a perigee as low as 300 km, so it seems possible that its state-of-the-art instrumentation could help confirm or refute the indications of superthermal ions and electrons, HF-driven convection, and ISR effects seen by Soliton. FAST has the capability of near real-time control of its instrumentation, therefore it would be possible to "re-tune" the spacecraft between passes over Arecibo (or HAARP!), and acquire data equivalent to several rocket flights, on a single night of heater and ISR operations.

Bibliography

[Arnoldy, 1994] Arnoldy, R. (1994). Personal communication.

[Bernhardt et al., 1989] Bernhardt, P., Duncan, L., and Tepley, C. (1989). Heater-induced cavities as optical tracers of plasma drifts. *Journal of Geophysical Research*, 94(A6):7003–7010.

[Bernhardt et al., 1988] Bernhardt, P., Duncan, L., Tepley, C., Behnke, R., and Sheerin, J. (1988). Artificial airglow excited by high-power radio waves. *Science*, 242:1022–1027.

[Bernhardt et al., 1995] Bernhardt, P., Siefring, C., Rodriguez, P., Haas, D., Baumback, M., Romero, H., Solin, D., Djuth, F., Duncan, L., Hunton, D., Pollock, C., Sulzer, M., Tepley, C., Wagner, L., and Goldstein, J. (1995). The ionospheric focused heating experiment. *Journal of Geophysical Research*, 100(A9):17,331–17,345.

[Biondi et al., 1970] Biondi, A., Sipler, D., and Jr., R. H. (1970). Optical (λ 6300) detection of radio frequency heating of electrons in the F region. *Journal of Geophysical Research*, 75:6421–6424.

[Boehm et al., 1994] Boehm, M., Carlson, C., McFadden, J., Clemmons, J., Ergun, R., and Mozer, F. (1994). Wave rectification in plasma sheaths surrounding electric field antennas. *Journal of Geophysical Research*, 99(A11):21,361–21,374.

[Bogoliubov, 1962] Bogoliubov, N. (1962). *Studies in Statistical Mechanics.* North Holland Publishing Company, Amsterdam.

[Bowles, 1958] Bowles, K. (1958). Observations of vertical-incidence scatter from the ionosphere at 48 Mc/s. *Physical Review Letters*, 1:454–455.

[Carlson et al., 1972] Carlson, H., Gordon, W., and Showen, R. (1972). High frequency induced enhancements of the incoherent backscatter spectrum at arecibo. *Journal of Geophysical Research*, 77:1242–1250.

[Chen, 1984] Chen, F. (1984). *Introduction to Plasma Physics.* Plenum Press, New York, second edition.

[Cheung et al., 1989] Cheung, P., Wong, A., Tanikawa, T., Santoru, J., DuBois, D., Rose, H. A., and Russell, D. (1989). Short-time-scale evidence for strong Langmuir turbulence during H-F heating of the ionosphere. *Physical Review Letters*, 62(23):2676.

[Churchill and Brown, 1963] Churchill, R. and Brown, J. (1963). *Fourier Series and Boundary Value Problems.* McGraw-Hill Book Company, third edition.

[Coster et al., 1985] Coster, A., Djuth, F., Jost, R., and Gordon, W. (1985). The temporal evolution of 3-m striations in the modified ionosphere. *Journal of Geophysical Research*, 90(A3):2807–2818.

[Das and Fejer, 1979] Das, A. and Fejer, J. (1979). Resonance instability of small-scale field aligned irregularities. *Journal of Geophysical Research*, 84(A11):6701–6704.

[Decreau et al., 1975] Decreau, P., Prange, R., and Berthelier, J. (1975). Optimization of toroidal electrostatic analyzers for measurements of low energy particles in space. *Reviews of Scientific Instruments*, 46(8):995–1007.

[Djuth et al., 1987a] Djuth, F., Jost, R., Ierkic, H., Sulzer, M., and Noble, S. (1987a). Observations of HF-enhanced ion waves in the ionosphere. *Geophysical Research Letters*, 14:194–197.

[Djuth et al., 1987b] Djuth, F., Thidé, B., Ierkic, H., and Sulzer, M. (1987b). Large F-region electron temperature enhancements generated by high power HF radio waves. *Geophysical Research Letters*, 14(9):953–956.

[DuBois, 1991] DuBois, D. (1991). Private communication.

[Duncan, 1995] Duncan, L. (1995). Personal communication.

[Duncan et al., 1988] Duncan, L., Sheerin, J., and Behnke, R. (1988). Observations of ionospheric cavities generated by high-power radio waves. *Physical Review Letters*, 61:239–242.

[Evans, 1969] Evans, J. (1969). Theory and practice of ionosphere study by Thomson scatter radar. *Proceedings of the IEEE*, 57(4):496–530.

[Fahleson, 1967] Fahleson, U. (1967). Theory of electric field measurements conducted in the magnetosphere with electric probes. *Space Science Reviews*, 7:238–262.

[Fejer, 1979] Fejer, J. (1979). Ionospheric modification and parametric instabilities. *Reviews of Geophysics and Space Physics*, 17(1):135.

[Fraser-Smith, 1987] Fraser-Smith, A. (1987). Centered and eccentric geomagnetic dipoles and their poles, 1600-1985. *Reviews of Geophysics*, 25(1):1–16.

[Garbe, 1990] Garbe, G. (1990). *A study of ion acceleration at rocket altitudes: and development and calibration of pitch angle imaging charged particle detectors.* PhD thesis, University of New Hampshire.

[Goldman, 1984] Goldman, M. (1984). Strong turbulence of plasma waves. *Reviews of Modern Physics*, 56(4):709 – 735.

[Goldstein, 1980] Goldstein, H. (1980). *Classical Mechanics.* Addison Wesley, 2 edition.

[Gradshteyn and Rhyzhik, 1994] Gradshteyn, I. and Rhyzhik, I. (1994). *Table of Integrals, Series and Products.* Academic Press.

[Groves, 1995] Groves, K. (1995). High Power RF Ionospheric Modification Workshop. volume 2. National Science Foundation.

[Haslett and Megill, 1974] Haslett, J. and Megill, L. (1974). A model of the enhanced airglow excited by RF radiation. *Radio Science*, 9:1005–1019.

[Hutchinson, 1987] Hutchinson, I. (1987). *Principles of Plasma Diagnostics*, chapter 3. Cambridge University Press, 1 edition.

[Ichimaru, 1980] Ichimaru, S. (1980). *Basic Principles of Plasma Physics, A Statistical Approach.* Addison-Wesley Publishing Company, Reading, Massachusettes, second edition.

[Isham, 1991] Isham, B. (1991). *Chirped Incoherent Scatter Radar Observations of the HF-Modified Ionosphere.* PhD thesis, Cornell University.

[Isham et al., 1990] Isham, B., Kofman, W., Hagfors, T., Nordling, J., Thidé, B., La Hoz, C., and Stubbe, P. (1990). New phenomena observed by EISCAT during an RF ionospheric modification experiment. *Radio Science*, 25:251–262.

[Jackson, 1975] Jackson, J. (1975). *Classical Electrodynamics.* John Wiley & Sons, Inc., second edition.

[Kelley, 1990] Kelley, M. (1990). Sounding rocket proposal to study solitary structures induced by intense electromagnetic waves. Cornell University.

[Kelley et al., 1995] Kelley, M., Arce, T., Salowey, J., Sulzer, M., Armstrong, W., Carter, M., and Duncan, L. (1995). Density depletions at the 10-m scale induced by the arecibo heater. *Journal of Geophysical Research*, 100(A9):17367–17376.

[Kletzing, 1991] Kletzing, C. (1991). Personal communication.

[Knoll, 1989] Knoll, G. (1989). *Radiation Detection and Measurement.* Wiley, 2 edition.

[Kopecky, 1968] Kopecky, V. (1968). The drift cyclotron instability of plasma in an inhomogeneous high frequency field. *Plasma Physics*, 10:609–615.

[Kurz, 1979] Kurz, E. (1979). Channel electron multipliers. *American Laboratory.*

[LaBelle and Kintner, 1989] LaBelle, J. and Kintner, P. (1989). The measurement of wavelength in space plasmas. *Reviews of Geophysics*, 27(4):495.

[Leyser and B. Thidé, 1988] Leyser, T. and B. Thidé (1988). Effect of pump-induced density depletions on the spectrum of stimulated electromagnetic emissions. *Journal of Geophysical Research*, 93(A8):8681–8688.

[Lynch, 1992] Lynch, K. (1992). *Fine Structure of Auroral Particle Acceleration.* PhD thesis, University of New Hampshire.

[Lynch et al., 1994] Lynch, K., Arnoldy, R., Kintner, P., and Vago, J. (1994). Electron distribution function behavior during localized transverse ion acceleration events in the topside auroral zone. *Journal of Geophysical Research*, 99(A2):2227–2241.

[Mantas and Carlson, 1996] Mantas, G. and Carlson, H. (1996). Reinterpretation of the 6300-å airglow enhancements observed in ionosphere heating experiments based on analysis of Platteville, Colorado, data. *Journal of Geophysical Research*, 101(A1):195–209.

[Marion, 1970] Marion, J. (1970). *Classical Dynamics of Particles and Systems.* Academic Press, 2 edition.

[McFadden, 1995] McFadden, J. (1995). Personal communication.

[Minkoff, 1974] Minkoff, J. (1974). Radio frequency scattering from a heated ionospheric volume. *Radio Science*, 9:997–1004.

[Moore, 1983] Moore, J. (1983). *Building Scientific Apparatus: a Practical Guide to Construction.* Addison-Wesley.

[Newman, 1996] Newman, D. (1996). Personal communication.

[Nicholson, 1977] Nicholson, D. (1977). Magnetic field effects on electrons during ionospheric modification. *Journal of Geophysical Research*, 82(13):1839–1845.

[Nicholson, 1983] Nicholson, D. (1983). *Introduction to Plasma Theory.* John Wiley and Sons, New York, New York.

[Noble and Djuth, 1990] Noble, S. and Djuth, F. (1990). Simultaneous measurements of HF-enhanced plasma waves and artificial field-aligned irregularities at arecibo. *Journal of Geophysical Research*, 95(A9):15,195–15,207.

[Parks, 1996] Parks, D. (1996). Personal communication.

[Paschmann, 1995] Paschmann, G. (1995). Personal communication.

[Pathria, 1991] Pathria, R. (1991). *Statistical Mechanics.* Pergamon Press, Elmsford, New York.

[Payne et al., 1984] Payne, G., Nicholson, D., Downie, R., and Sheerin, J. (1984). Modulational instability and soliton formation during ionospheric heating. *Journal of Geophysical Research*, 89(A12):10921.

[Press et al., 1989] Press, W., Flannery, B., Teukolsky, S., and Vetterling, W. (1989). *Numerical Recipes.* Cambridge University Press. FORTRAN Version.

[Rose et al., 1985] Rose, G., Grandal, B., Neske, E., Ott, W., Spenner, K., Holtet, J., Maseide, K., and Troim, J. (1985). Experimental results from the HERO project: In situ measurements of ionospheric modifications using sounding rockets. *Journal of Geophysical Research*, 690(90):2851.

[Showen and Behnke, 1978] Showen, R. and Behnke, R. (1978). The effect of HF-induced plasma instabilities on ionospheric electron temperatures. *Journal of Geophysical Research*, 83:207–209.

[Stix, 1992] Stix, T. (1992). *Waves in Plasmas.* American Institute of Physics, New York.

[Sulzer, 1994a] Sulzer, M. (1994a). Personal communication.

[Sulzer, 1994b] Sulzer, M. (1994b). Radar spectral observations of HF induced ionospheric Langmuir turbulence with improved range and time resolution. *Journal of Geophysical Research*, 99:15035.

[Utlaut, 1970] Utlaut, W. (1970). An ionospheric modification experiment using very high power. *Journal of Geophysical Research*, 75:6446–6452.

[Utlaut et al., 1970] Utlaut, W., Violette, E., and Paul, A. (1970). Some ionosonde observations of ionospheric modification by very high power, high frequency ground-based transmission. *Journal of Geophysical Research*, 75:6429–6435.

[Vedenov, 1958] Vedenov (1958). *Proceedings of the 2nd International Conference on Peaceful Uses of Atomic Energy*, volume 32, Geneva. United Nations.

[Wong and Stenzel, 1975] Wong, A. and Stenzel, R. (1975). Ion acceleration in strong electromagnetic interactions with plasmas. *Physical Review Letters*, 34(12):727–730.

[Zakharov, 1972] Zakharov, V. (1972). Collapse of Langmuir waves. *Soviet Physics JETP*, 35(5):908.

[Zakharov et al., 1989] Zakharov, V., Pushkarev, A., Rubenchik, A., Sagdeev, R., and Shvets, V. (1989). Kinetics of three-dimensional Langmuir collapse. *Soviet Physics JETP*, 69(2):334–341.